Photoelectron Spectroscopy of Small Organic Anions Prepared Using a Novel Cold Ion Source Employing Entrainment of Charged Particles

by

Yu-Ju Lu

B.S., National Chiao-Tung University, 2003

M.S., National Taiwan University, 2005

A thesis submitted to the

Faculty of the Graduate School of the

University of Colorado in partial fulfillment

of the requirements for the degree of

Doctor of Philosophy

Department of Chemistry and Biochemistry

2014

This thesis entitled:

Photoelectron Spectroscopy of Small Organic Anions Prepared Using a Novel Cold Ion Source Employing Entrainment of Charged Particles

written by Yu-Ju Lu

has been approved for the Department of Chemistry and Biochemistry

_____

W. Carl Lineberger

_____

G. Barney Ellison

Date: _____

The final copy of this thesis has been examined by the signatories, and we find that both the content and the form meet acceptable presentation standards of scholarly work in the above mentioned discipline

Lu, Yu-Ju (Ph.D., Physical Chemistry)

Photoelectron Spectroscopy of Small Organic Anions Prepared Using a Novel Cold Ion Source Employing Entrainment of Charged Particles

Thesis directed by Professor W. Carl Lineberger

Negative ion photoelectron spectroscopy is utilized to investigate the methyl anions (CH_3^- and CD_3^-), the propadienylidene anion (H_2CCC^-), and the propargylene anion ($HCCCH^-$) prepared using recently developed variations to the entrainment anion sources. Combining experiment and theory allows for further insight into the electronic and vibrational structures of these molecules.

To enhance the anion-synthesis capability, multiple, pulsed entrainment valves are used for stepwise chemistry. In addition to operation of multiple valves, pulsed plasma-entrainment anion source is developed. The major feature of this anion source is the additional pulsed valve for perpendicular entrainment of plasma, which is made in an electrical discharge. This anion source provides the capability to make substantial clusters of entrained anions, e.g., $OH^-(Ar_{n=0-32})$, as well as to stabilize products of exothermic reactions in the primary expansion, e.g., $HOCO^-$ and H_3COO^-. We expect that more pulsed valves could be used for additional complex syntheses if necessary.

The methyl anion CH_3^- is formed using the pulsed plasma-entrainment source. Upon photodetachment, the out-of-plane bending angle from the pyramidal CH_3^- anion to the planar CH_3 radical changes significantly, leading to an extended Franck-Condon progression in the umbrella mode. The observation of the well-studied ν_2 bands of CH_3 and CD_3, coupled with the dramatically

improved electron energy resolution, enables us to directly measure the inversion splitting between the 0^+ and 0^- energy levels in both CH_3^- and CD_3^-. The EAs of CH_3 and CD_3 are measured precisely; using a thermochemical cycle, the methane gas-phase acidity is refined.

The photoelectron spectra of H_2CCC^- and $HCCCH^-$ are used to characterize the electronic and vibrational structures of the corresponding neutral molecules. The reaction of O^- with allene ($H_2C=C=CH_2$) produces nearly pure H_2CCC^-, which exhibits resolved vibrational progressions. In contrast, the O^- + propyne reaction produces both H_2CCC^- and $HCCCH^-$ products. Comparison of the $HCCCH^-$ and H_2CCC^- photoelectron spectra provides information about the electronic states of HCCCH. With the aid of calculations and simulations, we can assign and characterize the electronic states of H_2CCC and HCCCH.

Dedication

To my parents.

Acknowledgements

First, I would like to thank my advisor, Carl Lineberger, for the opportunity to work in the photoelectron imaging laboratory and for his support and guidance over the past five years. Thank you for giving me the freedom to carry out my own ideas. Additionally, I have been fortunate to work with many excellent people in the group. I want to thank Elisa Miller for teaching me about imaging experiment. I had a great time working with you. I also thank Amanda Case for providing helps when needed. Your leadership and scientific knowledge impressed me. Thanks to Allan Maple de Oliveira for your friendship and help in both research and life. I wish you the best of luck with the future projects. Many wonderful group members have helped and listened to me, including Wilson Gichuhi, Julia Lehman, Daniel Nelson, Joshua Martin, Quanli Gu, Scott Wren, Kristen Lemke, and Adam Merchant. You are always my friends.

I would like to thank Barney Ellison, Mathias Weber, Robert Parson, and Heather Lewandowski for being my committee and giving comments about my thesis. Additionally, questions and discussions from the people in the Ion Super Group (Carl Lineberger, Barney Ellison, Veronica Bierbaum, and Mathias Weber groups) are also appreciated. I also thank JILA visiting fellows and many collaborators, including Anne McCoy, John Stanton, Mark Johnson, David Osborn, Robert McMahon, John Maier, Lai-Sheng Wang, and John Yukich, for a lot of suggestions and discussions about my research. This provides me many opportunities to network and meet these great professors and scientists. If I pursued my Ph.D degree in Taiwan, I would not have chances to interact with them.

I am grateful to have supports from JILA staff. Krista Beck has filled out a lot of paperwork for me; hence, I could focus on my research. Todd Asnicar and Hans Green of the machine shop

have offered good ideas to efficiently solve instrumental problems. James Fung-A-Fat in the electronics shop has provided his professional skills and experiences of circuit troubleshooting in our lab. Without these technical supports, many works would not be done as fast as they were. Thanks to the staff at JILA for all offered services.

Finally, I want to thank my family and Boulder friends. These friends have helped me get used to American life, which was challenging to me when I moved to Boulder in my first graduate year. My mother and siblings have given their full love and support to me for pursuing my Ph.D degree in America. To my wife, Pao-Hsing Hsu, thank you for your understanding and support throughout this process. I love you!

Contents

Tables

Figures

Chapter 1
Introduction

1.1 Negative Ion Photoelectron Spectroscopy

Photoelectron spectroscopy involves the measurement of the kinetic energy of electrons ejected from atoms or molecules following photoabsorption, analogous to the century-old photoelectric effect. Photoelectron spectroscopy is used to determine the binding energies of electrons in a neutral molecule, yielding information of the cationic states. Likewise, photoelectron spectroscopy of a negative ion yields the electron affinity and other information of the corresponding neutral molecule. Negative ion photoelectron spectroscopy was first implemented in JILA at the University of Colorado,[1] and has been widely applied to investigate fundamental problems in spectroscopy[2-4] and chemical dynamics.[5-12] The great advantage of negative ion photoelectron spectroscopy is that the anion precursors can be separated, manipulated, and mass-analyzed through time-of-flight mass spectrometry and other ion-based experimental techniques, resulting in unambiguous selection of the anion. Upon photodetachment, the negative ion photoelectron spectroscopy technique directly measures the electron affinity (EA) of the neutral species (see Section 1.1.1). The adiabatic EA is defined as the energy difference between the neutral molecule and the corresponding anion, both in their ground states. Useful thermochemical and spectroscopic properties of the neutral molecule can be further derived from negative ion photoelectron spectroscopy. Employing a thermochemical cycle, the measured EA, together with the ionization energy of the hydrogen atom, determines either the deprotonation enthalpy, $\Delta_{acid}H$(RH), or the bond dissociation energy, D(RH), if the other is already known.[13] Negative ion photoelectron spectroscopy is also able to measure transitions between neutral electronic states of different spin multiplicity, which is spin-forbidden (optically dark) from neutral molecules in

optical spectroscopy.[14] For example, from electron detachment from a doublet anion, the term-energy difference between the singlet and triplet states of the neutral molecule, or singlet–triplet splitting, can be determined directly (see Section 1.1.3).

In conventional negative ion photoelectron spectroscopy, an anion beam is intersected with a fixed frequency laser beam, leading to an electron ejection from an anion.[15] To obtain the photoelectron spectrum, the kinetic energy of photodetached electrons is measured with a hemispherical analyzer. The energy resolution of the conventional spectrometer is about 4 meV under optimal conditions (typically about 10 meV) and is constant over a 2.5-eV energy range. Recently, photoelectron velocity-map imaging (VMI) detectors have been used to obtain the photoelectron spectrum, where the velocity and angular distribution of the photodetached electrons can be simultaneously acquired.[16] The typical spectral resolution is approximately 6 meV for an electron kinetic energy of 0.3 eV. If, instead, slow electrons are selectively detected, high energy resolution of a few wavenumbers can be achieved; this is called SEVI (slow electron velocity-map imaging).[3] However, since electrons are detached very close to threshold, SEVI spectra are limited by the threshold effect (see Section 1.1.4), which influences the intensity of the observed signals.

1.1.1 Principle

Upon photodetachment from anions, we obtain the electron kinetic energy (eKE) distribution of the photodetached electrons, represented in Fig. 1.1. Since the electron is at least 1800 times lighter than the neutral species, nearly all of the kinetic energy is given to the electron. As a result, according to energy conservation, the electron binding energy (eBE) is calculated by subtracting the eKE from the photon energy:

$$eBE = \hbar\omega - eKE \quad (1.1)$$

where $\hbar\omega$ (blue arrow) is the photon energy of the laser. If an anion has significant Franck-Condon overlap with the ground state of the neutral molecule, its photoelectron spectrum shows the adiabatic EA and vertical detachment energy, VDE (maximum intensity of the vibrational progression). Measurement of the eKE distribution also gives information about the internal energy of the neutral molecule. From the spectrum we determine additional spectroscopic properties, such as vibrational frequencies and anharmonicities. Using higher photon energy, electronic term energies can be measured. Negative ion photoelectron spectroscopy can access neutral electronic excited states that would otherwise involve forbidden transitions from the neutral ground state, enabling characterization of excited states that are inaccessible using other spectroscopic techniques. Geometry information can be obtained from the vibrational progression in the photoelectron spectrum following the Franck-Condon principle (see Section 1.1.2). The principle states that the nuclear configuration of the molecule has no significant change during the photodetachment process since the electron moves much faster than any nuclear motion. Thus, in this important approximation, immediately following photodetachment, the anion and neutral geometries are identical. As such, a long vibrational progression is indicative of a large equilibrium geometry difference between anion and neutral species, while insignificant geometry difference between the species results in a single peak in the photoelectron spectrum at the adiabatic EA.

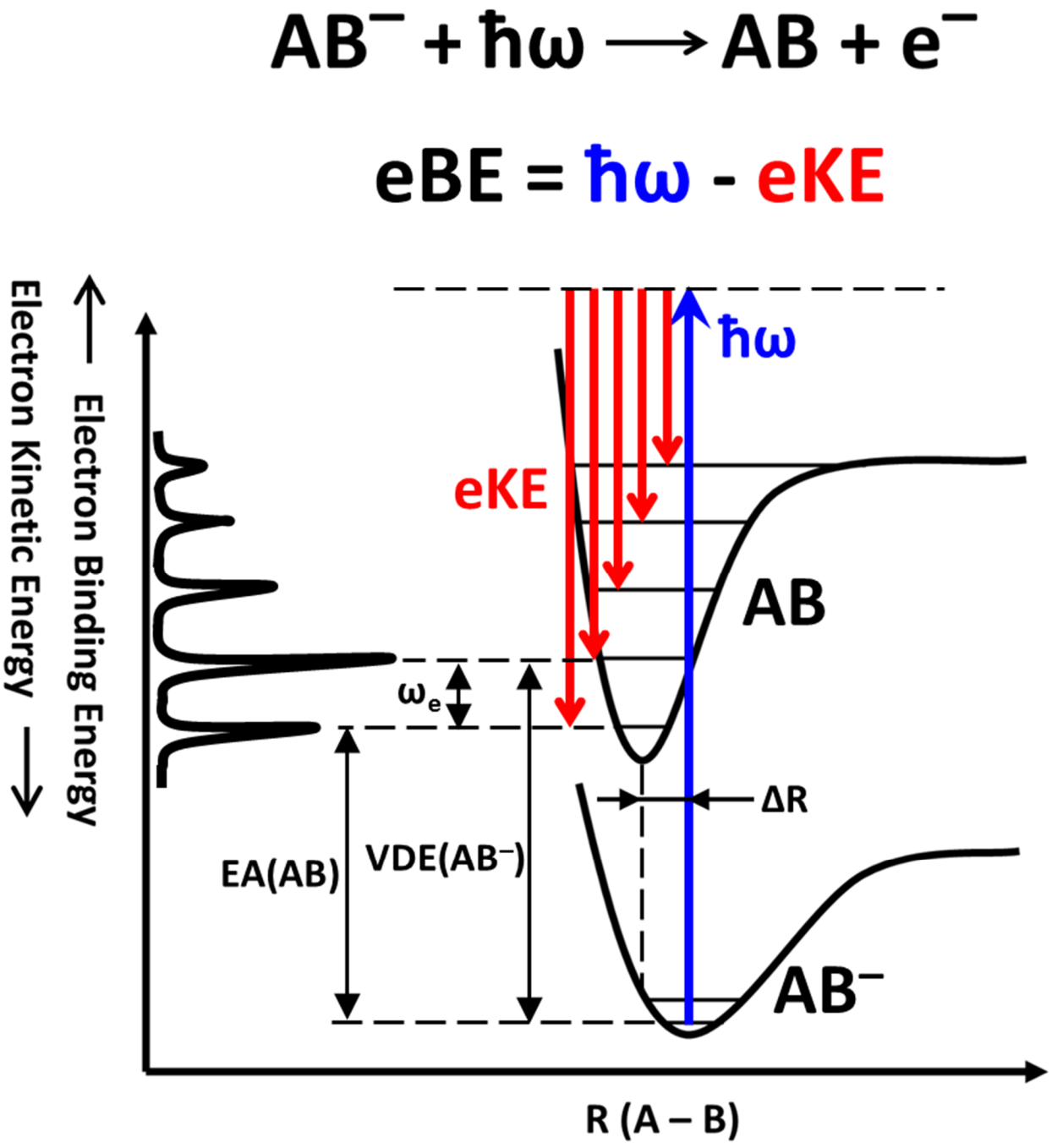

Figure 1.1 A schematic representation of the photodetachment process of anion, AB^-, along the reaction coordinate of the internuclear distance between A and B. The corresponding spectrum of the eBE and eKE distribution is shown on the left. EA is the electron affinity, VDE means vertical detachment energy, ω_e presents vibrational frequency, ΔR indicates geometry change or displacement, and $\hbar\omega$ is the photon energy.

1.1.2 Franck-Condon Factor

The photodetachment intensities of various transitions are quantitatively described by the Franck-Condon factor. In the Born-Oppenheimer approximation, the nuclei do not move when the electron is photodetached. Thus, the total wavefunction can be written as: $\Psi = \psi_e\psi_v\psi_r$, where ψ_e, ψ_v, and ψ_r represent the electronic, vibrational, and rotational wavefunctions, respectively. The ψ_e and ψ_r depend on nuclear and electron coordinates, but the ψ_v only depends on the nuclear coordinate.

The transition probability that a molecule absorbs a photon depends on the transition moment of the molecule. The transition dipole moment, $\boldsymbol{\mu}$, is defined as:

$$\boldsymbol{\mu} = \langle \Psi'' | \hat{\mu} | \Psi' \rangle,\ \Psi = \psi_e\psi_v\psi_r\ \ and\ \hat{\mu} = \hat{\mu}_{ele} + \hat{\mu}_{nuc} \tag{1.2}$$

where $\hat{\mu}$ is the operator; $\hat{\mu}_{ele}$ and $\hat{\mu}_{nuc}$ are the electronic and nuclei dipole operators, respectively. The transition moment becomes:

$$\boldsymbol{\mu} = \langle \psi"_e\psi"_v\psi"_r | (\hat{\mu}_{ele} + \hat{\mu}_{nuc}) | \psi'_e\psi'_v\psi'_r \rangle \tag{1.3}$$

$$= \langle \psi"_e\psi"_v\psi"_r | \hat{\mu}_{ele} | \psi'_e\psi'_v\psi'_r \rangle + \langle \psi"_e\psi"_v\psi"_r | \hat{\mu}_{nuc} | \psi'_e\psi'_v\psi'_r \rangle \tag{1.4}$$

$$= \langle \psi"_v | \psi'_v \rangle \langle \psi"_e\psi"_r | \hat{\mu}_{ele} | \psi'_e\psi'_r \rangle + \langle \psi"_v | \hat{\mu}_{nuc} | \psi'_v \rangle \langle \psi"_e\psi"_r | \psi'_e\psi'_r \rangle \tag{1.5}$$

The last term in Eq. 1.5 is zero due to orthogonality of the two electronic wavefunctions. In the Condon approximation, the electronic transition moment is independent of the nuclear coordinate. Thus,

$$\boldsymbol{\mu} = \langle \psi"_v | \psi'_v \rangle \langle \psi"_e\psi"_r | \hat{\mu}_{ele} | \psi'_e\psi'_r \rangle \tag{1.6}$$

Further, the transition probability can be written as:

$$\boldsymbol{\mu^2} = \left|\langle \psi''_v | \psi'_v \rangle\right|^2 \left|\langle \psi''_e \psi''_r | \hat{\mu}_{ele} | \psi'_e \psi'_r \rangle\right|^2 \quad (1.7)$$

The first term in the Eq. 1.7 is so called Franck-Condon factor (FCF), which is the square of the overlap of the initial and final vibrational states: FCF= $\left|\langle \psi''_v | \psi'_v \rangle\right|^2$.

In the case of polyatomic molecules, using anharmonic oscillator and symmetry arguments, $\Delta v = 0, \pm 1, \pm 2\ldots$ yields a non-zero Franck-Condon factor in totally symmetric vibrational modes. In contrast, for non-totally symmetric modes, only $\Delta v = 0, \pm 2, \pm 4\ldots$ have significant Franck-Condon factors.

1.1.3 Selection Rules

The selection rules for photodetachment are different from those in optical electronic spectroscopy. In addition to the Franck-Condon factors considered in Section 1.1.2, the spin angular momentum needs to be conserved. Since an electron is removed in the photodetachment process, the selection rule for electron spin is $\Delta S = \pm ½$, which is significantly different from traditional electronic spectroscopy. For example, removing an electron from a doublet anion can possibly yield either a singlet or a triplet neutral molecule, allowing for determination of the singlet–triplet splitting. Of course, in addition to the spin angular momentum, the angular momentum of the system also needs to be conserved. Since the incident photon has an angular momentum of 1ħ, photodetachment leads to a change of one unit of angular momentum, $\Delta l = \pm 1$. If an electron is detached from an s orbital ($l = 0$), the photoelectron leaves as p-type outgoing wave ($l = 1$). In terms of the electronic selection rule, single-photon detachment allows the transitions involving the removal of a single electron from an orbital, without changing other electrons.

1.1.4 Wigner Threshold Law

Another factor influencing the photodetachment intensity arises from the strong energy dependence of the near-threshold anion photodetachment cross section. While threshold photoionization of a neutral molecule is dominated by the long-range coulomb interaction between the ejected electron and the cation core, the longest range interaction in negative ion photodetachment arises from the centrifugal potential $\left(\propto \frac{\ell(\ell+1)}{r^2}\right)$ associated with the angular momentum of the outgoing electron. The energy dependence of threshold processes in which a pair of final state particles is produced the dominant long range interaction being via the centrifugal potential was derived in a classic paper by Wigner, and is now known as the Wigner Threshold Law. This effect is extremely important for photodetached electrons with low kinetic energy, which greatly affects the intensity in a SEVI spectrum. The photodetachment cross section near threshold is given by[17,18]

$$\sigma_{eKE} \propto (eKE)^{l+1/2} \tag{1.8}$$

where *eKE* and *l* are the kinetic energy and the angular momentum of the ejected photoelectron, respectively. The values of the angular momentum, *l*, are 0 (s-wave), 1 (p-wave), and 2 (d-wave). The higher the angular momentum is for the departing electron, then the stronger the long-range interaction (or higher centrifugal barrier). At a photon energy very close to the threshold, only transitions leading to the ejection of s-wave photoelectrons from a p-type orbital have significant intensities, where the cross section scales as $eKE^{1/2}$.

1.1.5 Photoelectron Angular Distributions

In addition to the electron velocity distribution, the reconstructed images show the differential cross section, which provides the photoelectron angular distribution with respect to the cylindrical symmetry axis, defined by the laser polarization direction. For linearly polarized light and single-photon detachment, the photoelectron angular distribution is described by the relationship[19]

$$I(\theta) = \frac{d\sigma}{d\Omega} = \frac{\sigma}{4\pi}\left[1 + \beta P_2(\cos\theta)\right] \qquad (1.9)$$

where θ is the angle between the velocity vector of the ejected electron and the laser polarization vector, $P_2(\cos\theta)$ is the second-order Legendre polynomial, and σ is the total cross section, and Ω is the solid angle. The anisotropy parameter, β, is determined by fitting the photoelectron angular distribution with Eq. 1.9. The β value varies from $\beta = -1$ ($d\sigma/d\Omega \sim \sin^2\theta$, a perpendicular transition) to $\beta = 2$ ($d\sigma/d\Omega \sim \cos^2\theta$, a parallel transition) and depends on the orbital angular momentum, l, of the ejected electron. For atoms, $\beta = 2$ corresponds to an outgoing p-wave electron, arising from electron detachment from an atomic s-orbital at any energy; $\beta = 0$ corresponds to threshold detachment from a p orbital, and $\beta = -1$ can stem from a linear combination of s and d waves that comes from above threshold photodetachment of a bound p-electron. For molecules, β can provide information to distinguish between transitions to different electronic states.[20]

1.2 Thesis Overview

This thesis discusses development and application of novel pulsed anion sources to obtain the photoelectron spectra of alkyl and radical anions taken with different photon energies to

improve the spectral resolution. In Chapter 2, the experimental apparatus, described in more detail, consists of the pulsed anion sources, the Wiley-McLaren time-of-flight mass spectrometer, the VMI detector, and the laser system. Various pulsed anion sources used in this thesis are presented. The laser systems employed here are described along with descriptions of data analysis. Chapter 3 details the design and characterization of a novel, cold anion source. Applications of this anion source are also demonstrated. In Chapter 4, photoelectron spectroscopy of methyl anion is discussed. The EAs of CH_3 and CD_3 are measured accurately; using a thermochemical cycle, the methane gas-phase acidity is refined. The observation of the well-studied v_2 (umbrella) bands of CH_3 and CD_3, coupled with the dramatically improved electron energy resolution, enables the direct measurement of the inversion splitting between the 0^+ and 0^- energy levels in both CH_3^- and CD_3^-. Chapters 5 and 6 focus on the photoelectron spectra of H_2CCC and HCCCH anions, respectively, to obtain information about the high-lying electronic excited states of the corresponding neutral molecules.

Chapter 2
Experimental Apparatus

2.1 Overview

An overview of the experimental apparatus is illustrated in Fig. 2.1. The detailed description of the apparatus is available in previous publications.[21-23] The apparatus consists of four main sections: an anion source, a linear time-of-flight mass spectrometer (TOF MS),[24] a velocity-map imaging (VMI) photoelectron spectrometer,[25,26] and a tunable laser system. In this thesis, two types of pulsed anion sources are developed and employed for anion formation, both of which offer significant improvements over the original anion source.[27] Specifically, the anions formed in Chapters 3 and 4 are generated using a pulsed, perpendicular, plasma-entrainment anion source. In Chapters 5 and 6, the anion syntheses occur *via* an ion-molecule reaction using a pulsed, coaxial, supersonic neutral-entrainment reactor. Following anion formation, anions are accelerated to ~3 keV, and mass-separated using a Wiley-McLaren time-of-flight mass spectrometer before entering the laser-ion interaction region. Electrons are then photodetached from the anions with radiation from a tunable laser system, allowing broad control of the kinetic energies of the detached electrons. Subsequently, a velocity-map imaging detector is utilized to obtain photoelectron velocity and angular images. The photoelectron images are reconstructed and analyzed to convert into photoelectron energy spectra. The experimental apparatus and data analysis will be further described in the following sections.

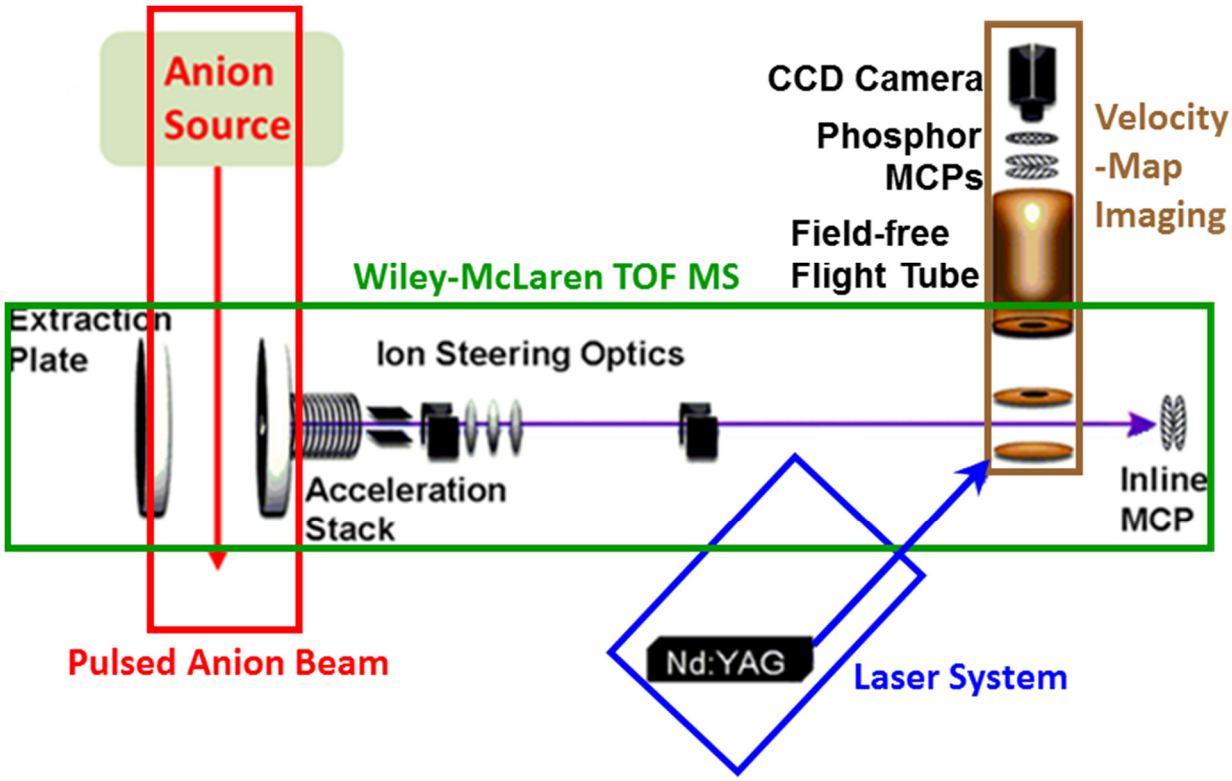

Figure 2.1 Overview of the experimental apparatus. Red represents the ion source, green represents the TOF MS region, brown represents the VMI, and blue represents the laser system.

2.2 Pulsed Anion Source

Two recently developed variations to the entrainment anion sources are employed throughout this thesis. Typically, this laboratory has generated a pulsed, anion beam by having a gas (or gas mixture) expand through a single, pulsed valve. The expanding gas undergoes interactions with a beam of electrons and produces slow, secondary electrons that attach to the molecules, forming anions.[27] Other common methods to produce anions include an electrical discharge source or sputtering,[28-31] laser vaporization,[32-35] and electrospray ionization (ESI).[36-39] However, these methods tend to be more "black magic", which makes it problematic to carry out complex syntheses of vibrationally cold anionic species. In order to enhance the anion-synthesis capability, we have employed multiple, pulsed entrainment valves to enable stepwise chemical anion synthesis that has proven exceptionally effective in continuous flowing afterglow experiments.[40-43] In addition to operation of multiple valves, different entrainments schemes are employed to incorporate plasma containing anions and/or electrons into the primary expansion. Currently, our realization of both arrangements (schematically shown in Fig. 2.2) utilize two pulsed valves with separate timings and pulse widths that are controlled by commercial (General Valve) Iota-1 valve drivers and a digital delay generator. When operating the two pulsed valves at a repetition rate of 80 Hz, the pressure within the source chamber increases to ~5×10^{-5} Torr from 1×10^{-7} Torr without a gas load when being pumped by a 10" diffusion pump. Additional pulsed valves could be employed for multistep syntheses if necessary.

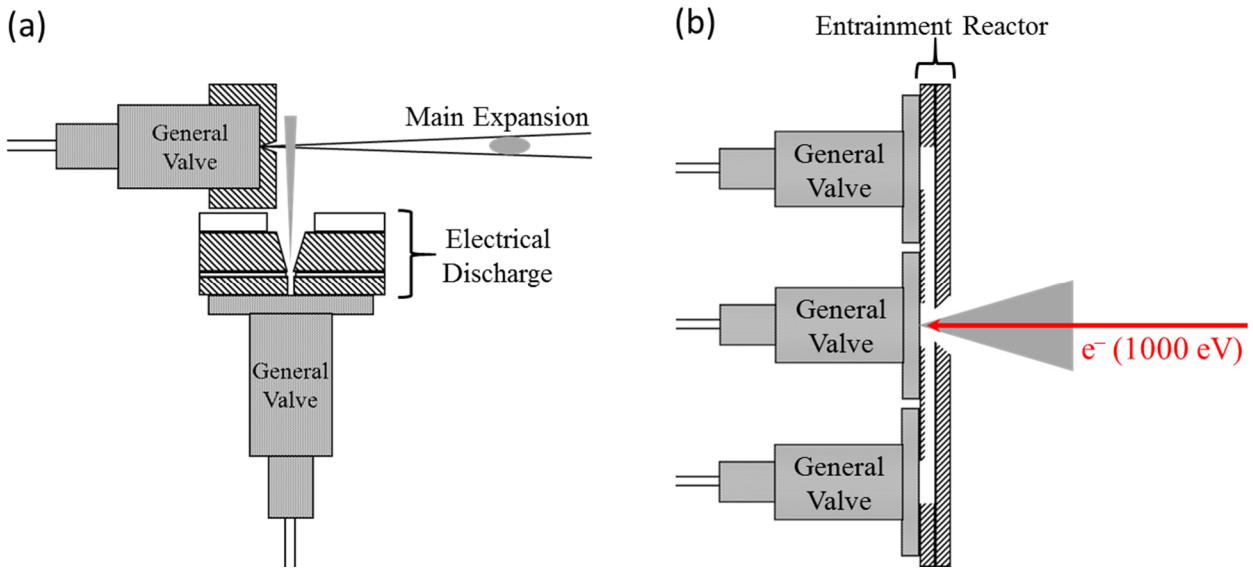

Figure 2.2 Schematic drawing of (a) the pulsed plasma-entrainment ion source and (b) the neutral-entrainment ion source. In this thesis, both designs use two pulsed valves but have the capability to entrain additional gases using additional pulsed valves.

Figure 2.2(a) displays schematically the arrangement of the pulsed, plasma-entrainment anion source. The design, construction, and performance of the pulsed, plasma-entrainment anion source are more fully described in Chapter 3. The major feature of this source is the additional pulsed valves for perpendicular entrainment of plasmas. The plasma is created by choked-flow expansion of an appropriate gas through an electrical discharge. The discharge electrodes are mounted onto the faceplate of the side pulsed valve that is oriented perpendicular to the main valve. The plasma from the side discharge valve, which operates under choked-flow conditions, interacts with the main supersonic expansion of Ar (backing pressure of 3.7 atm). The Ar acts as a carrier gas and provides additional collisional cooling. The principle of the supersonic entrainment technique was characterized and extensively studied by Campargue, in which a background gas outside of the shock-wave structure of the jet will be drawn into the free-jet zone of silence far from the orifice.[44,45] These complexities arises from the background gas colliding with the dense expansion, producing shock fronts and regions inaccessible for background gas entrainment. However, employing short, pulsed gas expansions into high vacuum essentially eliminates these shock effects, and the Campargue analysis does not apply. Specifically, there is no impediment to introducing a low-density gas (or plasma) into the barrel of the main, dense, cold expansion. It is also possible to entrain other plasmas, electrons, radicals and/or solvents at various points further downstream from the main Ar expansion. Therefore, this technique provides the capability to make substantial clusters of entrained anions, e.g., $OH^-(Ar_{n=0-32})$, as well as to stabilize products of exothermic reactions in the primary expansion, e.g., $HOCO^-$ and H_3COO^-. Since many anions formed in this anion source are demonstrated throughout this thesis, the experimental conditions will be described in each respective chapter.

Figure 2.2(b) presents a schematic drawing of one realization of the neutral-entrainment anion source also used in this thesis work. The anion source is an entrainment reactor, consisting of a central and two side pulsed General Valves with separate timings and pulse widths. Robertson *et al.* first developed and built a pulsed supersonic-entrainment reactor using the supersonic-entrainment principle, originally by Campargue,[44,45] to make cold anionic clusters.[46] Weber then combined the supersonic entrainment technique with laser vaporization to prepare metal containing cluster anions.[47] Following their design of the entrainment reactor, we synthesize the anion of interest by entraining N_2O to produce O^- with aid of an electron beam. For example, O^- reacts with allene and propyne to yield H_2CCC^- and mixtures of H_2CCC^- and $HCCCH^-$, respectively, *via* a H_2^+ abstraction reaction; this is similar to the flowing afterglow ion source, which has great control over rational anion syntheses. In order to produce the O^- reactant, one of the side valves entrains neat N_2O gas into the main expansion, which contains the other reactant embedded in Ar. This entrained, main expansion interacts with a continuous beam of 1 keV electrons, which are emitted from a thoriated tungsten filament in a homebuilt electron gun. Collisions between the gas expansion and the electron beam yield slow secondary electrons that form the O^- reactant through dissociative electron attachment of N_2O. To increase the number of anions generated, the electron beam is collimated towards the main valve with a ring magnet. Subsequently, the O^- reacts with propyne or allene to form the m/z = 38 anion. If the N_2O entrainment valve is turned off, the m/z = 38 signal disappears. Additional experimental details are provided in Chapter 5 and 6.

2.3 Time-of-Flight Mass Spectrometer

The apparatus is equipped with a Wiley-McLaren TOF MS for mass selection. After drifting 20 cm in the supersonic expansion, anions are perpendicularly repelled by a high-voltage pulse constituting the first electric field of a 2-m long Wiley-McLaren time-of flight mass spectrometer.[24] Because the anions being repelled have a significant extent (~5 mm) in the direction of this field, rather a finite volume and not from a point source, the length of the flight path in the mass spectrometer is not identical for all anions. Therefore, we use a potential distribution across the repelling field. This ensures that the ions traveling a longer distance have greater kinetic energies, and the ions with the same mass reach the anion-laser interaction region at the same time, independent of their starting positions. In this way, the amplitude of the repelling pulse is adjusted for spatial focusing (Wiley-McLaren condition) with a typical value of about - 700 V across an approximately three-inch gap. The timing of the repelling plate pulse with respect to the time of the opening of the pulsed ion source valve is optimized to maximize ion signals in the detection region. Upon entering the TOF MS, the ions pass through a 3-mm diameter orifice of the grounded electrode that also acts as a differential pumping stage between the source chamber and the rest of the instrument. The ions then enter the acceleration stack, where they are accelerated to +2300 V by 10 evenly spaced electrodes and are given a final kinetic energy of ~3 keV. While the Wiley- McLaren configuration allows high mass resolution, an important side effect is a significant energy spread arising from the finite extent of the initial ion packet in the direction of the extraction field.

The accelerated ions are steered by vertical and horizontal deflectors and spatially focused by a cylindrical einzel lens. Employment of a pulsed potential switch rapidly re-references the ions from +2300 V to earth ground when passing through the potential switch. The purpose of this

process is to keep the detector region with the imaging system at earth ground without floating the detector region at the existing 2.3-kV beam potential.[48] Using an inline microchannel plates, (MCP), detector, the time dependence of the ion signal is measured on a digital oscilloscope to acquire a mass spectrum of the anions. To find the optimal temporal overlap between the mass-selected anions and the laser beam in the ion-laser interaction region, we monitor the neutrals generated after photodetachment by deflecting the anions prior to the inline detector. Also, a set of horizontal deflectors provides a small correction to the ion trajectory prior to the ion-laser interaction region, which optimizes the VMI focusing. The pressure in the detection region, which is pumped by 230 l/s and 685 l/s turbomolecular pumps in parallel, is about $3x10^{-9}$ Torr under normal operational conditions.

2.4 Velocity-Map Imaging Photoelectron Spectrometer

The photoelectron imaging spectrometer is based on the original concept of Eppink and Parker.[26] Its high sensitivity is an advantage compared to other methods of photoelectron detection. The VMI analyzer is located at the spatial focus of the ion beam, where photodetached electrons are extracted perpendicular to the ion beam. The VMI assembly is composed of three oxygen-free high-conductivity copper electrostatic plates (a solid repeller, annular ground, and extractor), a 20- cm long electron flight tube, an annealed μ-metal, and a 40-mm diameter microchannel plate electron multiplier. The diameter and thickness of the three plates are 3″ and 0.03″, respectively. The ground and extractor plates have a 1″ central aperture. These plates are spaced by 1″. In order to repel the photodetached electrons, the repeller plate is pulsed between -10 and -150 V, depending on the desired electron kinetic energy range. The middle plate is held fixed at earth ground (0 V), and the typical voltage on the extractor is fixed between +30 and +450 V, a value

selected to extract photoelectrons toward the electron detector over the desired electron kinetic energy range under velocity-map imaging conditions. At optimized velocity-focusing conditions, the ratio of the $V_{repeller}$ to $V_{extractor}$ is -1:2.78. In addition, the extractor is electrically connected to the flight tube and the front plate of the electron detector to create a field-free flight region. The whole assembly is surrounded by μ-metal shielding to protect the photodetached electrons from external magnetic fields, which alter the trajectories of electrons.

After the photodetached electrons travel through the field-free flight region, they map onto a position sensitive detector, which includes a gated pair of 40-mm MCPs (gain ~ 10^6), a phosphor screen (Burle, Inc.), and a cooled (-11 ^{O}C) charge-coupled device (CCD) camera (LaVision). The kinetic energy and angular distribution of the photoelectrons determines the shape and distribution of the measured image, which is transferred to the computer by the DaVis image acquisition software. The imaging-quality MCPs (chevron configuration) are held at + 1350 V to minimize background signals and then are pulsed to + 2 kV for ~ 2 μs by a home-built pulser to have full gain of the signal. Additionally, the overlap timing between anion and laser beam is set at the center of the pulse of the MCPs to avoid the voltage instability. The voltage on the phosphor screen is kept +3 kV higher than the voltage on the MCPs, i.e., + 5 kV. To capture the image on the phosphor screen, we use the CCD camera. The camera has a wide angle lens, and therefore, the height needs to be adjusted to focus on the back of the phosphor screen (the image). Typically, the camera exposure time is 5 seconds for the sequence summing function and 500 ms for the event counting mode. The event counting mode utilizes the centroiding procedure, which finds the center of each electron impact (a few pixels in diameter) and reduces it to a single pixel. In contrast, the sequence summing function without centroiding collects data faster but with slightly worse energy resolution. In our instrument, the energy resolution, $\Delta E_k/E_k$, with centroiding is about 2% and

without centroiding is 3%. For 2% resolution, if the electron kinetic energy is 0.3 eV, then the ΔE_k will be 6 meV (i.e., 48 cm^{-1}). For electron kinetic energies below 0.1 eV, the spectral resolution cannot be less than 3 meV due to the velocity spread within the anion beam.

2.5 Laser System

The laser radiation for these photodetachment experiments include the fundamental (1064 nm), second harmonic generation (SHG, 532 nm), and third harmonic generation (THG, 355 nm) of the neodymium doped yttrium aluminum garnet (Nd:YAG, Coherent, Inc., Infinity) laser. To gain more tunability in the radiation used, we also employ a 532-nm pumped dye laser (PDL-1), 355-nm pumped optical parametric oscillator (OPO), and difference frequency generation (DFG). The various setups allow us to tune the radiation between the IR and UV and are described in more detail below.

In this thesis, the nanosecond Nd:YAG laser system operates at 80 Hz and typically outputs 5 to 300 mJ/pulse of 1064-nm light, depending on applications. The 1064-nm light can be doubled in a temperature-controlled type-I β-barium borate crystal (BBO) to generate 532-nm light. For THG, the 1064-nm and 532-nm light with the same polarization are combined in a second temperature-controlled type-I BBO crystal with different phase-matching angles to produce 355-nm light. In order to have the fundamental and SHG at the same polarization, a half-waveplate is used in the beam path between the SHG and THG crystals to rotate the 1064-nm polarization by 90° for the sum-frequency generation (SFG) process. By tuning the angle of the SHG and THG crystals, the power of 532-nm and 355-nm light can be optimized. This Nd:YAG laser also has a built-in 355-nm pumped OPO and BBO-based SHG stage for doubling signal or idler output from

the OPO, which provides a wavelength range of 220−2000 nm. The typical linewidth of the signal and idler light is 5−10 cm^{-1}; however, light near the degeneracy, 710 nm, has an increased linewidth, 20−100 cm^{-1}. To obtain a narrower linewidth spectra, the PDL-1 dye laser is used, and the schematic layout is shown in Fig. 2.3. In the dye laser, there are three cells, an oscillator, a pre-amplifier, and an amplifier. This dye laser can be side- or end-pumped by 532-nm light with vertical polarization, depending on the requirements of different dyes. The fundamental output of the dye laser can be doubled in an additional BBO crystal to generate UV light. This provides an optional wavelength range of 250−850 nm with energies of 0.1 to 30 mJ/pulse.

For the data obtained in Chapter 4, we needed mid-IR 3236-nm light, which cannot be produced by the setups discussed above. Therefore, we configured a DFG setup to produce the mid-IR light by mixing 801-nm light (from the 532-nm pumped LDS798 dye laser) with the residual 1064-nm light in a 1x1x3 cm^3 magnesium oxide doped lithium niobate ($MgO:LiNbO_3$) crystal. The schematic is depicted in Fig. 2.3. The $MgO:LiNbO_3$ crystal, purchased from the United Crystals Inc., has type-I phase-matching angle at 44.1°, an AR-coating at 1064 nm and 750 – 830 nm on the entrance surface, and AR-coating at 2500 – 3800 nm on the exit surface. The 801-nm and 1064-nm lights have to simultaneously reach the non-linear crystal, i.e., the same traveling distance. The polarizations of the dye laser output and 1064-nm light are vertical and horizontal, respectively, and therefore, the resulting polarization of mid-IR light is horizontal. Using a band filter to absorb 801-nm and 1064-nm lights, the power of the 3236-nm light can be monitored by a power meter and optimized by tuning the phase-matching angle of the $MgO:LiNbO_3$ crystal. The mid-IR light, energy between 50 and 100 μJ/pulse, is focused into the anion-laser interaction region using a 1-m CaF_2 lens. We measure the dye wavelengths using a wavemeter (Atos, LRL-005)

calibrated by a He-Ne laser. Based on the dye wavelength, we then calculate the exact mid-IR wavelength: $\frac{1}{\lambda_{\mathrm{mid-IR}}} = \frac{1}{\lambda_{\mathrm{Dye}}} - \frac{1}{\lambda_{1064\,\mathrm{nm}}}$.

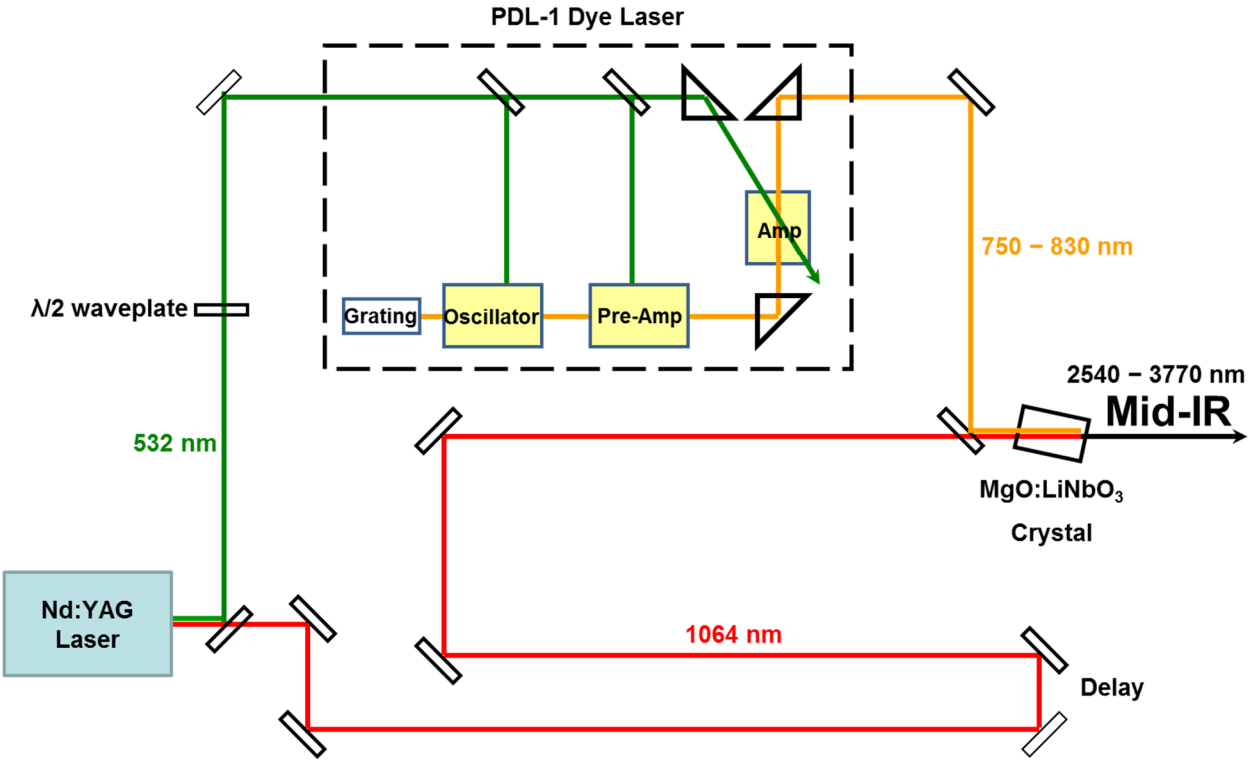

Figure 2.3 Schematic layout of mid-IR generation utilizing a Coherent Infinity Nd:YAG laser and a QuantaRay PDL-1 dye laser. The dye cells (yellow) in the day laser are pumped by the 532-nm light (green), which laser polarization is flipped to be vertical using a half-wave plate. The residual 1064-nm light (red) with horizontal laser polarization is aligned through the $MgO:LiNbO_3$ crystal, and is mixed with the dye laser output (orange) to generate a mid-IR light with horizontal laser polarization. The delay stage is used to simultaneously get both lights to the non-linear crystal, i.e., the same traveling distance. The power of the mid-IR light is optimized by rotating the phase-matching angle of the $MgO:LiNbO_3$ crystal.

For the reconstruction of the photoelectron image in this experimental setup, the laser polarization is required to be parallel (horizontal polarization) to the imaging MCPs and at the correct height to enter the vacuum chamber. Therefore, vertically polarized light is rotated 90° by a twisted periscope, in which two mirrors are perpendicularly arranged, and horizontally polarized light only has the height adjusted by a normal periscope, parallel arrangement of two mirrors. Before the laser beam is aligned through the anion-laser interaction region, the laser power is reduced to 0.1 – 3 mJ/pulse to avoid "drilling" the exit window on the chamber. To further avoid damaging the exit window, the light is softly focused through the detection region with a 1-m focal length lens. The overlap timing of the laser with the anion beam is adjusted by a Stanford Digital Delay pulse generator (Stanford Research, DG535), set to obtain the strongest detachment signals. The laser-light wavelengths are measured using a wavemeter (Atos, LRL-005) calibrated by a He-Ne laser or using the known spin-orbit splittings of atoms, such as I and S, from the measured photoelectron image.

2.6 Data Analysis

Following photodetachment of the electrons, the three dimensional (3-D) laboratory frame photoelectron distribution is projected onto a two dimensional (2-D) imaging MCP detector, which is digitized by the DaVis camera software, and transferred to a computer for analysis. The raw 2-D images must first be reconstructed back into the nascent 3-D photoelectron distribution. This is accomplished by using the basis set expansion (BASEX) Abel inversion software package developed by Dribinski *et al.*, which ultimately converts the raw 2-D photoelectron images into nascent 3-D velocity and angular distributions.[49] The velocity distribution is the angle-integrated intensity as a function of radial pixel (typically half pixel) from the center of the ring image. Hence,

the center of the photoelectron image is very crucial that a symmetrization procedure is developed. Take vertical symmetrization of the bottom half of the image as an example; we get rid of the top half of the image, duplicate the data of the bottom half, flip it vertically, and paste it back onto the top half. The center is determined by using different (x,y) coordinates to carry out vertical symmetrization of the image until velocity distributions of symmetrized images are matched. Likewise, horizontal symmetrization is carried out using left and right half of the image. Both the signal and background images are individually reconstructed by the BASEX using the same center. If the quadrant-symmetrized or symmetrized image results in a photoelectron spectrum with better signal-to-noise ratio or lower uncertainty, we report those data.

To obtain the photoelectron spectrum in terms of the electron kinetic energy, eKE, the velocity domain photoelectron spectrum is transformed to the energy domain using the appropriate Jacobian transformation, Eq. 2.1.,

$$I(E) \propto I(v)/v \tag{2.1}$$

where v is velocity. In addition to the electron velocity distribution, the reconstructed images contain the differential cross section, which provides the photoelectron angular distribution with respect to the cylindrical symmetry axis, defined by the laser polarization direction. Anisotropy parameters obtained from the photoelectron angular distributions are useful to assign electronic states of neutral molecules and were discussed in Chapter 1.

The calibration of the energy scale for the reported data is performed using well-known peak energies. In particular, EAs and spin-orbit splittings of atomic species are mostly used in these experiments because of narrower peak widths due to a lack of an internal energy. We report photoelectron spectra as a function of electron binding energy (eBE= $\hbar\omega$ – eKE), which is independent of the laser wavelength used for photodetachment. Figure 2.4 demonstrates the 532

nm (2.330 eV) photoelectron spectrum of S^-, which is used for calibration.[50-52] The spectrum is reconstructed from the quadrant-symmetrized photoelectron image with centroiding. The S^- anions are produced by dissociative electron attachment of CS_2 with slow secondary electrons. The observed peaks, labeled a through f, are well-separated, and the corresponding transitions are shown in the inset. The spectral resolution is about 2% and defined as $\Delta E_k/E_k$, in which ΔE_k is the measured energy width of the peaks and E_k is electron kinetic energy at the center of the peak.

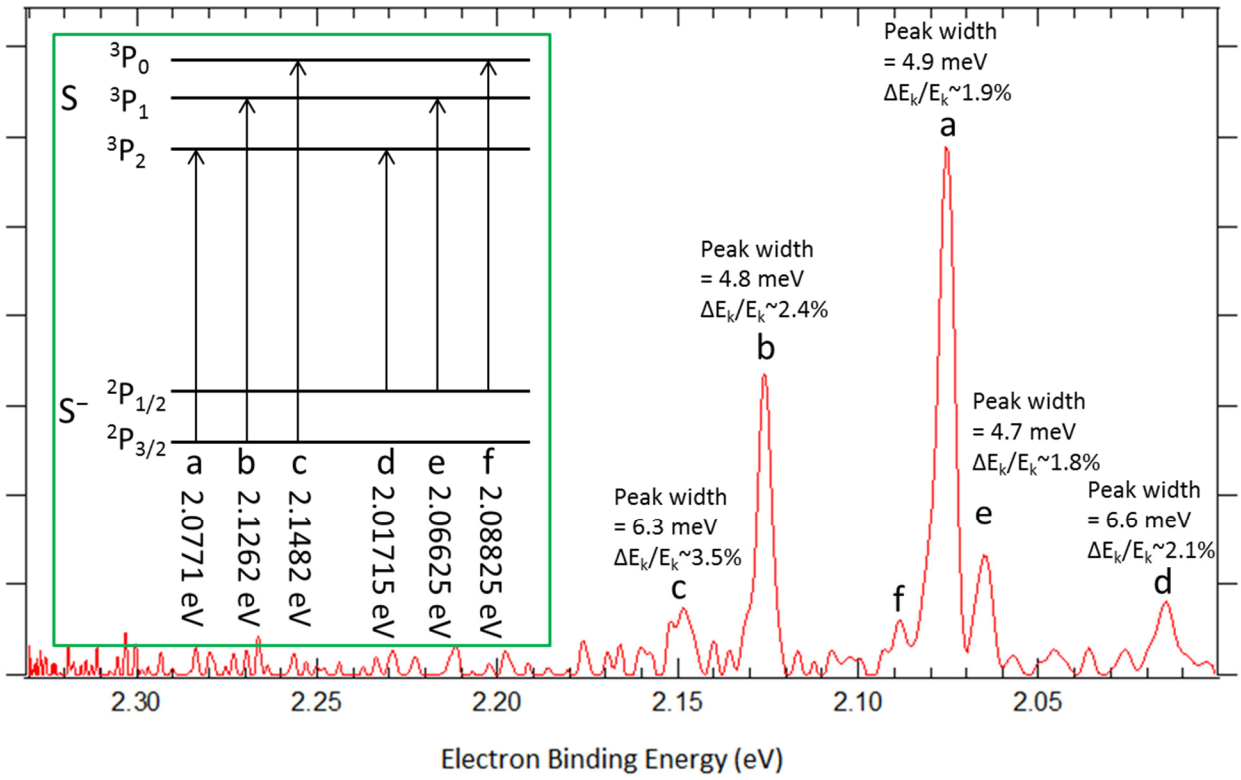

Figure 2.4 Photoelectron spectrum of S^- at 532 nm. The spectrum is reconstructed from the quadrant-symmetrized photoelectron image. The peaks are labeled a through f, and the peak widths are also shown. The corresponding known transitions are presented in the inset.

Chapter 3
Versatile, Pulsed Anion Source Utilizing Plasma-Entrainment: Characterization and Applications

3.1 Introduction

Negative ion photoelectron spectroscopy has been widely applied to investigate the spectroscopic properties of neutral species[2-4] and the dynamics of photodissociation,[6,9] cage recombination,[5,7] S_N2 reaction,[8] isomerization,[11] and charge transfer.[10,12] In order to study extensive aspects, a variety of anion sources have been developed for continuous wave (cw) and pulsed instruments. The flowing afterglow ion source,[53-56] which has great capabilities for multistep ion syntheses, was adapted from the conventional continuous anion-laser beam photoelectron spectrometer.[57,15] However, no pulsed anion sources have attempted to carry out rational ion syntheses in a supersonic expansion. In this chapter, we characterize the design of a novel, pulsed anion source based upon entrainment of ions and/or electrons using a plasma source. This pulsed anion source permits multistep syntheses of cold anionic species that are very difficult to produce using conventional pulsed anion sources. Some applications of the development are also demonstrated.

A pulsed anion beam is typically constructed using a pulsed supersonic jet that coaxially or perpendicularly collides with a continuous beam of 1-keV electrons from an electron gun.[27] For the formation of some anions, an electrical discharge source[28-31] or a laser vaporization source[32-35] is required and results in a high temperature environment. All of these sources use a main pulsed expansion to create ions. Generally, a supersonic expansion of molecules in a carrier gas leads to sufficient cooling of the internal degrees of freedom for high-resolution spectroscopic applications. However, a gas expansion that passes through a hot plasma, for example, contains too many energetically excited species to completely cool the anions formed. The insufficient internal

cooling of anions in the supersonic anion jet broadens peaks and, possibly, generates dense spectra, both of which raise the difficulty of extracting spectroscopic information.

There are two methods to reduce the internal energy of the anions studied, the Ar-tagging technique[46,58] and cryogenic ion trapping.[59,60] For the Ar-tagging technique a "cold" subset of the anions are selected. Since Ar atoms weakly bind to anions, mass selecting for anion-Ar clusters limits the internal energy of the anion, suppressing hot bands and reducing spectral congestion.[61-64] The supersonic entrainment technique is often employed to attach Ar solvent atoms to anions and build large complexes. The Ar atoms are boiled off to cool the anion, thus the anions in the large clusters have low internal energy.[46] Another method is to use a cryogenic ion trap. In this method, an ion beam is stored in a low-temperature environment for milliseconds or seconds, which is capable of cooling ions *via* radiative relaxation or collisions with a cold buffer gas. The resulting cold anions are released from the trap having low internal energies. Using a cold ion technique can increase the resolution of photoelectron spectroscopy to obtain more accurate spectroscopic properties of neutral molecules. Although both of these methods have ion-cooling capability, they do not allow for great control over rational anion syntheses, as in the flowing afterglow source.

Yet another method, the continuous pick-up method, is capable of making cold anionic clusters. The cluster anion of the $O^-(Ar)_n$ ($n = 0 \sim 34$) has been formed in a continuous expansion of about 9-atm Ar gas, maintained at 196 K, that has been intersected with O^- (made by the interaction of electrons, emitted from a filament, with N_2O gas).[65] One can expect that O^- was picked up by neutral Ar clusters that were formed in the cold, condensed Ar gas tank. Other ion sources have been employed to investigate large ionic systems relevant to the condensed phase. Electrospray ionization (ESI) sources are frequently used to transfer ionic species from solution

into the gas phase. These ions can then be mass-selected, stored, and cooled in a cryogenic ion trap *via* collisions with a cold buffer gas for further different measurements.[36-39] Additionally, Rydberg electron transfer[66] and a laser-assisted desorption technique[67] have been used to attach electrons to nucleobases and amino acids, respectively.

In this chapter, a detailed description of the pulsed plasma-entrainment anion source is given. Its performance is documented with a variety of applications. This anion source utilizes two pulsed valves: one serves to create the supersonic expansion, the other is placed perpendicular to this main expansion and utilizes an electrical discharge. Anions are made in a side pulsed discharge that creates a violent, high-energy environment. The Ar beam picks up the anions in a region of high density, providing collisional cooling to the anions. It is informative to explore the many uses of such a source. This pulsed anion source has successfully generated $OH^-(Ar)_n$ (n = 0 ~ 32), and we obtain the photoelectron spectra of n=0–3, 7, 12, and 18. Further, using this anion source, we are able to perform condensation reaction, and we demonstrate this by producing $HOCO^-$ isomers and CH_3OO^-. The photoelectron spectra of bare $HOCO^-$ are presented and compared to the published spectrum taken under a cryogenic environment.[68] Lastly, the photoelectron spectra of CH_3OO^- formed by an association reaction in this pulsed anion source and by a proton abstraction reaction in a continuous anion source,[69] are compared, illustrating the possibilities of making transient species through rational chemical means.

3.2 Anion Source Details

A thorough description of the apparatus can be found in Chapter 2; the design of the plasma-entrainment anion source is described here in more detail. Figure 3.1 shows a schematic arrangement of this pulsed anion source. The setup employs two pulsed General Valves (Parker-

Hannifin, series 9): one functions to generate the supersonic expansion, and the other is oriented perpendicular to this main expansion and utilizes an electrical discharge. Since the two valves are independently controlled by a commercial multi-channel Iota-1 driver and a digital delay generator, temporal overlap of the two gas pulses can be adjusted in real time. A plasma is created in an electric discharge that is mounted onto the faceplate of the side valve, and is introduced at a distance of about 3 mm beyond the faceplate of the main valve. The side discharge nozzle operates under choked-flow conditions (the gas throughput is roughly one order of magnitude less than that from the main valve) with a 250-μs gas pulse, and entrains plasma into the main expansion of Ar. The Ar acts as a carrier gas and provides additional collisional cooling. The principle of supersonic entrainment was first characterized and extensively studied by Campargue; it was determined that gas outside the shock-wave structure of the jet was drawn into the free-jet zone of silence far from the orifice.[45] This study confirms that the low-density gas from the side pulsed valve does not disturb the main Ar expansion, and that it is possible to entrain electrons, cations, anions, radicals, and solvent species into the main Ar expansion. In order to measure the time spread of the ion packet that is entrained into the main expansion, we vary the timing of the extraction plate that directs anions down the time-of-flight mass spectrometer; we find that the temporal FWHM of the ion-packet is about 20 μs, indicating a small spatial coverage of ions.

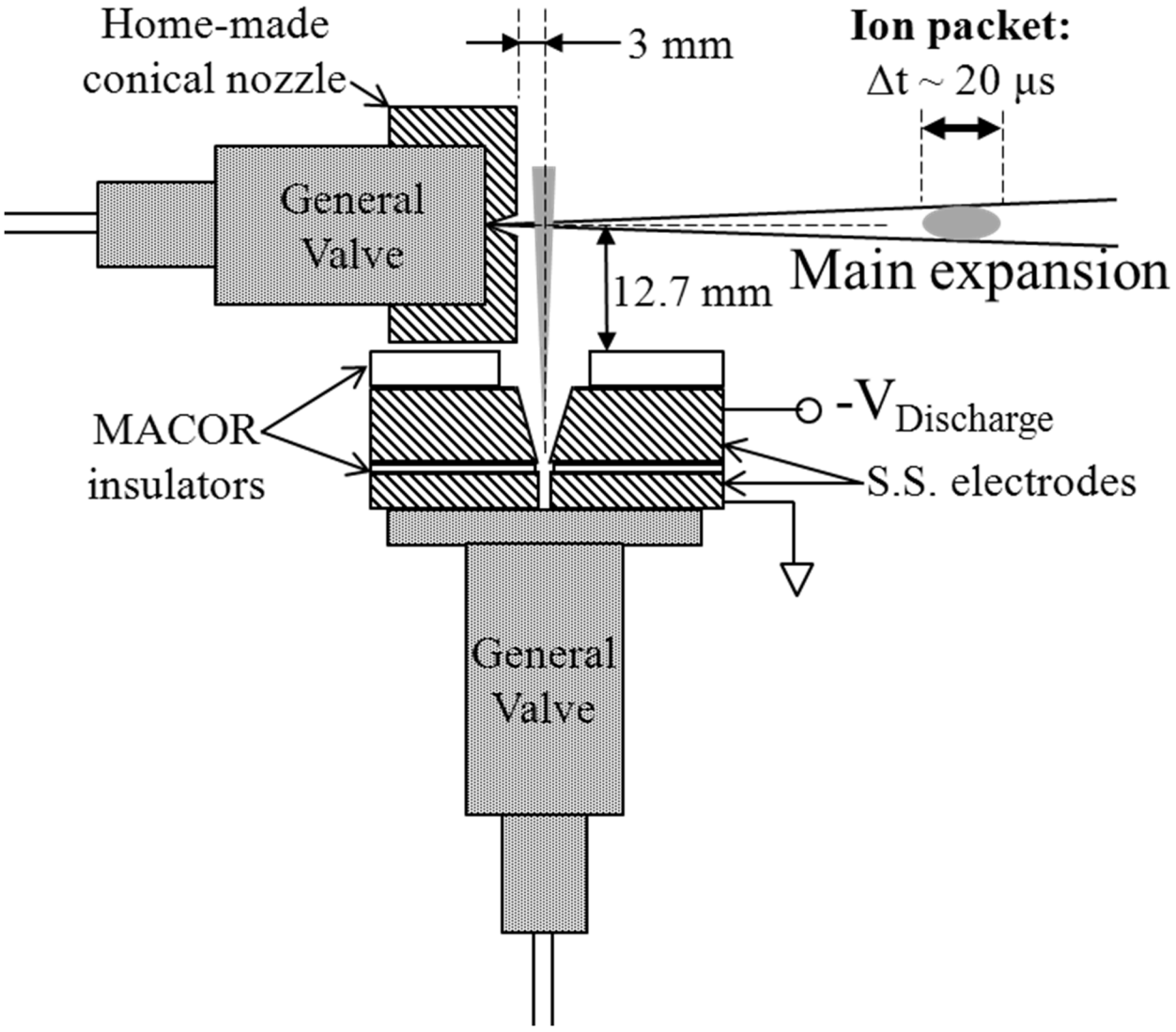

Figure 3.1 Schematic arrangement of the pulsed anion source. The source is capable of entraining ions from a side expansion.

In order to increase the forward intensity of the main expansion, we use a 40° conical nozzle with a 0.5-mm orifice (D_O) and an aspect ratio (L/D_O) of 7.[70] The nozzle seals in a similar fashion as a commercial faceplate and, thus, couples well with a General Valve body. Even though we run the pulsed discharge at a duration time of 140 μs to produce a large quantity of anions, internally cold anions can also be generated in the main expansion after entrainment. Furthermore, sequential addition of neutral reactants to cold anions provides for the possibility of implementing stepwise ion syntheses in the pulsed expansion. This new source gives multiple pathways to the formation of a wide variety of anions prior to extraction into the TOF MS and VMI detector.

The pulsed discharge source is comprised of two stainless steel electrodes, one is attached to a commercial General Valve faceplate (0.8-mm orifice) held at ground and the other is pulsed to negative high voltage; a cylindrical MACOR plate insulates the two place from each other. A second MACOR ring is added at the end of the whole assembly. The grounded S.S. electrode has an inner channel with diameter of ø0.04″ and a thickness of 0.075″. The inner channel diameter of the MACOR insulator in between the two electrodes is ø0.06″, and its thickness is 0.04″. The S.S. electrode that is pulsed to high negative-voltage has a 40° conical nozzle with a ø0.04″ orifice diameter and a thickness of 0.32″. The inner diameter and thickness of the final MACOR ring are ø0.39″ and 0.15″, respectively. Each plate has four holes, which hold the whole stack together using nylon screws. The outer diameter of all the plates is ø1.5″. Appendix A shows a schematic drawing of the home-made nozzle and all the discharge components. Appendix B gives a blow-out figure of the discharging region. We use a pulsed voltage between -800 and -2000 V to maximize the ion intensities and the stability of the discharge. The negative-voltage pulse is provided by a pulse generator (Directed Energy, Inc. (DEI), GRX-3.0K-H) with a DC power supply (Bertan associates, Inc., 205-03R). The pulser (triggered by a digital delay generator)

controls the discharge timing and pulse duration, both of which are adjusted to optimize the ion intensities. Additionally, using two 10kΩ resistors in series with the cathode increases the discharge stability. Time traces for the pulser output voltage and the voltage measured across the electrode for a -2 kV, 40-μs discharge are shown in Fig. 3.2, with an inset illustrating the circuit diagram. When -2 kV (in a 40-μs pulse) is applied through the two 10 kΩ resistors, the voltage drop across two resistors is -1.5 kV, corresponding to a discharge current of 75 mA. The ballast resistor depicted allows the -2 kV between the plates to initiate the discharge, but then limits the discharge current to a maximum of 100 mA, providing current regulation and arc suppression.

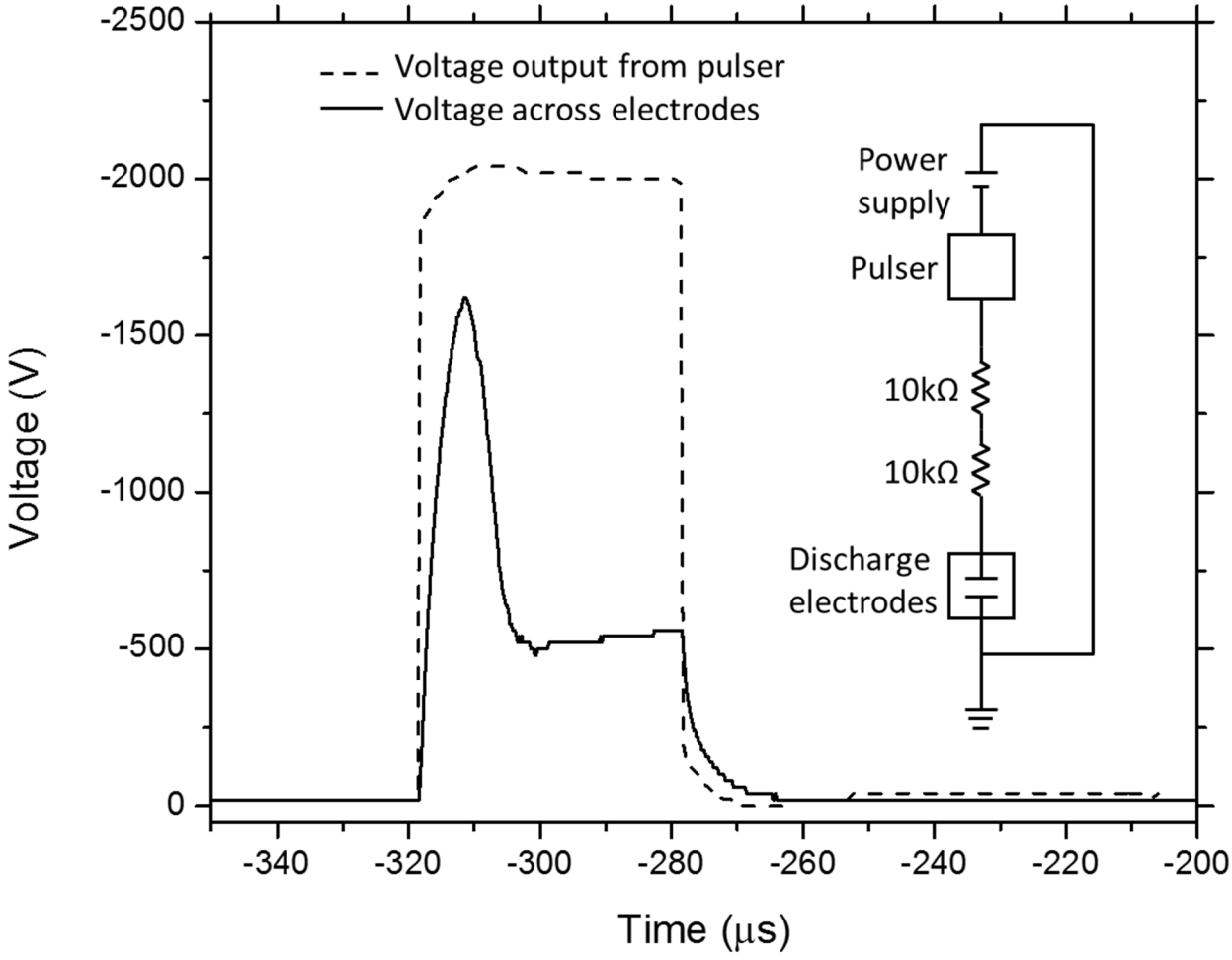

Figure 3.2 Time trace of a -2kV discharge voltage for OH^- production. Through two 10kΩ resistors, the voltage drops about 1500 V, which corresponds to the peak discharge current of 75 mA. The inset represents the circuit diagram, in which the discharge electrodes are under vacuum condition in the source chamber.

For the preparation of the desired anions, a suitable gas mixture is crucial. For example, OH^- is readily formed in the discharge of 1% O_2 and 25% H_2 in Ar at a backing pressure of 4.7 atm. We use this mixture to study $OH^-(Ar)_n$ clusters; Appendix C lists the experimental conditions of $OH^-(Ar)_n$ cluster formation. We have also tried various combinations of $N_2O/CH_4/Ar$, $N_2O/H_2/Ar$, and $O_2/CH_4/Ar$ for OH^- production; however, in all cases the discharge of these gas mixtures produce OH^- intensities that are less intense than the $O_2/H_2/Ar$ mixture. Furthermore, for these mixtures many N_2O– or CH_4–solvated anionic complexes, e.g., $OH^-(N_2O)_n$ or $OH^-(CH_4)_n$, also form at a number of mass-to-charge ratios, resulting in an undesirable background. The gas mixtures used in the formation of various other anions will be pointed out in each section.

3.3 Results and Discussion

In this section, we demonstrate the performance of this pulsed anion source using mass spectrometry and photoelectron spectroscopy. First, we discuss electron entrainment into the main expansion from the side valve. Then, we present and discuss photoelectron spectra of CH_3^-, $OH^-(Ar)_n$, $CH_3O^-(Ar)$, $CH_3O^-(H_2)_n$, $HOCO^-$, and CH_3OO^- to confirm our ability to make a wide array of cold anion with this novel anion source.

3.3.1 Electron Entrainment

After initiating a discharge in the side expansion, the gas forms a plasma (a neutral medium consisting of many charged particles: electrons, cations, and anions) with a Debye shielding length which is much shorter than the physical dimension of the plasma. These electrons will become entrained into the main expansion, making the formation of anions by attachment to neutral molecules in the supersonic jet possible. However, the charged species of a plasma do not move independently. The electric field of the quickly moving electrons drags ions along with them,

creating an ambipolar diffusion that results in the electrons and ions having the same diffusion rate.[71] This ambipolar diffusion makes it possible to form anions through attachment of slow entrained electrons. We demonstrate this in Fig. 3.3, which shows a comparison between two mass spectra obtained using neat Ar (black) and 1% O_2 in Ar (red) in the main expansion. In both cases, neat Ar is used in the side discharge source (-2 kV in a 140-μs pulse). The addition of O_2 in the main expansion causes the formation of O^- and O_2^- anions, reinforcing the electron-entrainment application of this pulsed anion source. It is worth noting that the ion intensities obtained are at least as intense as other common sources, making this method a plausible way to form anions without too much unwanted "heating" of the anions.

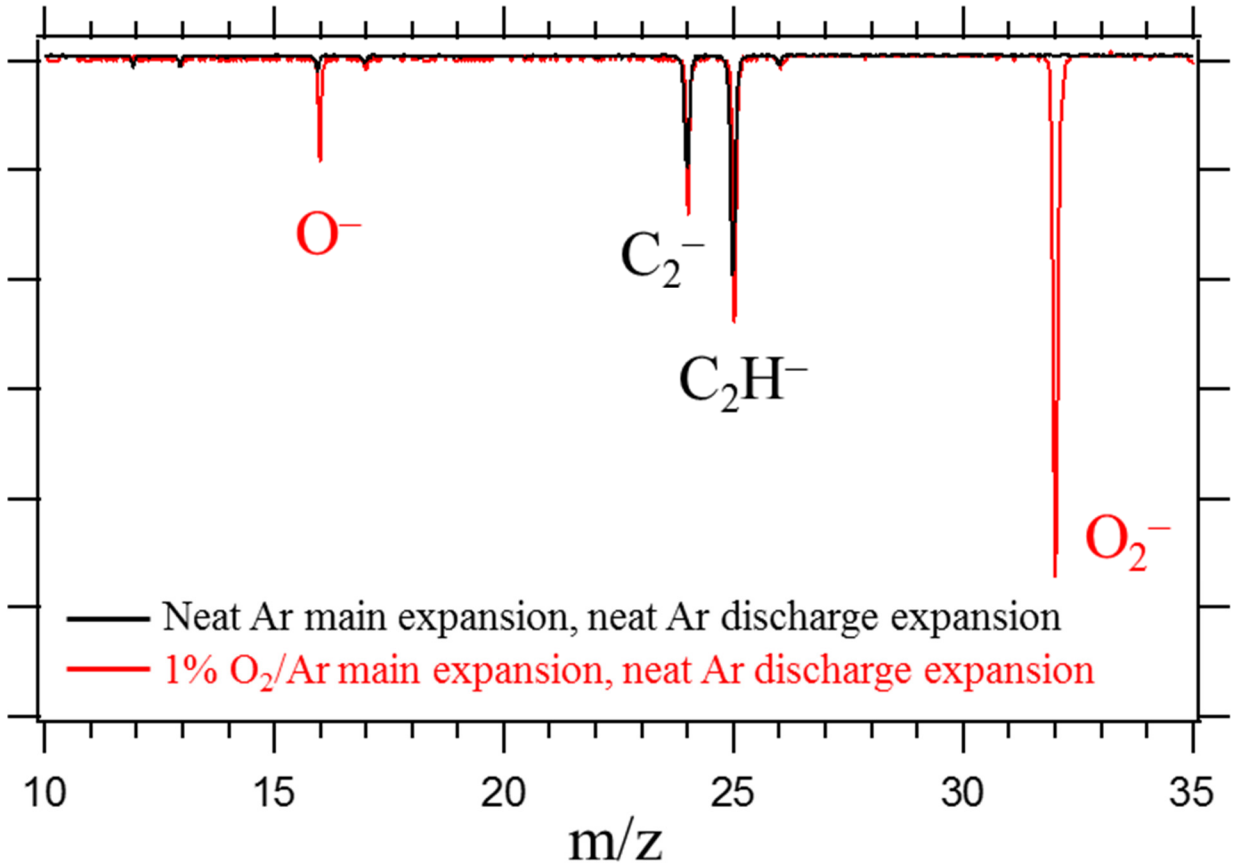

Figure 3.3 Comparison between TOF mass spectra from experiments using neat Ar (black) and 1% O_2/Ar (red) for the main expansion. Neat Ar gas is used for both experiments in the side discharge source. Entrainment of electrons is demonstrated from the additional formation of the O^- and O_2^- anions.

3.3.2 Exotic Species: CH_3^-

Using conventional pulsed anion sources, it is extremely challenging to produce CH_3^-. However, this pulsed ion source provides a straightforward way for making cold CH_3^-. In 1978, Ellison *et al.* successfully measured the photoelectron spectrum of CH_3^- (formed in a discharge) and determined the EA of the methyl radical.[72] The CH_3^- spectrum revealed an extensive progression in the out-of-plane bending (umbrella) mode of the methyl radical in its electronic ground state. In this experiment, we use an electrical discharge of neat CH_4 gas in the side pulsed valve, and in the main valve we have a neat Ar expansion (3.7 atm). The pulsed electrical discharge takes place when the CH_4 gas passes through a stainless steel cathode, which is pulsed (140 μs) at a potential of -900 V in series with two 10kΩ resistors (for increased discharge stability), to a stainless steel grounded anode. The ions formed are then picked up by the Ar expansion and further cooled. Interestingly, CH_3^- anions were not observed using a dilute gas mixture of 3% CH_4 in Ar in the discharge; see Fig. 3.4. Figure 3.5 presents the photoelectron spectrum of CH_3^- using 1064-nm (1.165 eV) radiation. This spectrum is consistent with the previous spectrum taken in 1978, and further discussions on this system can be found in Chapter 4.

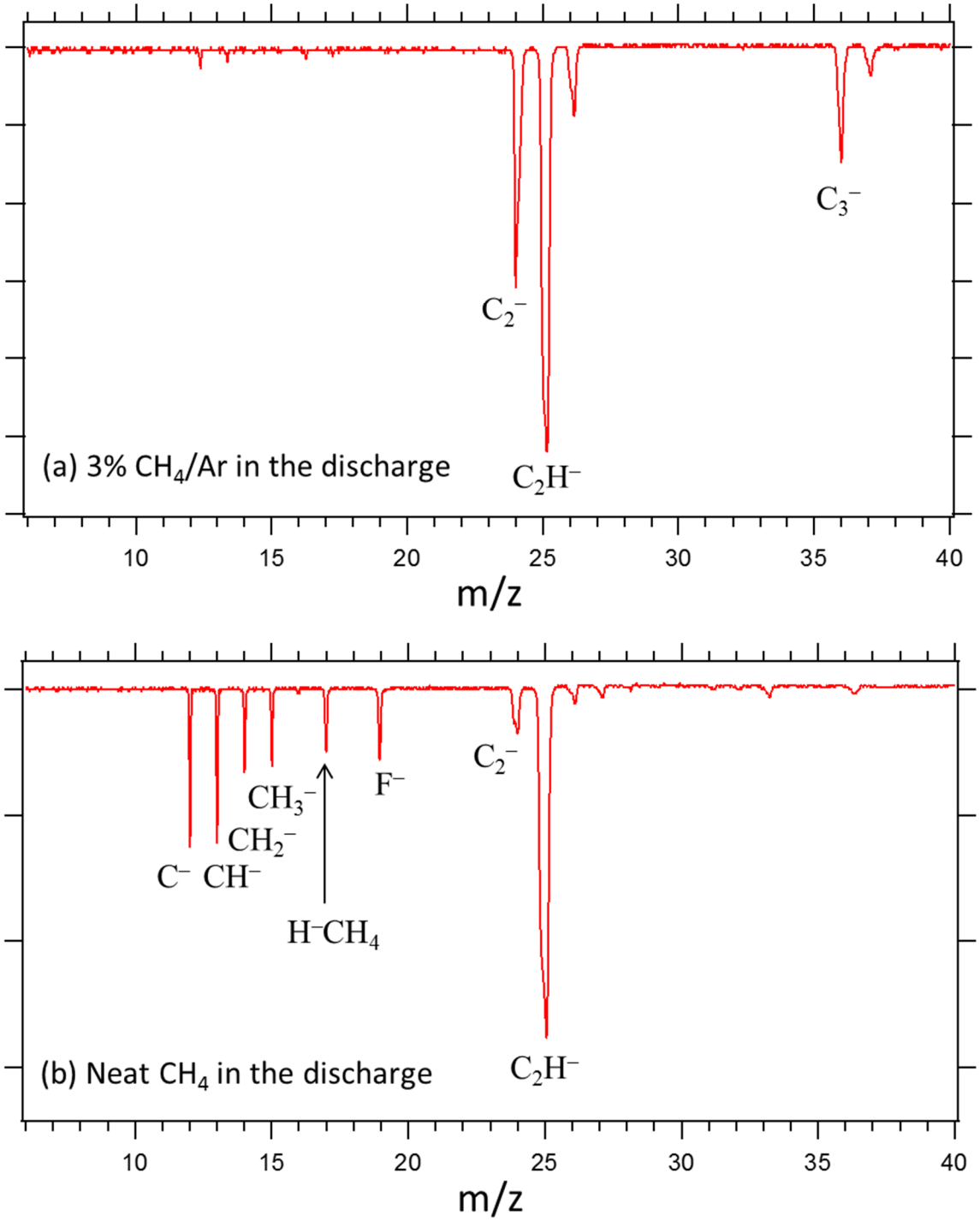

Figure 3.4 Time-of-flight mass spectrum from experiments using (a) 3% CH_4/Ar and (b) neat CH_4 in the side discharge source. Neat Ar gas is used as the main expansion for both experiments. The chemical identity of the mass-selected anions is confirmed by comparing their photoelectron spectra with other known anion photoelectron spectra. F^- comes from chemical contamination in sample line.

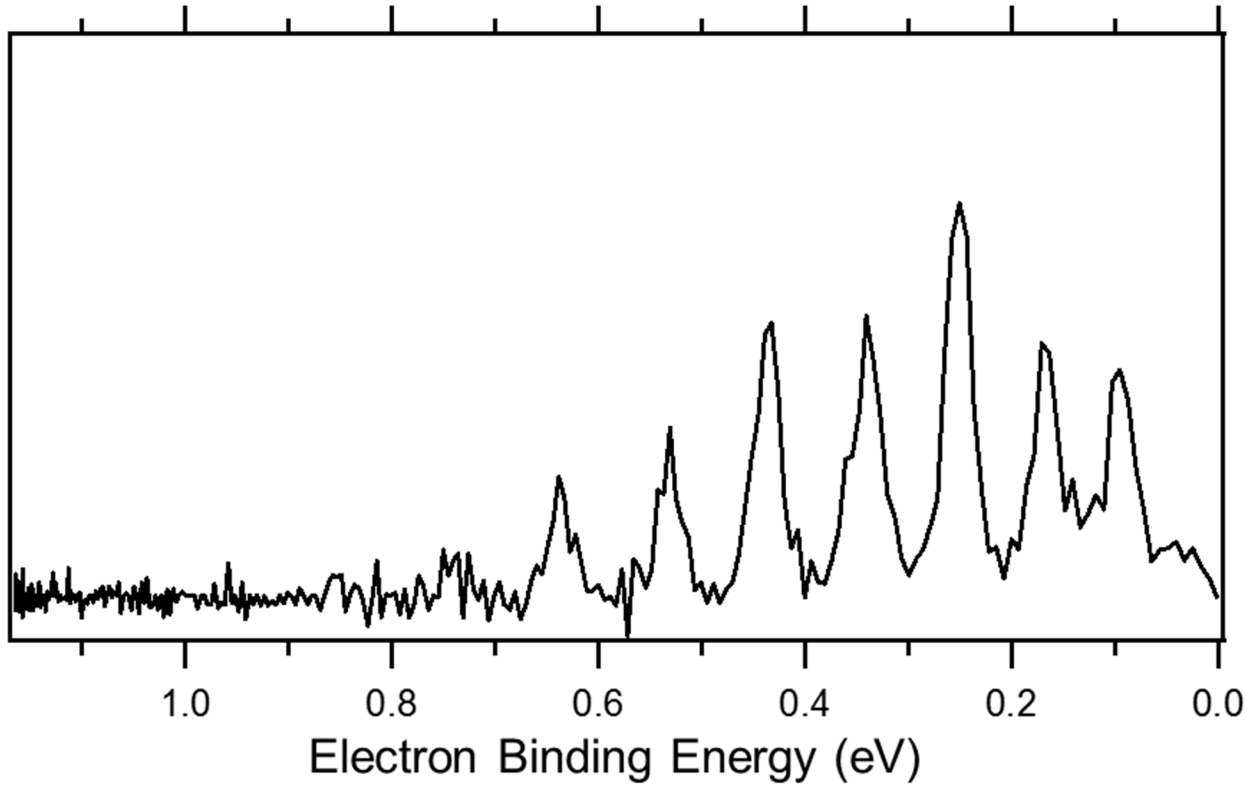

Figure 3.5 The 1064-nm photoelectron spectrum of CH_3^- showing an extensive progression in the out-of-plane bending (umbrella) mode of CH_3.

3.3.3 Ar-tagging: $OH^-(Ar)_n$

Figure 3.6 shows composite mass spectra of Ar-tagged OH^- ranging from 0 to 32 Ar atoms, $OH^-(Ar)_{n=0-32}$. Below m/z=50, three predominant peaks occur: O^-, OH^-, and O_2^-. These ions are formed in the discharge source and drawn into the main expansion of neat Ar. Once in the main expansion, some of the OH^- anions cluster with Ar atoms generating $OH^-(Ar)_n$; the portions of the mass spectrum showing $7 \leq n \leq 32$ are magnified and shown in two insets. The peaks for n = 12 and 18 are prominent, suggesting that 12 and 18 are "magic numbers" that indicate a particularly stable cluster geometry.[73,74] These magic numbers (of 12 and 18) are also observed in $O^-(Ar)_n$ and correspond to the closing of the solvation shell in an icosahedral (12 Ar atoms) and double icosahedral (18 Ar atoms) structure.[65] Similar solvation shells likely account for the peak intensities observed for n = 12 and 18 in the $OH^-(Ar)_n$ mass spectrum.

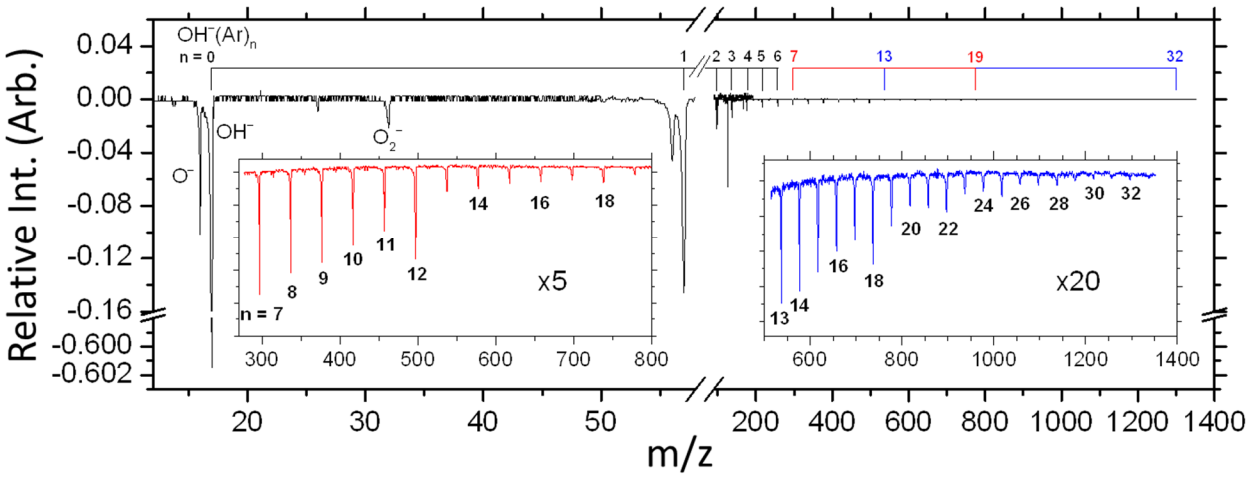

Figure 3.6 Composite mass spectra of $OH^-(Ar)_{n=0-32}$. The insets show the color-coded 5x (red curve) and 20x (blue curve) magnifications of the selected mass spectral region to better view the cluster distribution and magic numbers of n = 12 and 18.

Figure 3.7 shows a series of representative photoelectron spectra for $OH^-(Ar)_n$ –clusters with n =0, 1, 2, 3, 7, 12 and 18 are obtained using three different photodetachment wavelengths: 459 (2.703 eV), 532 (2.330 eV), and 602 (2.060 eV) nm. In the photoelectron spectrum of bare OH^-, the rotational branches of the OH radical in the $^2\Pi_{3/2}$ and $^2\Pi_{1/2}$ states are resolved. In the spectra for all of the complexes, there is a single broad peak that shifts to higher electron binding energy with an increasing in the number of Ar atoms. The peak shift is a result of the greater binding energy of the solvent to the anionic cluster than to the neutral cluster. Solvation by the first Ar atom increases the electron binding energy by about 0.12 eV. The next two consecutive Ar additions (n=2 and 3) shift the vertical detachment energy (VDE) by about 0.07 eV. Thus, the VDE of $OH^-(Ar)_3$ is 0.07 eV higher than the VDE of $OH^-(Ar)_2$, 0.14 eV above the VDE of OH^- Ar, and 0.26 eV above the EA of OH. The solvation energies for the various cluster sizes studied are shown in the Fig. 3.7, and demonstrate that the average solvation energy per Ar atom decreases as the cluster size increases. Since Ar atoms in outer solvation shells interact less with the localized negative charge, the addition of Ar atoms beyond n=12 only shifts the VDE minimally; in fact, the difference in the VDE of n = 12 and n = 18 is only ~0.06 eV, suggesting an averaged size-dependent binding energy of 0.01 eV per Ar atom. This solvation behavior is consistent with studies of $I_2^-(Ar)_n$ and $O^-(Ar)_n$ clusters.[65,61]

The FWHMs of the photoelectron peak in the spectra of all the cluster sizes are similar (approximately 0.06 eV) and twice as broad as that of the bare OH^- peak (about 0.027 eV). Recall that the peak FWHM reported here is dependent of eKE, since the spectral resolution in VMI spectrometer degrades with increasing eKE (decreasing eBE). Hence we use three different wavelengths for the various clusters in an attempt to make a fair comparison of the FWHM. In order to understand the peak broadening that occurs upon complexation of OH^- with Ar, it is useful

to begin with the simpler and analogous system, O^-(Ar). Garand *et al.* has assigned the EA of O(Ar) and deduced[75] that the solvation-energy shift from the EA of O is about 700 cm^{-1}. Using theoretical simulations, they determined an increased O–Ar bond distance of 0.371 Å, changing from 2.976 to 3.347 Å, upon photodetachment. The slow electron velocity-map imaging (SEVI) spectrum of O^-(Ar) resolved the fundamental vibrational frequencies of the neutral (31 cm^{-1}) and the anionic (86 cm^{-1}) ground state. In comparison to the O(Ar) complex, the neutral and anionic OH(Ar) clusters have a low HO–Ar stretching frequency and even lower frequency bending vibrations, making it much more difficult to resolve these transitions. Furthermore, any rotational excitation in the OH^-(Ar) cluster will also lend to the difficulty. As a result, the observed broadening is believed to arise from unresolved low-frequency vibrational modes of the neutral and/or initial excitation of the low-frequency internal degrees of freedom of the anion. However, it is possible that the broadening is due to the Franck-Condon overlap, causing the anion (in its ground state geometry) onto the repulsive wall of the neutral because of a large change in the equilibrium geometry between the anion and neutral species. Additional efforts for high-resolution experiments need to be made to understand the true reason of the peak broadening.

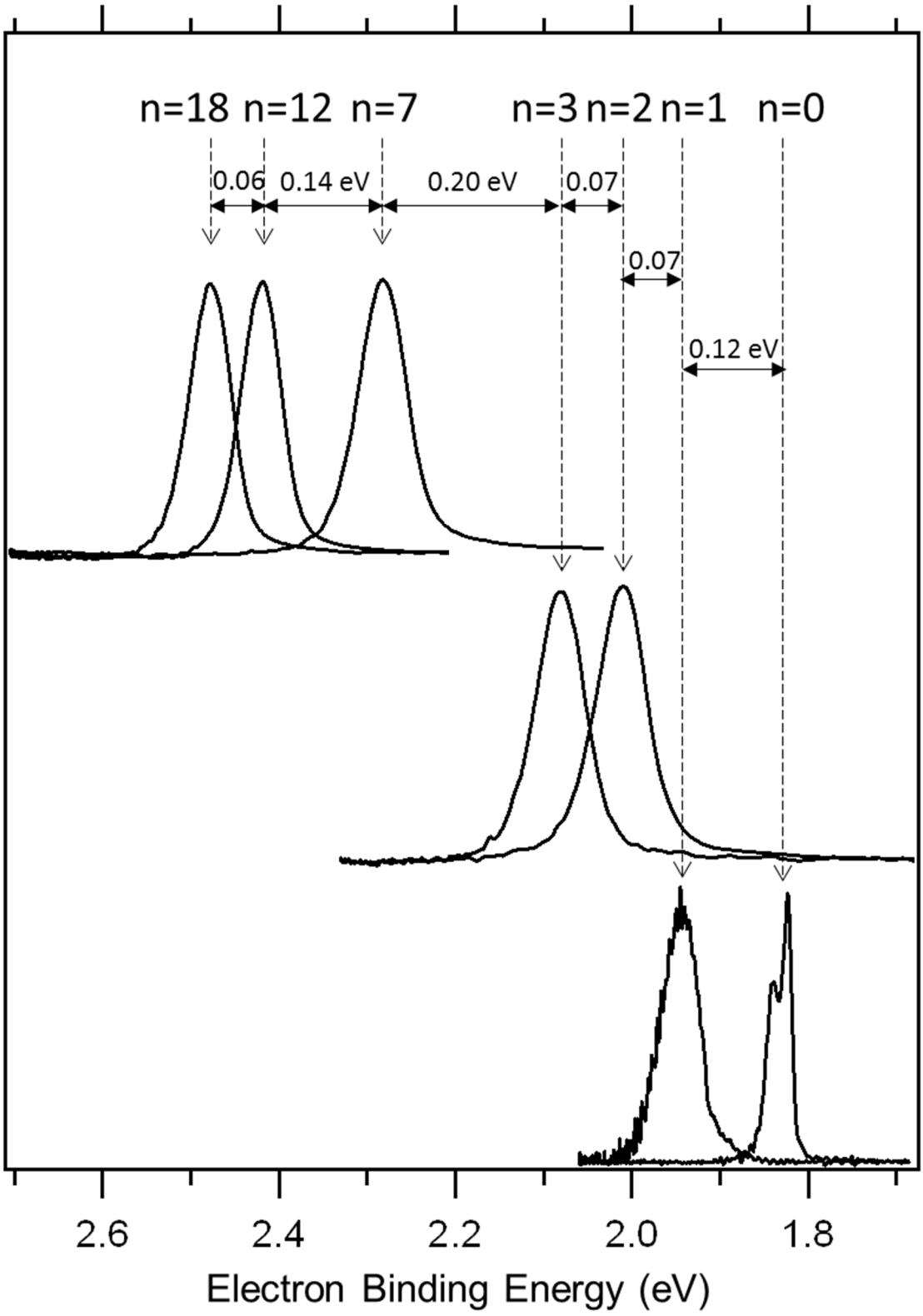

Figure 3.7 Photoelectron spectra of $OH^-(Ar)_{n=0,\ 1,\ 2,\ 3,\ 7,\ 12,\ and\ 18}$ at three different wavelengths: 459 (top), 532 (middle), and 602 (bottom) nm.

3.3.4 H_2-tagging: $CH_3O^-(H_2)_n$

Using this pulsed anion source, we have successfully attached one Ar atom and up to three H_2 molecules on CH_3O^-, yielding $CH_3O^-(Ar)$ and $CH_3O^-(H_2)_{1-3}$ clusters. By comparing these complexes, we gain insight into the different solvation effects of Ar and H_2. In particular, H_2 has a smaller polarizability than Ar; thus, we expect a weaker interaction and perturbation from H_2 than Ar. We also hope to obtain sharper peaks in the photoelectron spectrum and a minimal solvation-energy shift. The photoelectron spectroscopy of doubly charged anions aggregated with several H_2 molecules has been investigated previously.[76] These spectra reveal a slight blue shift of the binding energy, having ~34 meV per H_2 on average. This binding energy is lower than the typical binding energy of an Ar atom (~60 meV).[46] In contrast, studies of $F^-(H_2)$ and $OH^-(H_2)$ that access the transition state region using negative ion photoelectron spectroscopy display a larger H_2 solvation energy of about 250 meV.[77-79] Our measurement is consistent with the larger shift in binding energy, as discussion in detail later.

One application of this technique that has been developed is messenger spectroscopy. First recorded using predissociation of H_2–solvated species as a function of photon energy, it has facilitated the measurement of infrared spectra of cationic clusters in a continuous beam.[80-82] Recently, vibrational predissociation spectroscopy of macromolecular ions, tagged with H_2 molecules, has been realized using a ESI source and a cryogenic ion trap.[38] By analysis of vibrational bands in the infrared action spectrum and electronic structure calculations, the structural characterization of these ions was obtained.

Figure 3.8 shows a comparison between two mass spectra for the production of CH_3O^- (m/z = 31). The CH_3O^- which is formed in the side discharge source (–800V, 140 μs) from expansion of Ar gas (2.0 atm) bubbling through liquid CH_3OH (99.8%, Macron^{TM} Chemicals) kept

at room temperature. The plasma is then entrained into a main expansion of either neat Ar (black) or a mixture of 25% H_2 in Ar (red) at a backing pressure of 3.7 atm. In the neat Ar expansion, CH_3O^-(Ar) is formed; we confirm this by photoelectron spectroscopy. When H_2 is added, using a gas mixture of 25% H_2 seeded in Ar, the intensities at m/z = 33, 35, and 37 increase, denoting the formation of $CH_3O^-(H_2)_{1\text{-}3}$ clusters. When optimizing for the cluster intensities, the intensity of m/z = 31 is about 20 times stronger than the m/z = 33 intensity.

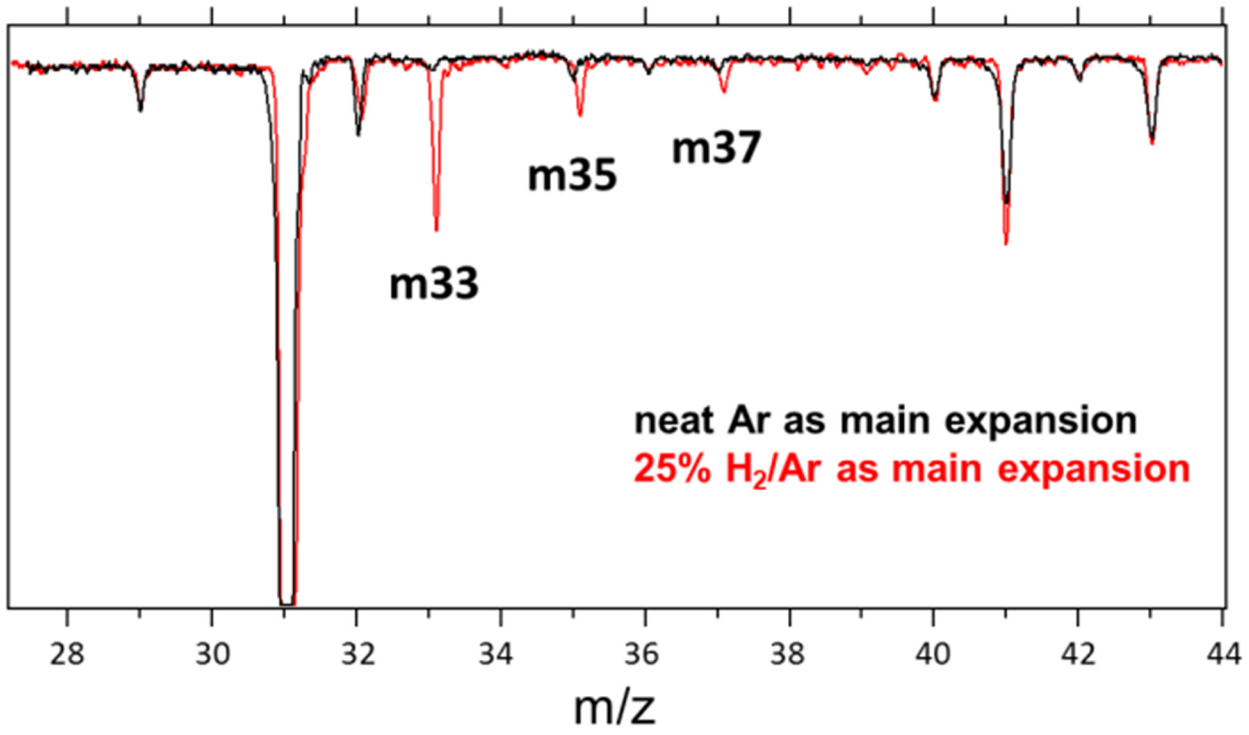

Figure 3.8 Comparison of the $CH_3O^-(H_2)_{n=0-3}$ TOF mass spectra from experiments using neat Ar (black) and 25% H_2/Ar (red) for the main expansion. The CH_3O^- is made in the side discharge source.

Figure 3.9 shows the 532-nm (2.330 eV) photoelectron spectra of CH_3O^- and $CH_3O^-(Ar)$, together with the 459-nm (2.703 eV) photoelectron spectra of CH_3O^- solvated with one, two, and three H_2 molecules. The photoelectron spectrum of CH_3O^- has been studied previously.[83-85] The photoelectron spectrum of CH_3O^- shows a Jahn-Teller vibronic transition that is assigned to e' degenerate vibrational modes of the ground state (^2E) methoxy radical. The SEVI spectrum of CH_3O^- has resolved the spin-orbit features.[85] Direct comparison of the photoelectron spectra for CH_3O^- and $CH_3O^-(Ar)$, top panel of Fig. 3.9, shows that the $CH_3O^-(Ar)$ spectrum (purple) exhibits a significant blue shift of about 95 meV from the CH_3O^- spectrum (black). Besides the shift, the vibrational progression in the photoelectron spectra are nearly identical, indicating a weak perturbation from the Ar solvent. The story is rather different when CH_3O^- is tagged with one hydrogen molecule. The photoelectron spectrum of $CH_3O^-(H_2)$ is significantly broadened, and the features are no longer resolvable. This is also shifted to a higher binding energy than the argon-tagged complex. If the solvation energy of the H_2 molecule was much small, creating only a little shift, it would be expected that by tagging $CH_3O^-(H_2)$ with more H_2 solvent molecules the internally energy of the anions and the spectral congestion would be reduced. However, the photoelectron spectra of $CH_3O^-(H_2)_2$ and $CH_3O^-(H_2)_3$ are still very broad. Unlike the CH_3O^- and $CH_3O^-(Ar)$ spectra, which provide information about the anion-neutral geometry change, the electron affinity, and vibrational frequencies, the H_2–tagged spectra presented herein provide very limited information.

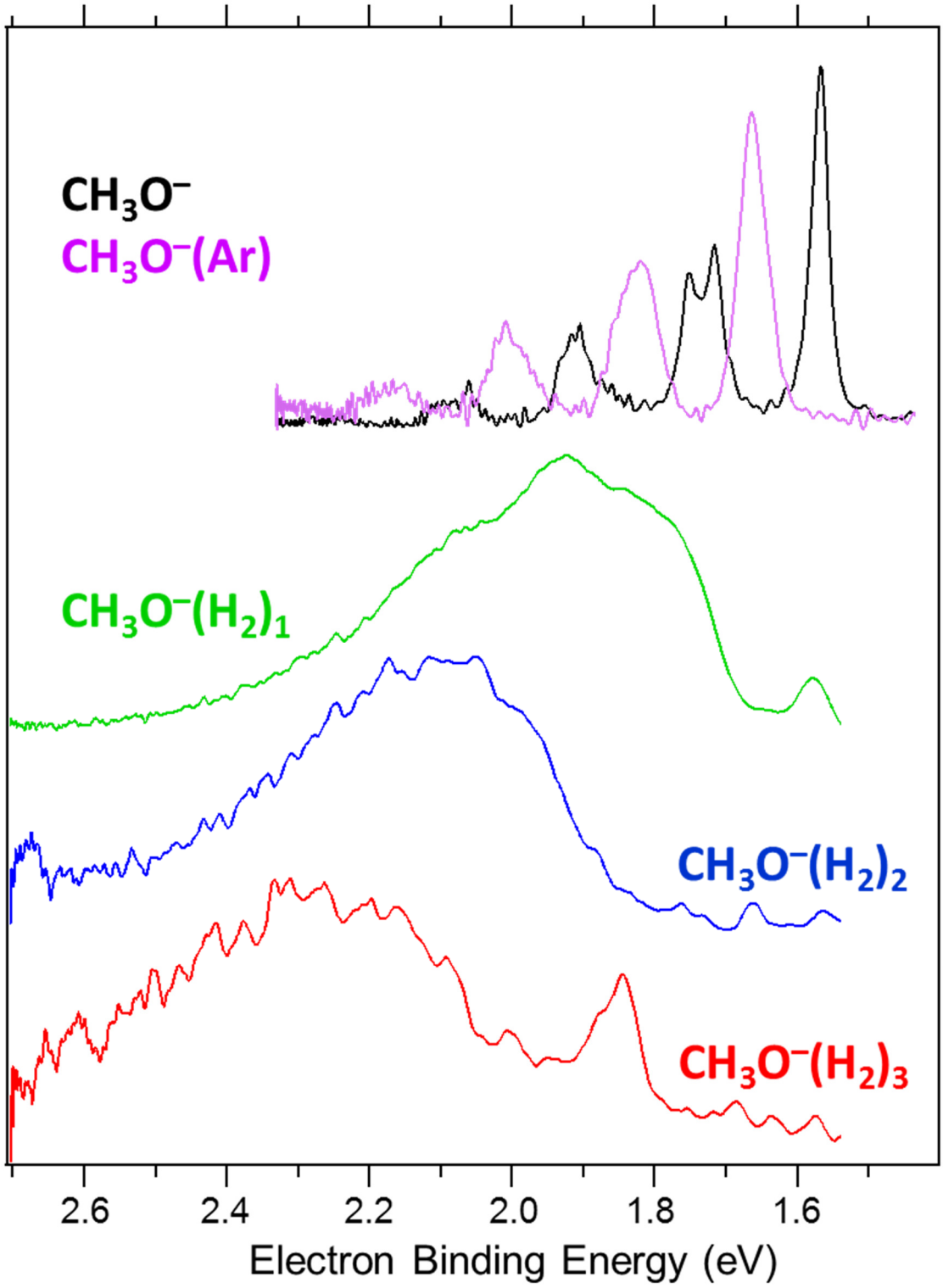

Figure 3.9 Photoelectron spectra of CH_3O^-, $CH_3O^-(Ar)$, and $CH_3O^-(H_2)_{n=1-3}$ using 532- and 459-nm light. The color-coded traces correspond to the indicated anion complexes.

In comparison to Ar solvation, H_2 tagging shows a greater solvation energy and only a broad feature. The blue-shifts of the electron binding energy as determined by the m/z = 71, 33, 35, and 37 spectra are ~ 95, 250, 450 and 590 meV, respectively, from the CH_3O origin. These findings contradict the idea of a small perturbation from H_2 solvation, as we had expected. If H_2 solvation leads to internally colder anionic clusters, why are the spectra of the $CH_3O^-(H_2)_{1\text{-}3}$ clusters more congested? There are several likely reasons. First, the stronger interaction in the anionic complexes gives rise to a shorter bond distance between the solute and the solvent than in the case of the neutral complexes. The broad spectral feature observed for the H_2–tagged species may result from accessing the steep repulsive wall of the neutral potential upon photodetachment. Second, partial H-bonding in the CH_3O^-·H–H form an intermediate that may complicate the anion photoelectron spectrum; photodetachment may access the transition state region of neutral surface, analogous to $F^-(H_2)$ and $OH^-(H_2)$. As a consequence, adding H_2 does not simplify the CH_3O^- spectrum. Additional efforts for high-resolution experiments and theoretical calculations need to be carried out to explain the peak broadening due to H_2 solvation.

3.3.5 $HOCO^-$

We demonstrated large, cold $OH^-(Ar)_n$ clusters in Section 3.3.3. With a cold OH^- source, a well-controlled chemical reaction can facilitate the formation of the anionic forms of OH reaction intermediates that are of interest in the atmosphere and in combustion. Here we take $HOCO^-$ as an example, and compare our results with data obtained from the work of Johnson *et al.* who stored $HOCO^-$ in a cryogenic electrostatic ion beam trap.[68] To make internally cold $HOCO^-$ in the present experiment, we perform a condensation reaction between a neutral CO molecule and an OH^- anion, after which the newly formed $HOCO^-$ cools in the supersonic expansion.

$$OH^- + CO + Ar \rightarrow \textit{trans}\text{- and } \textit{cis}\text{-}HOCO^- \text{ (internally excited)} + Ar \quad (3.1)$$

$$\textit{trans}\text{- and } \textit{cis}\text{-}HOCO^- \text{ (internally excited)} + nAr \rightarrow \textit{trans}\text{- and } \textit{cis}\text{-}HOCO^- \text{ (cooled)} \quad (3.2)$$

The neutral CO reactant is present in the main expansion (1% CO seeded in 3.7 atm of Ar), while the OH^- is formed in the side discharge. The position of the side valve is near the vicinity of the nozzle of the main pulsed valve, described in Section 3.2, so the OH^- is taken up very early in the main expansion. The anion and neutral find each other in the high density of the early expansion and the association reaction take place, forming the $HOCO^-$ product, and subsequent collisions of the anion with Ar result in an internally cold $HOCO^-$

Figure 3.10(a) presents photoelectron spectra of $HOCO^-$ taken at three different wavelengths: 532 (2.330 eV), 602 (2.059 eV), and 764 (1.622 eV) nm. Clearly, there is a strong cross-section suppression of photodetached electrons near threshold. This behavior is described by the threshold law (see Section 1.1.4).[17,86,18,87,88] (Note that simulating a near threshold spectrum can alter the Franck-Condon simulation and yield incorrect information about the anion-neutral geometry change; however, the spectral assignments in the spectrum should not be affected by the threshold law.) Previously, Johnson *et al.* adapted the cryogenic ion trap to the photoelectron-photofragment coincidence spectrometer for storing and cooling of $HOCO^-$ anions in a ~20 K environment.[68,59] They determine the adiabatic EAs of *cis*– and *trans*–HOCO to be 1.51 and 1.38 eV, respectively. Their near-threshold spectrum (775 nm) is reproduced as the blue trace in Fig. 3.10(b).[68] The black trace in Fig. 3.10(b) is an enlargement of our 764-nm spectrum seen in Fig. 3.10(a). Comparison between the black and blue traces in Fig. 3.10(b) finds that the peak positions in both spectra are consistent, illustrating the success of the stepwise $HOCO^-$ synthesis. This novel synthesis also produced the desired anion with low levels of internal excitation. Despite the

similarity in the peak positions, there are still two dissimilarities between the two spectra in Fig. 3.10(b): the peak width and the ratio of *cis*– and *trans*–$HOCO^-$ isomers. First, the narrower peak width in our data could arises from lower initial excitation of anion's internal degrees of freedom or from a higher instrument resolution. In either event, the narrower peaks reduce spectral congestion and provide information with a smaller uncertainty. For example, near an eBE of 1.52 eV, the black spectrum shows two distinct peaks, but these peaks are overlapped in the blue spectrum. Second, the black spectrum in Fig. 3.10(b) has a larger contribution from the *trans*–$HOCO^-$ isomer than the blue spectrum. The different proportions of the two isomers are due to the different way in which the anions are formed. In the sample used to obtain the blue spectrum, the $HOCO^-$ anions are stored in the ion trap for several hundred milliseconds and most of them are quenched to the global minimum, *cis*–$HOCO^-$. On the other hand, in the entrained pulsed jet, the two isomers are suddenly cooled to their individual minima and shortly thereafter are in a collisionless region, "trapping" more *trans* isomers. This comparison proves that without using a cryogenic ion trap, this low-expense, pulsed anion source has the capability to make cold anions, even when the anions form from exothermic association reactions.

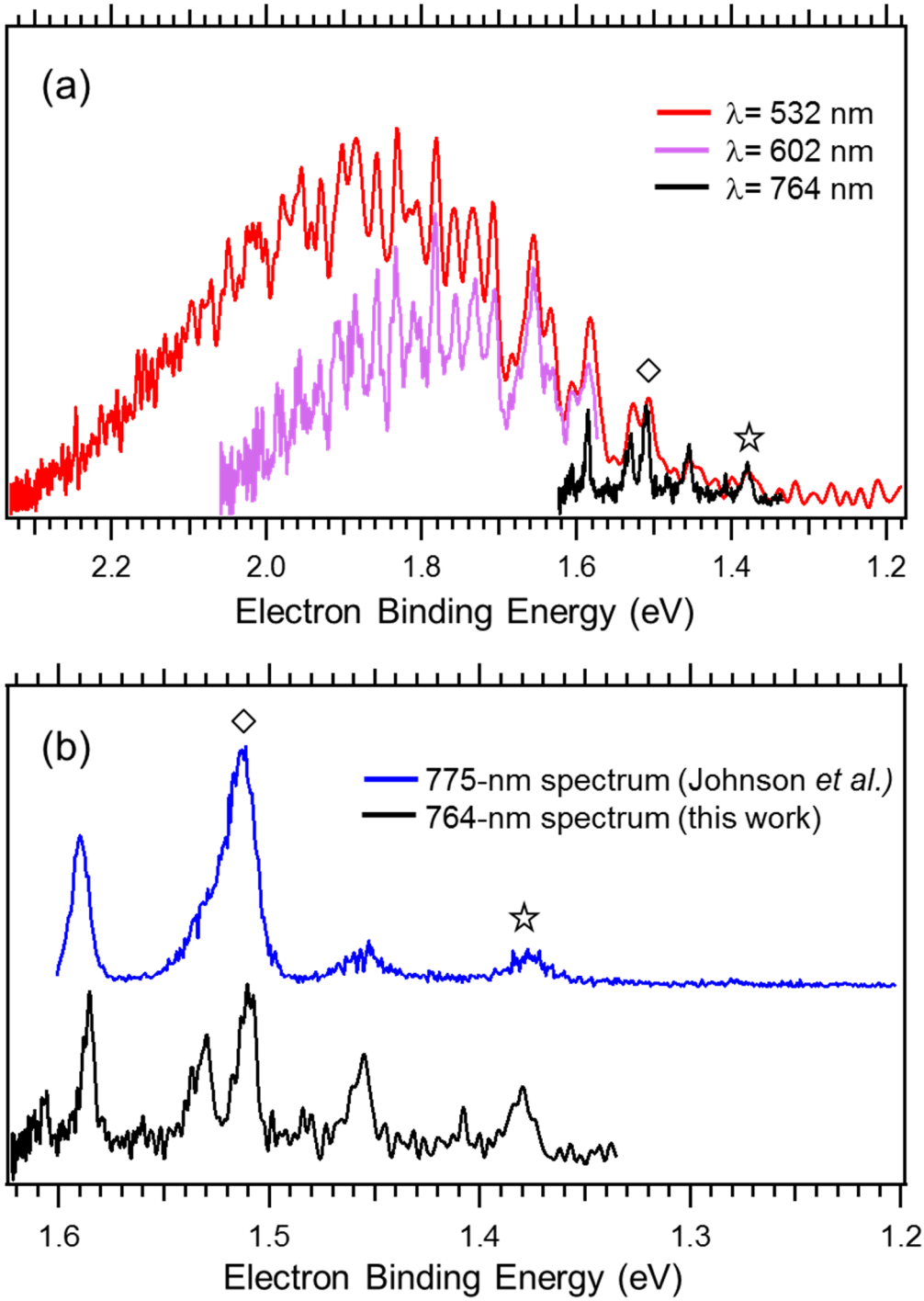

Figure 3.10 Photoelectron spectra of $HOCO^-$ (a) at three different wavelengths: 532 (red), 602 (purple) and 764 (black) nm, and (b) comparison between the 764 nm spectrum (this work) and the 775 nm spectrum (blue) from Johnson *et al*.[68] The diamond and star symbols denote the EA of *cis*– and *trans*–$HOCO^-$, respectively, from the assignments in the work of Johnson *et al*.[68]

3.3.6 CH_3OO^-

The CH_3OO^- anion has been investigated and formed using a proton abstraction reaction; this reaction was performed by adding CH_3OOH downstream of an OH^- in a flowing afterglow ion source at JILA.[69] We also generate CH_3OO^- using the pulsed anion source described in this chapter; here we carry out an association reaction between O_2 and CH_3^-.

$$CH_3^- + O_2 + Ar \rightarrow CH_3OO^- \text{ (internally excited)} + Ar \quad (3.3)$$

$$CH_3OO^- \text{ (internally excited)} + nAr \rightarrow CH_3OO^- \text{ (cooled)} \quad (3.4)$$

The CH_3^- reactant, produced in the side discharge pulse (-900V) from 2.4 atm of neat CH_4, is added in the vicinity of the nozzle of main pulsed valve from a perpendicular geometry. It is in the main expansion that the association reaction takes place. The main expansion is created from a gas mixture that is 1% O_2 seeded in Ar at a total backing pressure of 3.7 atm. The CH_3OO^- adduct is generated and efficiently cooled in the Ar supersonic jet. When optimizing for the CH_3OO^- anion, the intensity ratio of CH_3^- to CH_3OO^- is 3:1.

In order to confirm production of the CH_3OO^- adduct from the pulsed anion source, we take the photoelectron spectrum at 532 nm (2.330 eV) and compare it to the spectrum previously obtained in the flowing afterglow photoelectron spectrometer using 363.8-nm radiation; these two spectra are shown in Fig. 3.11. The CH_3OO^- spectrum provides the electron affinity, the term energy, and the CH_3O–O stretching and H_3C–O–O bending frequencies. The eBEs of the spectral features in both spectra are consistent, suggesting that both anions are the indeed the same species. Again, it indicates the capabilities of this novel pulsed anion source. Hence, without using any explosive compounds, this pulsed anion source performs rational ion synthesis to make transient species that are internally cold.

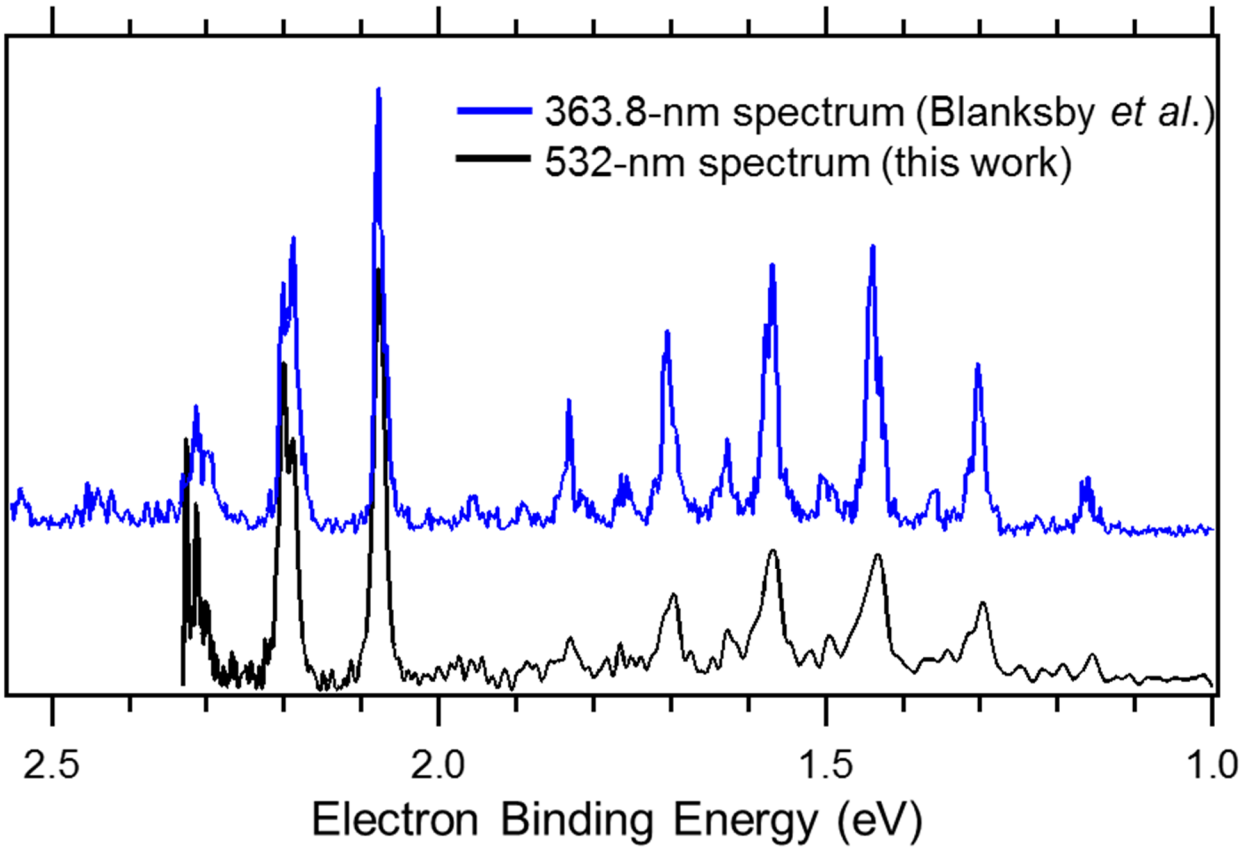

Figure 3.11 Comparison of the CH_3OO^- spectra obtained using the wavelengths of 363.8 (blue) and 532 (black) nm. For the blue spectrum from Blanksby *et al.*,[69] CH_3OO^- is formed *via* a proton abstraction reaction following addition of CH_3OOH downstream of OH^- in a flowing afterglow ion source at JILA. For the black spectrum (this work), we perform the association reaction of O_2 with CH_3^- in an Ar pulsed jet to generate CH_3OO^-.

3.4 Conclusion

In this chapter, we present a versatile, pulsed anion source that utilizes a plasma-entrainment method suitable for production of cold anions (that can easily be solvated). This simple and inexpensive setup is also capable of tagging anions with Ar atoms to ensure that the internal energy of the ions is low. Further, this ion source is able to produce cold anions through a well-controlled ion-molecule reaction, such as the production of $HOCO^-$ and CH_3OO^- *via* association reactions. All of these very exothermic reactions have been successfully performed by entraining the charged species into a main expansion containing ~1% of the neutral reactant. This versatile anion source allows for the investigation of many exotic or transient species. In addition to the applications addressed in this chapter, cooling anions and rational ion synthesis, there is also the possibility of initiating chemistry from size-selected clusters (bigger than binary complexes) to explore significant portions of reactive potential energy surfaces that are not accessed in the binary complexes.

Chapter 4
Photoelectron Spectroscopy of the Methyl Anion, CH_3^- and CD_3^-

4.1 Introduction

CH_3^- is the simplest carbanion and has a trivalent carbon atom with a lone pair of electrons and a negative charge.[89] Carbanions frequently occur as reactive intermediates in organometallic chemical reactions and are involved in the formation of Grignard and organolithium reagents. While in these organometallic reagents, the anions are not free, but instead are stabilized by counterions, experimental studies in the gas phase can provide a deeper understanding of the intrinsic properties of isolated carbanions. CH_3^- can be obtained by removing a proton from methane. Methane, however, is an extraordinarily weak acid and has an extremely high gas-phase acidity. Since the difficulty of removing a proton from methane reflects the difficulty of forming CH_3^-, the properties of this anion are not well known, despite its fundamental importance. If the simplest alkyl anion, CH_3^-, can be characterized, further insight may be gained about larger alkyl anions.

The inversion splitting between the 0^+ and 0^- levels of the umbrella-bend state corresponding XH_3 molecules has been explored in the NH_3 (ND_3)[90,91] and H_3O^+ (D_3O^+)[92-94] systems. Since the CH_3^- anion is isoelectronic with NH_3 and H_3O^+, it is expected that CH_3^- will also have a pyramidal structure with C_{3v} symmetry and a symmetric double-well potential, and, thus, an inversion splitting associated with the umbrella bending vibration. In NH_3, this tunneling motion has been well-studied due to its use in the first maser, and this splitting is 23.7 GHz (0.79 cm^{-1}). In H_3O^+, a lower inversion barrier leads to a larger splitting of 55.35 cm^{-1}. Until the present work, the inversion splitting of the CH_3^- anion has not been experimentally observed. In

addition, this work also utilizes study of the fully deuterated species, CD_3^-, to understand the mass dependence of the tunneling effect. Herein, we report an experimental determination of the inversion splitting of CH_3^- and CD_3^-.

The previous experimental studies of CH_3^- are scant and mostly focus on the electron affinity (EA) of CH_3 and the gas-phase acidity of CH_4.[95,96,72,97-99] The photoelectron spectrum of the CH_3^- anion has been studied previously.[72] Ellison *et al.* reported an early (55-meV resolution) determination of EA(CH_3), 0.08 ± 0.03 eV. The CH_3^- spectrum exhibited a long progression in the v_2 umbrella mode of ground-state CH_3, indicating transitions from a pyramidal anion to a planar $^2A''$ ground state of CH_3. The $^2E'$ valence excited state of the CH_3 radical was not observed, indicating that it lies more than 2.2 eV above the ground state. The low resolution of the energy analyzer prohibited any determination of the inversion splitting in the anion.

Graul and Squires employed collision-induced dissociation of various carboxylate or alkoxide anions to generate CH_3^- and investigated reactions of the anion with neutral molecules.[97] Using thermochemical cycles, they determined the gas-phase acidity of methane to be 417 ± 4 kcal/mol. This strong basic property of CH_3^- allowed for the observation of proton transfer even from ethylene and NH_3 to CH_3^-. Electron transfer from CH_3^- to O_2, OCS, CS_2, and C_6F_6 was also observed, indicating a low electron binding energy for CH_3. This low EA is consistent with both the results of Ellison *et al.*[72] and an autodetachment study of CH_3^- following IR excitation.[99] Finally, Graul and Squires observed both nucleophilic addition and elimination reactions of CH_3^- with both protic and aprotic reagents, showing its high nucleophilicity.

There has been considerable theoretical attention directed toward the CH_3^- anion.[100-115] The stability and structural properties are highly emphasized. Calculated structures are also consistent

with a pyramidal geometry. However, the EA has been calculated to be both positive and negative (bound and unbound, respectively), depending on the level of theory and basis set used. In particular, the anharmonicity of the umbrella mode adds difficulty and complexity to the calculation of the zero point energy, which strongly affects the calculated electron binding energy of this weakly bound anion. For reliable results, a potential energy surface calculation of high quality is required.

In this chapter, we report the photoelectron spectra of cooled CH_3^- and CD_3^-. We utilize the plasma-entrainment anion source described in Chapter 2 to produce reasonable quantities of cold CH_3^-, allowing us to investigate its properties with much higher resolution than was previously possible. Using CD_4 as a precursor, CD_3^- can also be formed and studied. We measure the electron affinities of CH_3 and CD_3, and we significantly improve the measurement uncertainty using mid-IR light. We observe extended vibrational progressions involving the umbrella bend in the electronic ground state of both CH_3 and CD_3. The observation of the well-studied ν_2 bands of CH_3 and CD_3, coupled with the dramatically improved electron energy resolution, enable us to directly measure the inversion splitting between the 0^+ and 0^- energy levels in both CH_3^- and CD_3^-. In addition, by employing a thermochemical cycle, we can improve upon the previous measurements of the gas-phase acidity of methane and report the experimental gas-phase acidity for d_4-methane. Finally, we compare our experimental results with calculated values and discuss possibilities for investigating yet-to-be-detected CH_3 $^2E'$ valence excited state.

4.2 Experimental Details

In this experiment, we utilize the negative ion photoelectron velocity-map imaging (VMI) spectrometer, described in more detail in Chapter 2, to obtain anion photoelectron spectra. This experimental apparatus uses a pulsed anion beam that is mass-separated by a Wiley-McLaren time-of-flight mass spectrometer (TOF MS). The mass-selected anions of interest are photodetached using a tunable light source, and then a standard VMI photoelectron detector is utilized to obtain the photoelectron spectrum.

The CH_3^- anion is prepared in a novel plasma-entrainment pulsed anion source described in Chapter 2. This source utilizes two pulsed General Valves (Parker-Hannifin, series 9): one serves to create the supersonic expansion, the other is placed perpendicular to this main expansion and utilizes an electric discharge. The electrical discharge takes place when the gas passes through a stainless steel cathode, which is pulsed (140 μs) at a potential of -900 V in series with two 10kΩ resistors (for increased discharge stability), to a stainless steel grounded anode. This side discharge nozzle, which operates under choked-flow conditions (2.4-atm neat CH_4), is pulsed for approximately 250 μs, introducing ions into an Ar expansion (backing pressure, 3.7 atm). The Ar beam picks up the anions moving them in the direction of the main expansion and providing additional collisional cooling. The cold anions are then extracted into the TOF MS. Figure 4.1(a) shows the mass spectrum under these conditions. We confirm the chemical identity of the mass-selected anions by comparing their photoelectron spectra with other known anion photoelectron spectra. Using neat CD_4 as a precursor, CD_3^- can be generated in an analogous manner, and the mass spectrum is shown in Fig. 4.1(b).

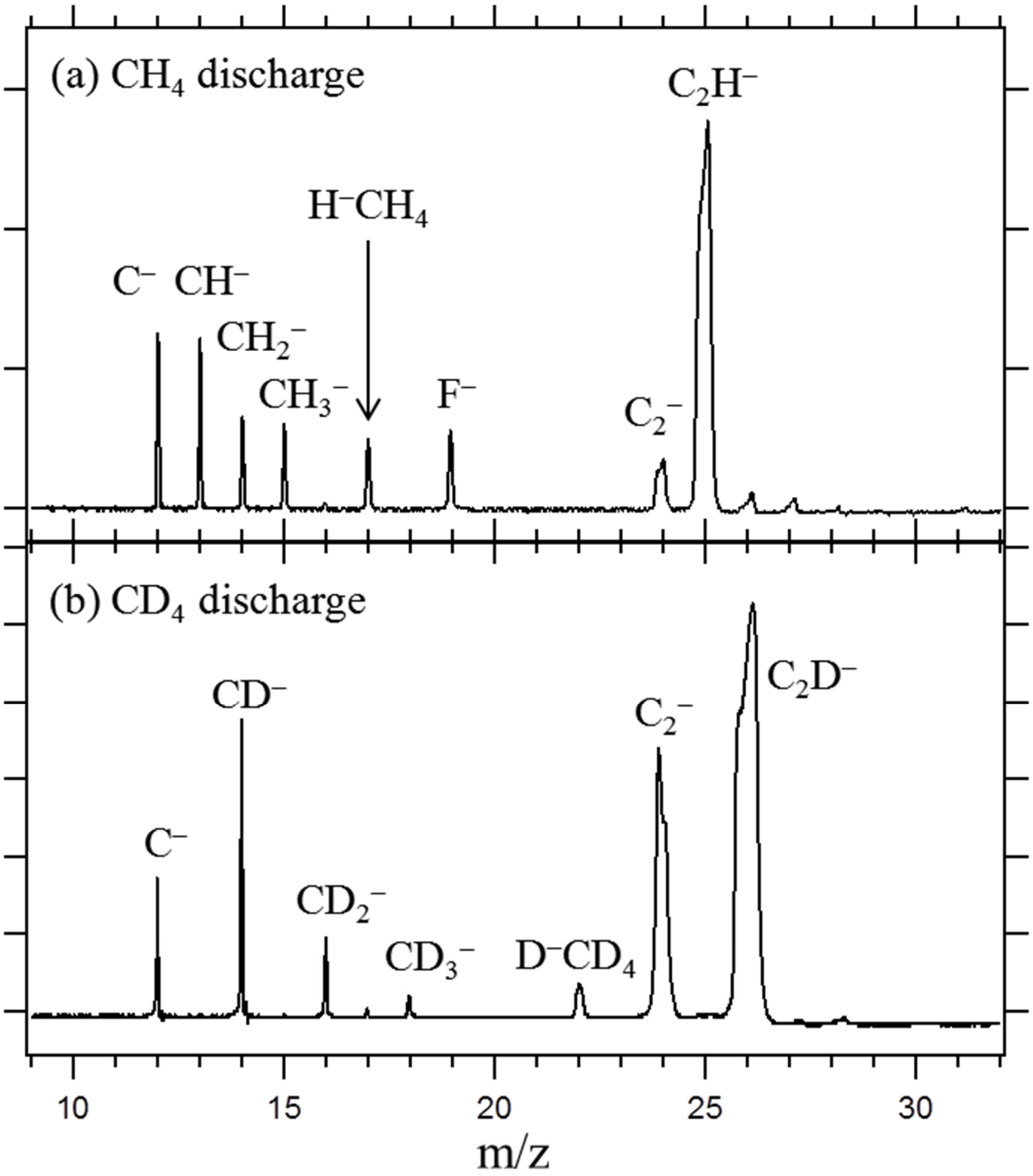

Figure 4.1 Mass spectrum for the production of CH_3^- and CD_3^- by introducing ions formed from (a) a neat methane or (b) a neat methane-d_4 pulsed discharge, respectively, into a neat Ar expansion. F^- comes from chemical contamination in sample line.

Anions of m/z = 15 or 18 are photodetached by spatially and temporally overlapping them with laser light. The velocity and angular distribution of the photodetached electrons is then acquired by the VMI photoelectron spectrometer. The raw data are converted into a velocity distribution using the BASEX implementations in the required Abel inversion.[49] The spectral resolution in the VMI spectrometer improves as the electron kinetic energy (eKE) decreases. Since we have access to a tunable light source, we use three different photon energies to obtain photoelectron spectra of CH_3^- and CD_3^-. The 763-nm (1.625-eV) output of a 532-nm pumped dye laser is used to obtain a survey photoelectron spectrum, and the Nd:YAG fundamental light (1064 nm or 1.165 eV) is used to obtain the overview (full eKE range) photoelectron spectrum of the CH_3 ground state. A higher energy-resolution spectrum, focusing on the lowest energy transitions, is obtained using 3236-nm (0.383-eV) light. We generate this mid-IR light using difference frequency generation (DFG) of 801-nm (1.548-eV) light (from the 532-nm pumped LDS798 dye laser) and the residual 1064-nm (1.165-eV) light (Nd:YAG fundamental) in a 1x1x3 cm^3 magnesium oxide doped lithium niobate ($MgO:LiNbO_3$) crystal. The mid-IR light, which generally has energies of 50–100 μJ/pulse, is focused into the laser-anion interaction region using a 1-m CaF_2 lens. To determine the exact photon energy, we directly measure the dye wavelength using a wavemeter (Atos, LRL-005) calibrated by a He-Ne laser, and then calculate the resultant mid-IR wavelength.

In this thesis, we report photoelectron spectra as a function of electron binding energy (eBE= $\hbar\omega$ – eKE), which is independent of the laser wavelength. The calibration of the energy scale for the reported data is performed using the well-measured ν_2 out-of-plane bending frequencies in neutral CH_3 and CD_3 from high-resolution IR absorption studies.[116-118] In order to

confirm the validity of this procedure, we also calibrate the energy scale for the images using the known photoelectron spectrum of S^- with 532-nm light to assure agreement.[50-52]

Since the band origin and the observed peak maximum are not necessarily the same, the uncertainty in the determined eBE is given by combining the uncertainty in the Gaussian-fit peak-center location with the deviation of the peak center from the simulated and fitted band origin. We reproduce and fit the rotational envelope of the observed peaks in the photoelectron spectra using the PGOPHER rotational simulation program.[119] The anions and neutrals are treated as rigid symmetric tops, and the rotational constants for the anions and neutrals are obtained from Kraemer *et al.*,[110] Yamada *et al.*,[116] and Sears *et al.*.[118] The rotational temperature and Gaussian linewidths of the rotational transitions are varied until the rotational band contour best fits the observed lineshapes. Consequently, each difference between the peak maximum and the simulated band origin can be accurately obtained.

4.3 Results

Upon photodetachment, the out-of-plane bending angle from the pyramidal CH_3^- anion to the planar CH_3 radical changes significantly, which leads to an extended Franck-Condon progression in the umbrella v_2 mode. Figure 4.2 shows schematic potential energy curves as a function of the out-of-plane bending angle for both CH_3^- and CH_3. The curves are plotted using the parameters found in from Kraemer *et al.*[110] and shifted to fit our experimental findings. The out-of-plane bending angle is defined as the angle between the C–H bond and the plane of the three H atoms. For example, a 0 degree angle is formed by the C atom in the H_3 plane, which corresponds to the equilibrium geometry of the methyl radical. The plotted wavefunctions are obtained using the Numerov method.[120] As shown in Fig. 4.2, the pyramidal CH_3^- anion exhibits

a symmetric double-well potential, which gives rise to an inversion splitting, analogous to NH_3 and H_3O^+. The inversion splitting depicted in Fig. 4.2 arises from the wavefunction tunneling through the barrier. The coupling of the two equivalent vibrational states for the two configurations of CH_3^- lifts the degeneracy, splitting the energy levels, and creates two discrete parity states. These ground-state inversion levels of CH_3^-, denoted here as 0^+ and 0^-, are linear combinations of the degenerate states with even and odd symmetries, respectively. Excitation will follow the selection rule $v_2'' = 0^+ \rightarrow v_2' = 0, 2, 4\ldots$ and $v_2'' = 0^- \rightarrow v_2' = 1, 3, 5\ldots$ to preserve the parity and ensure a non-zero Franck-Condon overlap. If both 0^+ and 0^- states of CH_3^- are populated in the anion beam, we anticipate the progression in the non-totally symmetric v_2 mode to be irregularly spaced. In other words, the above-stated selection rule requires alternate vibrational levels of the methyl radical to be populated by excitation from either the 0^+ or 0^- inversion level of the anion. These Franck-Condon allowed transitions are indicated by the red ($v_2'' = 0^+$) and blue ($v_2'' = 0^-$) double arrows in Fig. 4.2.

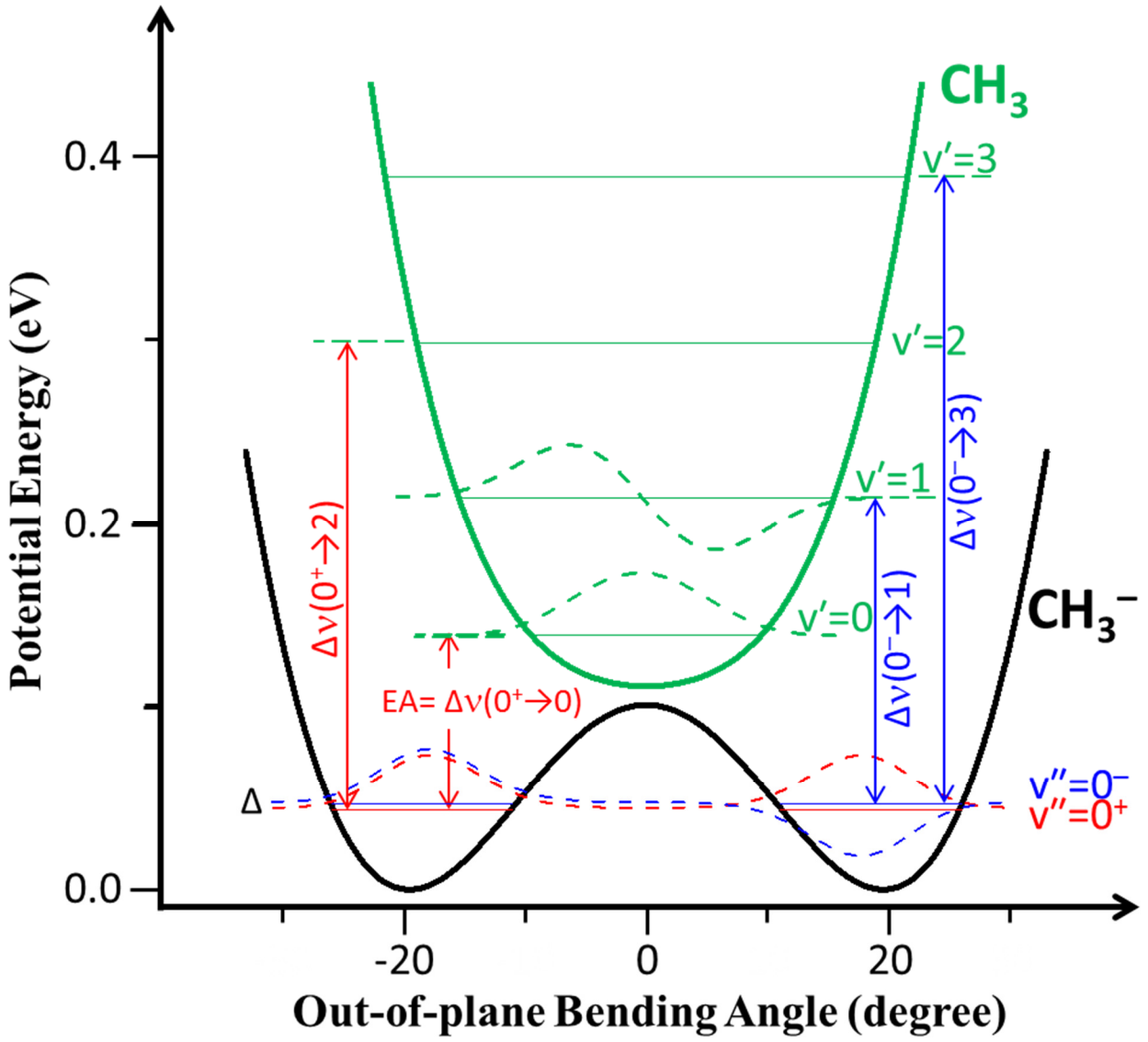

Figure 4.2 Schematic potential energy surfaces for the electronic ground states of CH_3 (green) and CH_3^- (black) as a function of the out-of-plane bending angle. The red and blue arrows indicate a non-zero Franck-Condon overlap for $v''=0^+$ (even wavefunction, red dashed line) and 0^- (odd wavefunction, blue dashed line) in the anionic ground state to even and odd quanta of the neutral state, respectively. The 0^+–0^- inversion splitting of the CH_3^- is labeled Δ.

The three well-resolved photoelectron spectra of CH_3^-, shown in Fig. 4.3, agree with our expectations. These spectra, taken with 763 (1.625 eV, black), 1064 (1.165 eV, red), and 3236 (0.383 eV, blue) nm photodetachment wavelengths, show similar features to the Ellison *et al.* photoelectron spectrum, exhibiting an extensive progression of energy levels in the out-of-plane bending mode of CH_3. The observed peaks (labeled A through G) in Fig. 4.3 are listed and assigned in Table 4.1. The peak center, in eBE, of each transition is the weighted average of the three experimental spectra. Their uncertainties are given by the deviation of the center of the peak from the simulated and fitted band origin. As expected, the differences between adjacent peak positions are irregularly spaced, suggesting transitions from both anion inversion levels.

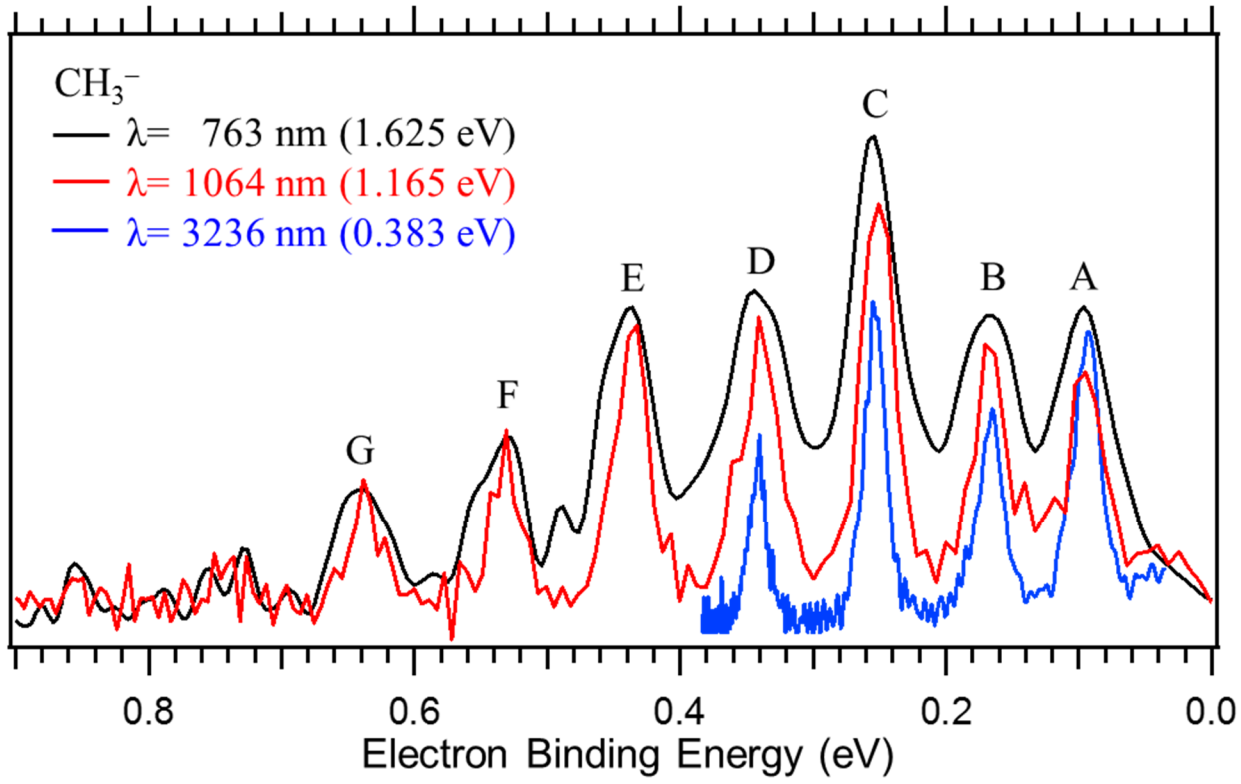

Figure 4.3 Photoelectron spectra of CH_3^- at three different photodetachment wavelengths: 763 (black), 1064 (red), and 3236 (blue) nm.

Table 4.1. Experimental peak positions and assignments in the photoelectron spectra of CH_3^- and CD_3^-. The values in parentheses are the uncertainties described in the text.

$CH_3 + e^- \leftarrow CH_3^-$			$CD_3 + e^- \leftarrow CD_3^-$		
Peak[a]	Position (cm^{-1})	Assignment $v_2' \leftarrow v_2''$	Peak[a]	Position (cm^{-1})	Assignment $v_2' \leftarrow v_2''$
A	763(31)	$0 \leftarrow 0^+$	a′	332(52)	
B	1349(27)	$1 \leftarrow 0^-$	a	691(28)	$0 \leftarrow 0^+$
C	2047(22)	$2 \leftarrow 0^+$	b	1138(22)	$1 \leftarrow 0^-$
D	2761(17)	$3 \leftarrow 0^-$	c	1650(19)	$2 \leftarrow 0^+$
E	3544(45)	$4 \leftarrow 0^+$	d	2190(17)	$3 \leftarrow 0^-$
F	4308(40)	$5 \leftarrow 0^-$	e	2767(14)	$4 \leftarrow 0^+$
G	5165(35)	$6 \leftarrow 0^+$			

[a] Peak labels shown in Fig. 4.3 and 4.4.

Since the spectral resolution in the VMI spectrometer degrades with increasing eKE, we use the spectrum obtained using 3236-nm light to obtain the highest accuracy measurement of the EA and inversion splitting. The near-threshold spectrum of CH_3^- is expanded in Fig. 4.4(a). We assign peak A, which is at the lowest eBE, to the transition from the lower inversion level, 0^+, of CH_3^- to the ground vibrational state of CH_3. This origin transition corresponds to the adiabatic electron affinity (EA) of the methyl radical. The most intense transition, peak C, which is assigned to the vertical transition from the 0^+ state of the anion to the $v_2' = 2$ state of the neutral, has the best Franck-Condon overlap and, thus, the smallest geometry change from the anion to the neutral. Transitions to odd v_2' quanta of the neutral have to come from the upper inversion level, 0^-, of CH_3^- in order to have a non-vanishing Franck-Condon overlap. The variation in peak intensity of the four peaks seen in Fig. 4.4(a) primarily reflects the relative populations of the 0^+ and 0^- inversion levels in the ion beam, further reinforcing our assignments. The peak intensities are also subject to the threshold effect, and, thus, the intensities of peak C and D in the near-threshold spectrum drop notably compared to other spectra taken with higher photon energies; see Fig. 4.3.

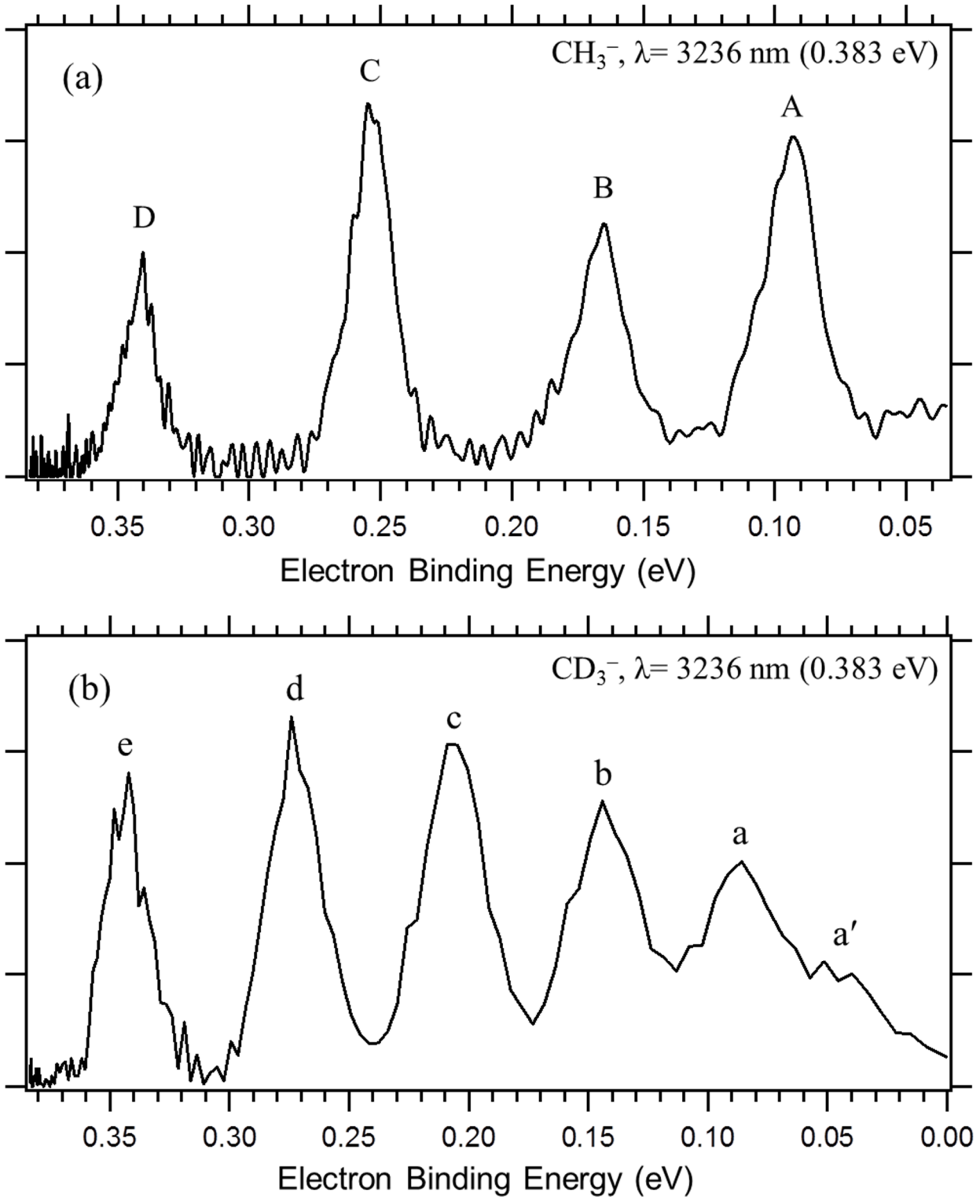

Figure 4.4 Mid-IR photoelectron spectra of (a) CH_3^- and (b) CD_3^-. The CD_3^- spectrum is rebinned to 2.5 pixels to improve the signal-to-noise ratio without changing the spectral appearance.

Figure 4.4(b) shows the near-threshold CD_3^- spectrum taken with 3236-nm laser radiation. The spectrum is rebinned to 2.5 pixels to improve the signal-to-noise ratio without altering the spectrum. The observed peaks (labeled a′, and a through e) in Fig. 4.4(b) are listed and assigned in Table 4.1. The uncertainties are obtained with the same method described above. Although peak a′ has the lowest eBE in the spectrum, the eBE of peak a′ is less than half of the eBE of peak A (the EA of CH_3). Because there is only a small change in the zero-point energy upon deuteration, it seems very unlikely that this low eBE denotes the EA of CD_3. Instead, we assign peak a to the origin transition. With an expected difference between the CH_3 and CD_3 EA of less than 10 meV (ca. 81 cm^{-1}), the 9 meV difference between Peaks A and a suggest that this assignment is preferred.[121] Based on this assignment, peak a′ is a hot band that likely arises from initial population in one or both of the 1^+, 1^- states of CD_3^-. As in CH_3^-, the peaks are irregularly spaced, indicating transitions from the 0^+ and 0^- states of the anion to even and odd quanta of vibrational levels of the neutral, respectively.

4.4 Discussion

Photoelectron spectroscopy of negative ions yields information on the structure and vibrational frequency of the corresponding neutral species. However, the fundamental ν_2 frequency, its overtones, and the planar equilibrium structure of CH_3 and CD_3 have all been rigorously determined from absorption and emission studies of the neutral species.[116,122,117,118] The experimental frequencies are summarized in Table 4.2; from this table it becomes apparent that the ν_2 frequencies of CH_3 and CD_3 show substantial negative anharmonicity (i.e., greater vibrational frequencies with increasing vibrational levels). Yamada *et al.* suggest that the negative anharmonicity may be attributed to a vibronic interaction between the ground and excited

electronic states of the neutral molecule.[116] In the present experiment, we take advantage of the known ν_2 frequencies of CH_3 and CD_3 umbrella modes to obtain the inversion splitting, $\Delta E_{Inv.}$, in CH_3^- and CD_3^-. For the $\Delta E_{Inv.}$ of CH_3^-, we use the equation shown below:

$$\Delta E_{Inv.}(CH_3^-, 0^+ \leftrightarrow 0^-) = 3\nu_2(CH_3, \nu_2=3\text{-}0) + \text{Peak A}(0 \leftarrow 0^+) - \text{Peak D}(3 \leftarrow 0^-).$$

This equation includes Yamada *et al.*'s measurement of $3\nu_2$ (2019.1657 cm^{-1}, CH_3, $\nu_2=3 \leftarrow 0$).[116] For the eBE of Peaks A and D, multiple measurements are obtained using mid-IR light. We then take an average of the computed values over several independent measurements to determine the inversion splitting, and assign an uncertainty that is one standard deviation of the mean. This procedure yields an inversion splitting of 24(2) cm^{-1} between the $\nu_2 = 0^+$ and 0^- energy levels of CH_3^-. Similarly, we apply the same approach to CD_3^-, giving a $0^+ – 0^-$ inversion splitting of 7(2) cm^{-1}. For comparison, we correct the measured ν_2 frequencies for the inversion splitting of the anion; these values are listed in Table 4.2. In addition, we use the eBE of Peak D (which has a lower uncertainty than Peak A) to improve our initial determination of the electron affinity of CH_3. By using the position of Peak D and the frequency of $3\nu_2$, we determine the EA to be 0.095(2) eV, which is consistent with the previously reported EA of 0.08(3) eV. Likewise, the electron affinity of CD_3 is determined to be 0.086(2) eV using the eBE of Peak e. Table 4.3 summarizes our experimental determinations of the EAs and inversion splittings.

Table 4.2. Experimentally measured out-of-plane bending frequencies of CH_3 and CD_3 (cm^{-1}) in the gas phase.

	CH_3			CD_3	
ν_2 band	Yamada *et al.*[a]	Hermann *et al.*[b]	This work[c]	Sears *et al.*[d]	This work[c]
$1 \leftarrow 0$	606.4531		610(41)	457.8136	454(36)
$2 \leftarrow 1$	681.6369		674(35)	507.9297	505(29)
$3 \leftarrow 2$	731.0757	729(4)	738(28)	542.2841	547(26)
$4 \leftarrow 3$		772(4)	759(48)	568.6322	570(22)
$5 \leftarrow 4$		811(4)	788(60)		
$6 \leftarrow 5$			833(53)		

[a] Reference 116.
[b] Reference 122.
[c] Values corrected using the inversion splittings.
[d] Reference 118.

Table 4.3. Experimentally determined values: adiabatic electron affinity (EA) and inversion splitting ($\Delta E_{Inv.}$).

$EA(CH_3)$	0.095(2) eV
$\Delta E_{Inv.}$ (CH_3^-, $0^+ \leftrightarrow 0^-$)	24(2) cm^{-1}
$EA(CD_3)$	0.086(2) eV
$\Delta E_{Inv.}$ (CD_3^-, $0^+ \leftrightarrow 0^-$)	7(2) cm^{-1}

Our experimentally determined EAs and inversion splittings, are in good agreement with the calculated values. Kraemer *et al.* investigated the CH_3^- and CD_3^- inversion potentials at the SCF/SRCI and CASSCF/MRCI levels of theory,[110] and calculated the electron affinities of CH_3 and CD_3 to be 0.09 and 0.08 eV, respectively. The inversion splitting was also calculated to be 19 cm^{-1} for CH_3^- and 4 cm^{-1} for CD_3^-. In addition, Dixon *et al.* calculated the CH_3^- ground-state inversion splitting of 27 cm^{-1} and the CH_3 EA of 0.071±0.013 eV using the CCSD(T) level of theory.[103,113]

Depuy *et al.* have used the gas-phase acidity, or the deprotonation enthalpy ($\Delta_{acid}H$), of methane as a reference in determining alkanes acidities.[123] For this molecule to serve as a reliable reference acid, its gas-phase acidity should be known as accurately as possible. From our precise measurement of the EA(CH_3), we are able to refine the gas-phase acidity of methane at 0 K using a thermochemical cycle involving the $H_3C–H$ bond strength, the ionization energy of H, and the electron affinity of CH_3: $\Delta_{acid}H_0(CH_4) = D_0(H_3C–H) + IE(H) – EA(CH_3)$. The bond dissociation energy of methane, $D_0(H_3C–H)$, was reported by Ruscic *et al.* to be 103.42(3) kcal/mol.[124] The ionization energy of hydrogen, IE(H) = 313.59 kcal/mol, is well known. In this work, our measured value for the EA(CH_3) of 0.095(2) eV (2.19±0.05 kcal/mol) yields the revised $\Delta_{acid}H_0(CH_4)$ = 414.82(6) kcal/mol. The uncertainty of the resulting gas-phase acidity is one order of magnitude smaller than the previous measurement. Moreover, the present measurement for the EA(CD_3) of 0.086(2) eV (1.98±0.05 kcal/mol), together with the $D_0(D_3C–D)$ = 105.80(3) kcal/mol[125] and the well-known IE(D) = 313.69 kcal/mol, gives the first determination of the gas-phase acidity of d_4-methane, $\Delta_{acid}H_0(CD_4)$ = 417.51(6) kcal/mol.

Negative ion photoelectron spectroscopy can also be used to investigate the electronic energy levels, or term energies, of neutrals. The methyl radical has a $^2A_2''$ ground state and a

valence excited state, $^2E'$, that has been predicted theoretically but not observed experimentally. The $^2E' \leftarrow ^2A_2''$ transition is symmetry forbidden in the neutral molecule; however, the $^2E'$ state is accessible by photodetachment of the CH_3^- anion. Various electronic structure calculations show the vertical excitation energy of the $^2E'$ level, ranging from 6.8 to 7.6 eV, for the planar equilibrium geometry of the CH_3 ground state.[126-132] In particular, the MRCI[131] and EOM-CCSD[132] results are 7.13 and 7.01 eV, respectively. Using the valence state equilibrium geometry to optimize the CH_3 ground state, the excitation energy of the valence state was calculated to be 4.5 or 4.2 eV.[129,131] Therefore, the adiabatic excitation energy is believed to be between 4.2 and 7.6 eV. The 1978 photoelectron spectrum of Ellison *et al.* confirms that the $^2E'$ level is more than 2.2 eV above the CH_3 ground state, and, with our tunable light source, it is tempting to pursue a photoelectron spectrum of CH_3^- that would expose the $^2E'$ state. Unfortunately, the UV light required to access the $^2E'$ state of the CH_3 radical from the CH_3^- anion creates severe background photoelectrons in our current apparatus, giving an extremely bad signal-to-noise ratio. This experiment may be feasible in an oil free chamber where UV-induced background photoelectrons would be minimal.

4.5 Conclusion

We report the photoelectron spectra of CH_3^- and CD_3^-. These spectra show extensive progressions in the out-of-plane bending vibration of the electronic ground states of the neutral CH_3 and CD_3 radicals; this long Franck-Condon progression arises from a substantial change in the geometry upon photodetachment. The electron affinities of CH_3 and CD_3 are measured to be 0.095±0.002 and 0.086±0.002 eV, respectively. Using the well-studied ν_2 bands of CH_3 and CD_3, we determine the inversion splitting of the $CH_3^-$and CD_3^- anions to be 24±2 cm^{-1} and 7±2 cm^{-1}, respectively. By use of a thermochemical cycle, a precise gas-phase acidity is determined for CH_4

and CD_4 at 0 K: 414.82(6) and 417.51(6) kcal/mol, respectively. While the $^2E'$ valence excited state of CH_3 is accessible by removing an electron from CH_3^-, we were unable to determine the adiabatic excitation energy due a large background – spectroscopic examination of this state awaits a clean photodetachment experiment using approximately 6-eV photons.

Chapter 5
Photoelectron Spectroscopy of Propadienylidene Anion, H_2CCC^-

5.1 Introduction

Isomers of C_3H_2 are important in organic, astrophysical, and combustion chemistry. Singlet cyclopropenylidene (*c*-C_3H_2) is the global minimum structure (defied as E = 0 kcal/mol), which has two low-lying isomers are triplet propargylene (also called propynylidene, HCCCH, ΔE = 10 kcal/mol) and singlet propadienylidene ($H_2C=C=C$: or abbreviated to H_2CCC, ΔE = 13 kcal/mol).[133] The first experiment on H_2CCC was performed using IR spectroscopy in a matrix, and they confirmed the structure of H_2CCC using the comparison between the experimental and calculated IR spectrum.[134] Then additional laboratory characterization of this species was accomplished with microwave spectroscopy in the gas phase, where they determined the rotational and centrifugal distortion constants of H_2CCC.[135] Subsequently, H_2CCC was detected by radio astronomy in two dense clouds by identifying four rotational lines.[136] A combination of microwave studies and theoretical calculations determined the equilibrium geometry of H_2CCC to be a near-prolate top in a C_{2v} symmetry.[137-139] The electronic absorption spectrum of H_2CCC in Ar and Ne matrices was also measured and resulted in identifying the three lowest-lying singlet excited states and vibrational structures in each state.[140,141] Recently, using cavity ring-down spectroscopy, Maier *et al.* measured the electronic spectrum of H_2CCC at 4881 Å and 5450 Å belonging to $\tilde{B}\ ^1B_1 \leftarrow \tilde{X}\ ^1A_1$ transition in the gas phase, coincident with two unidentified diffuse interstellar bands (DIBs).[142] They proposed that the broad DIBs at these two wavelengths are produced by a ground-state electronic transition of H_2CCC. However, this assignment has been disputed and criticized.[143-145] More discussion can be found in the discussion section.

The photoelectron spectrum of H_2CCC^- anion has been previously measured by Oakes *et al.*[146] and Robinson *et al.*[121] using 488-nm and 351-nm lights, respectively. In the 488-nm spectrum, the electron affinity (EA) of H_2CCC has been measured to be 1.794(25) eV, but Oakes *et al.* did not observe any excited electronic states. Using 351-nm light, Robinson *et al.* observed the ground electronic state ($\tilde{X}\ ^1A_1$) and the first excited electronic state ($\tilde{a}\ ^3B_1$) of H_2CCC with photoelectron spectroscopy. They reported a more precise EA measurement of 1.794(8) eV and the singlet–triplet splitting of 29.7(2) kcal/mol. In comparison to conventional absorption spectroscopy, both singlet and triplet (spin-forbidden from neutral H_2CCC) electronic excited states can be investigated using negative-ion photoelectron spectroscopy.

In this chapter, we report the photoelectron spectrum of H_2CCC^- anion using radiation between 245 and 330 nm. We utilize a neutral–entrainment anion source to produce H_2CCC^-, allowing us to investigate its electronic excited states ($\tilde{b}\ ^3A_2$, $\tilde{A}\ ^1A_2$, $\tilde{B}\ ^1B_1$ and $\tilde{c}\ ^3A_1$). Vibrational transitions in the electronic states are also observed and assigned, allowing us to determine the term energies of H_2CCC. Finally, we compare our experimental results with calculated values and the experimental data previously collected.

5.2 Experimental Details

The VMI apparatus has been described in detail in Chapter 2. In general, the apparatus consists of a pulsed anion source, a Wiley-McLaren time-of-flight mass spectrometer (TOF MS),[24] a velocity-map imaging (VMI)[25,26] photoelectron spectrometer, and a ns-pulsed, tunable-laser system. Only experimental details that are specifically relevant to obtaining the H_2CCC spectrum will be discussed further.

Propadienylidene anion (H_2CCC^-) is formed *via* H_2^+ abstraction from allene by O^-[146,121,147] in a pulsed supersonic entrainment reactor.[46] The entrainment reactor comprises a central and two side pulsed solenoid valves (General Valve Series 9, 0.8-mm orifice) operating at 80 Hz with individual timings and pulse widths. The middle pulsed valve provides the main expansion using 1% allene (H_2CCCH_2; 97%, Sigma-Aldrich or 96%, Pfaltz & Bauer) seeded in Ar at a backing pressure of 4.4 atm. One of the adjacent pulsed valves entrains neat N_2O (99%, Scott Specialty Gases) at a backing pressure of 1.1 atm into the allene/Ar gas expansion. A guided, collinear beam of 1-keV electrons, emitted from a continuous electron gun with thoriated tungsten filament, collides with the gas expansion to produce slow secondary electrons. The interaction of slow secondary electrons with N_2O yields the O^- reactant by dissociative electron attachment. The O^- anion subsequently reacts with allene to produce H_2CCC^- anion. If the N_2O entrainment valve is turned off, the H_2CCC^- anion signal disappears.

The anions are perpendicularly extracted and mass-separated via the Wiley-McLaren TOF MS. The H_2CCC^- anions are photodetached by temporally overlapping the ion beam with a linearly polarized laser pulse tunable from 245 to 330 nm. The tunable light is produced by frequency doubling the signal output of a 355-nm pumped OPO in a BBO crystal. Following photodetachment of the H_2CCC^- anions, the VMI photoelectron spectrometer acquires the kinetic energy distribution of the photodetached electrons. In this chapter, we report the photoelectron spectra as a function of electron binding energy ($eBE = \hbar\omega - eKE$), which is independent of the laser wavelength used for photodetachment. The calibration of the energy scale for the reported data is performed using the known transitions[148,149-151] of $O^-$and I^-. These spectra typically extend over a 0 – 8,000 cm^{-1} eKE range, with a corresponding 80 – 400 cm^{-1} energy resolution. When

peaks in a H_2CCC^- spectrum do not overlap, the uncertainty in the absolute eBE is approximately the HWHM (half width at half maximum) of the peak.

5.3 Results

Photodetachment of H_2CCC^- anions result in various electronic states of the H_2CCC radical by selectively removing an electron from different orbitals within the ground state anion. Figure 5.1 shows the ground state electronic configuration ($\tilde{X}\ ^2B_1$) of the H_2CCC^- anion: [core]$(1b_1)^2(7a_1)^2(2b_2)^2(2b_1)^1$. Removing the unpaired electron yields the $\tilde{X}\ ^1A_1$ ground electronic state of the corresponding neutral molecule. Detachment of an α electron from the $2b_2$, $7a_1$, or $1b_1$ molecular orbitals gives the $\tilde{A}\ ^1A_2$, $\tilde{B}\ ^1B_1$, or $\tilde{C}\ ^1A_1$ singlet electronic states, respectively, while a β electron photodetachment from the three orbitals results in the $\tilde{b}\ ^3A_2$, $\tilde{a}\ ^3B_1$, or $\tilde{c}\ ^3A_1$ triplet states, respectively. According to Hund's rule, these triplet states are lower in energy than the singlet states with the same symmetry (e.g., $^3A_2 < {}^1A_2$). Transitions to both the ground state and the lowest triplet state of the H_2CCC radical have been reported using 351.1-nm (3.531-eV) light.[121] Interestingly, the lowest triplet state is $^3B_1$ instead of $^3A_2$; however, this is counterintuitive to what one would hypothesize from the orbital energy ordering of H_2CCC^- ($\tilde{X}\ ^2B_1$). The actual energy ordering ($^3B_1 < {}^3A_2$) can be rationalized by considering that two unpaired electrons between singlet and triplet states with B_1 symmetry have stronger coupling than the two A_2 states; therefore, the singlet-triplet splitting is significantly larger for the B_1 pair of states than for the A_2 states. This results in the following measured energy ordering: $^3B_1 < {}^3A_2 < {}^1A_2 < {}^1B_1$. To investigate these higher lying electronic excited states, laser radiation with wavelengths shorter than 351.1 nm are employed.

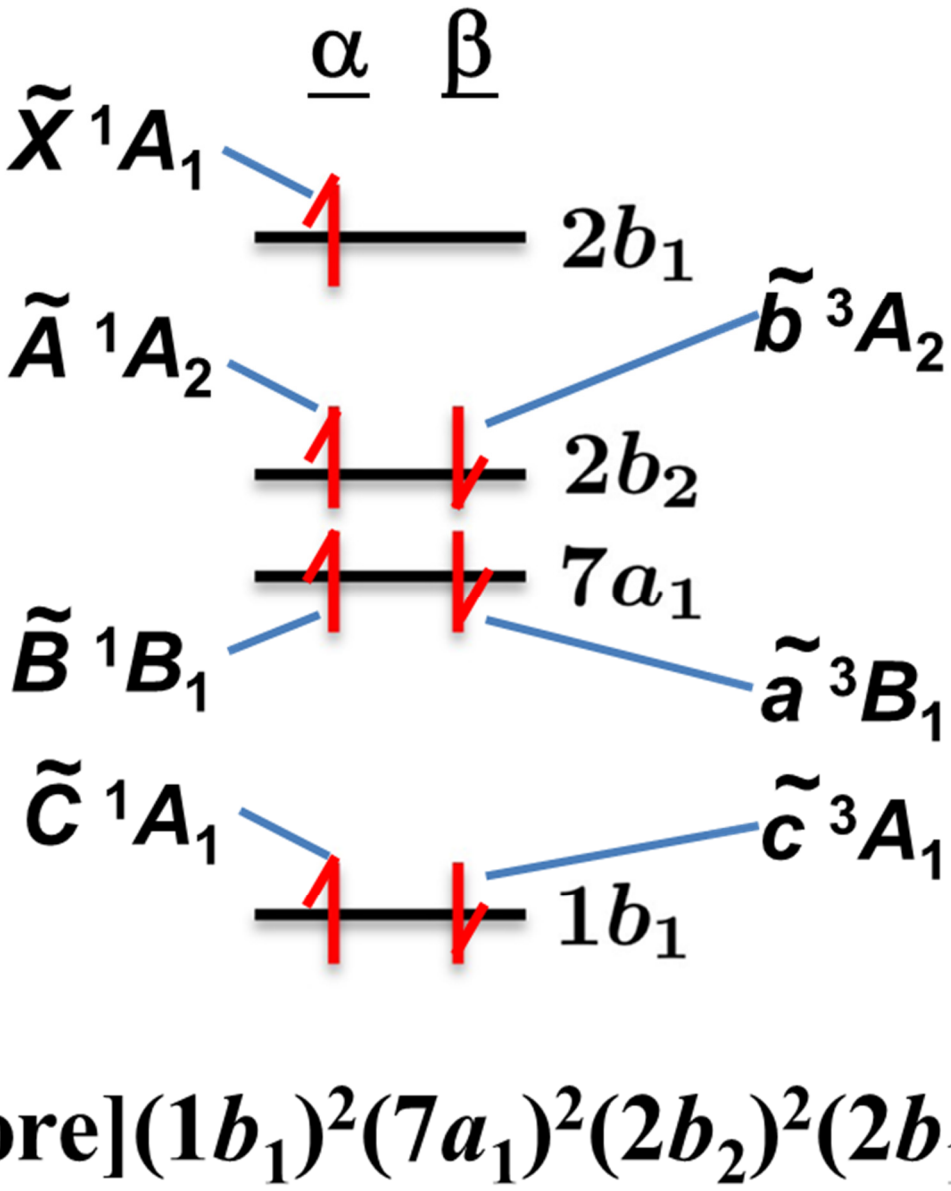

$$[\text{core}](1b_1)^2(7a_1)^2(2b_2)^2(2b_1)^1$$

Figure 5.1 Ground-state electronic configuration of propadienylidene anion, H_2CCC^-, and corresponding singlet or triplet states formed by removal of an α or a β electron.

Figure 5.2 shows the experimental photoelectron spectra taken with three different photon energies: 3.809 (black), 4.164 (red), and 4.704 (blue) eV. (Note the ground-state radical photoelectron spectrum is shown and discussed later in the chapter.) The peaks at the two lowest binding energies (eBE = 3.074(6) and 3.207(6) eV) in the black trace are assigned to the origin transition and the ν_4 fundamental ($H_2C{-}CC$ stretching), respectively, of the first excited electronic state ($\tilde{a}\,^3B_1$). These values are both in good agreement with the previous observations by Robinson *et al.*[121] The ν_4 frequency in the $\tilde{a}\,^3B_1$ state is measured to be 1073(68) cm^{-1}. To identify the higher lying features, we use previous measurements on neutral H_2CCC in addition to the measured EA, which is determined to have a value of 1.7957 eV and discussed in more detail below. In the electronic absorption spectrum of the H_2CCC radicals in a matrix, the two lowest-lying singlet excited states, $\tilde{A}\,^1A_2$ and $\tilde{B}\,^1B_1$, were observed 1.73 and 2.00 eV, respectively, higher in energy than the neutral radical in its ground electronic state.[140,141] The addition of the measured EA value to these previously measured term energies gives the expected detachment energy of the $\tilde{A}\,^1A_2$ state from the $\tilde{X}\,^2B_1$ anion to be ~3.5 eV. Therefore, the feature appearing at eBE = 3.492(6) eV in both the black and red traces of Fig. 5.2 is assigned to the origin transition of the $\tilde{A}\,^1A_2$ state. The peak at eBE = 3.685(10) eV is assigned as the ν_2 level in the $\tilde{A}\,^1A_2$ state, yielding a ν_2 frequency ($H_2CC{-}C$ stretching) of 1557(90) cm^{-1}. Similarly, the origin transition of the $\tilde{B}\,^1B_1$ state is expected to be ~3.8 eV. However, there is only one broad peak appearing at eBE = 4.065(6) eV, which is 0.265 eV (2137 cm^{-1}) higher in energy than the estimated origin of this state. We assign this peak as the ν_2 transition in the $\tilde{B}\,^1B_1$ state, and the origin is unobservable, which is probably due to strong vibronic coupling between the $\tilde{A}\,^1A_2$ and $\tilde{B}\,^1B_1$ states.

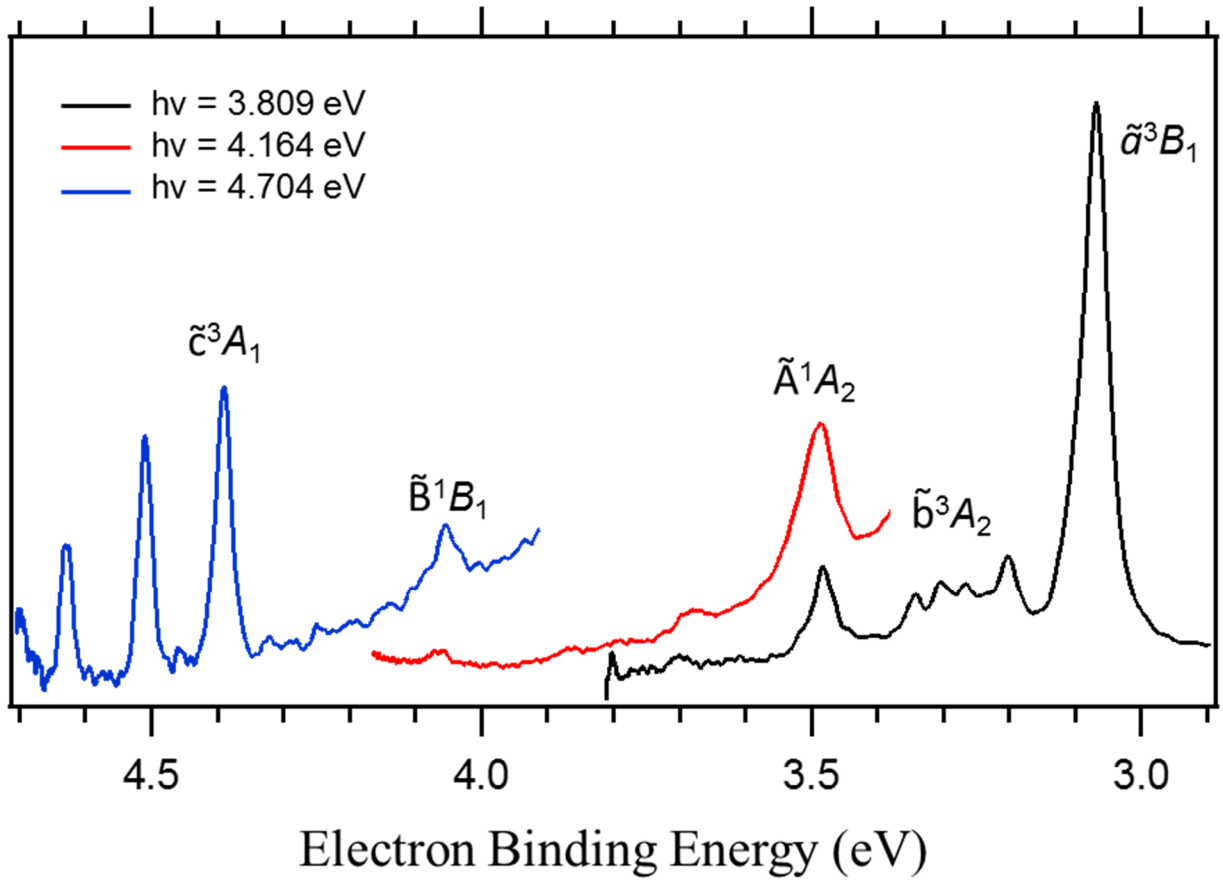

Figure 5.2 Photoelectron spectra of H_2CCC^- anion taken with photon energies of 3.809 (black), 4.164 (red), and 4.704 (blue) eV. The labels denote all origin transitions except the $\tilde{B}\ ^1B_1$ state.

There are some features around 3.3 eV, which were not observed in the work of Robinson *et al.*[121] probably due to the threshold effect. Since the term energy of the $\tilde{b}\,^3A_2$ state lies between the $\tilde{A}\,^1A_2$ and $\tilde{a}\,^3B_1$ states, the peaks at eBE = 3.269(7) and 3.307(7) eV are assigned to the origin transition and the first overtone of the ν_9 level (CCC in-plane bending), respectively, of the $\tilde{b}\,^3A_2$ state. The ν_9 mode (b_2 symmetry) in the $\tilde{b}\,^3A_2$ state becomes active due to a vibronic coupling with the $\tilde{a}\,^3B_1$ state, lending intensity to this transition.[152] However, the peak at eBE = 3.348(7) eV in the black trace shown in Fig. 5.2 cannot be assigned to any level of what state.

Unlike the complicated features below 4 eV, the structure of the $\tilde{c}\,^3A_1$ state in the blue trace of Fig. 5.2 is straightforward. The origin of this state appears at 4.391(4) eV, and the position of the adjacent peak is 4.510(5) eV. The spacing is 0.119(7) eV or 960(56) cm^{-1}, and this transition is assigned as the ν_4 fundamental ($H_2C{-}CC$ stretching). The position of next peak, 4.629(5) eV, may be the $2\nu_4$ level. However, there is a Fermi resonance between the $2\nu_4$ and ν_2 modes, so things become more complicated and uncertain.[152]

5.4 Discussion

This work was combined with Negative-Ion Photoelectron Spectroscopy (NIPES) at JILA and Slow Electron Velocity-map Imaging (SEVI) at Berkeley to obtain a moderately high-resolution photoelectron spectrum over the range of eBE from 1.49 to 4.71 eV, shown in Fig. 5.3. Before discussing details, one can notice that data are all consistent, and particularly, SEVI offers the highest resolution measurement of the three techniques. However, some SEVI signals can disappear due to threshold effects. In addition, NIPES has constant energy resolution over the entire spectrum, but the range of eBE is limited by the fixed-laser frequency, prohibiting investigation of higher-lying excited states of the H_2CCC radical.

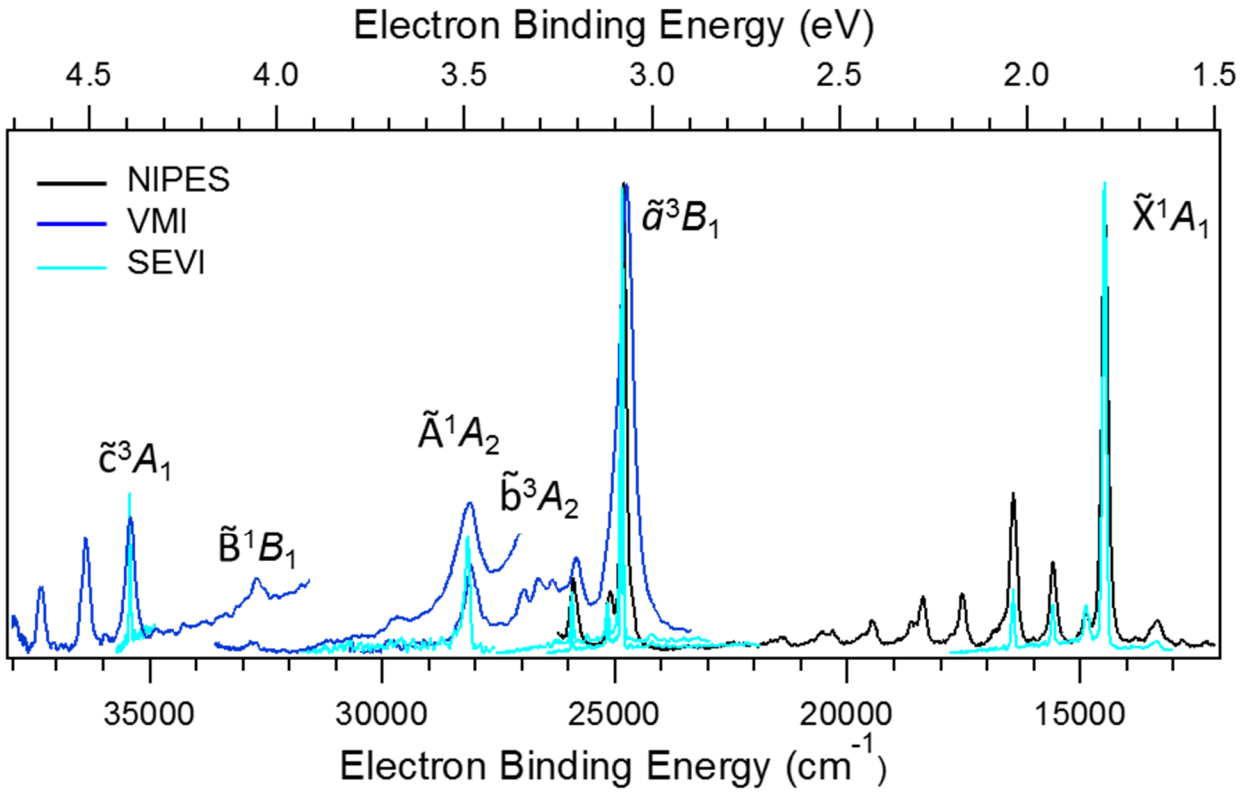

Figure 5.3 Composite photoelectron spectrum of H_2CCC^- anion using NIPES, VMI, and SEVI techniques. The three techniques are color-coded in black, blue, and cyan, respectively. The labels indicate the origins of different electronic states of H_2CCC radical except the $\tilde{B}\ ^1B_1$ state.

From SEVI measurements, the more precise EA of the H_2CCC radical is determined to be 1.7957(10) eV, in excellent agreement with the previously reported EA of 1.794(8) eV by Robinson *et al.*[121] The dominant vibrational progression includes ν_2 (H_2CC–C stretching) and ν_4 (H_2C–CC stretching) modes. Minor contributions from the $2\nu_6$ (CCC out-of-plane bending) and $2\nu_5$ (HCH out-of-plane wagging) levels are also revealed. The peak positions of the $\tilde{a}\ ^3B_1$, $\tilde{b}\ ^3A_2$, $\tilde{A}\ ^1A_2$ and $\tilde{c}\ ^3A_1$ origins are 3.0794(10), 3.2773(25), 3.4914(10) and 4.3923(10) eV, respectively. The corresponding term energies are 1.2837(14), 1.4816(27), 1.6957(14), and 2.5966(14) eV, respectively. These experimental values are summarized in Table 5.1. Additionally, there is a $2\nu_9$ (CCC in-plane bending) level in the $\tilde{a}\ ^3B_1$ state resolved in the NIPES and SEVI spectra because the vibronic coupling between $\tilde{a}\ ^3B_1$ and $\tilde{b}\ ^3A_2$ states lends intensity to the ν_9 mode. Some vibrational levels missing in the SEVI spectra are captured with our VMI measurement and described in the results section. With the aid of calculations and simulations, we gain further insight into the observations and assignments, such as the complex singlet–triplet splittings of the excited states of B_1 and A_2 symmetries. Table 5.1 summarizes the experimental and calculated values for comparison.

Table 5.1. Comparison between experimental and calculated detachment energies and term energies.

		Detach. Energy (eV)	Term Energy (eV)	
		Experiment	Experiment	Calculation
Species	State	Adiabatic		EOM-CCSDTQ
H_2CCC^-	$\tilde{X}\,^2B_1$	0		
H_2CCC	$\tilde{X}\,^1A_1$	1.7957 ± 0.0010	0	0
	$\tilde{a}\,^3B_1$	3.0794 ± 0.0010	1.2837 ± 0.0014	1.3480
	$\tilde{b}\,^3A_2$	3.2773 ± 0.0025	1.4816 ± 0.0027	1.5637
	$\tilde{A}\,^1A_2$	3.4914 ± 0.0010	1.6957 ± 0.0014	1.7302
	$\tilde{B}\,^1B_1$			2.0281
	$\tilde{c}\,^3A_1$	4.3923 ± 0.0010	2.5966 ± 0.0014	2.5967

Maier *et al.* recently proposed[142] that broad DIBs at 4881 Å and 5450 Å are attributed to the $\tilde{B}\,^1B_1 \leftarrow \tilde{X}\,^1A_1$ transition of H_2CCC. Using our experimental results, the position of the ν_2 band in the $\tilde{B}\,^1B_1$ state, eBE = 4.065(6) eV, lies 2.269(6) eV above the H_2CCC ground state (EA = 1.7957(10) eV), which corresponds to a wavelength range between 5449 and 5479 Å. This result is consistent with the electronic absorption of H_2CCC at 5450 Å in the work of Maier *et al.* However, the astronomical assignment is controversial and has been criticized.[143-145] Araki and coworkers searched for the rotational transition of H_2CCC toward HD 183143 using a radio telescope.[145] They concluded that the major DIBs carrier at 4881 and 5450 Å should not be attributed to H_2CCC due to low column density. Similarly, Liszt *et al.* directly measured the column density of H_2CCC with radio telescopes in four diffuse clouds and TMC-1 (Taurus molecular cloud 1).[144] They found that the observed column density of H_2CCC is three orders of magnitude lower than the required column density to explain the DIBs, suggesting that H_2CCC is not a possible carrier of DIBs due to apparently low abundance. Thus, the hypothesis by Maier *et al.*[142] is very unlikely to be correct.

5.5 Conclusion

In this work, we measured the photoelectron spectra of H_2CCC^- anion with three different photon energies. The five lowest-lying excited states are observed and assigned as well as the active vibrational levels. The $\tilde{B}\,^1B_1$ origin is not observed and not assigned since strong vibronic coupling between the $\tilde{A}\,^1A_2$ and $\tilde{B}\,^1B_1$ states makes the origin transition unclear. Finally, combining experiment and theory gains further insight into the spectral observations and assignments.

Chapter 6
Photoelectron Spectroscopy of Propargylene Anion, $HCCCH^-$

6.1 Introduction

Isomers of C_3H_2 are important in organic, astrophysical, and combustion chemistry. Singlet cyclopropenylidene (*c*-C_3H_2) is the global minimum structure, which has two low-lying isomers: triplet propargylene (HCCCH, ΔE = 10 kcal/mol) and singlet propadienylidene ($H_2C{=}C{=}C{:}$, ΔE = 13 kcal/mol).[133] Cyclopropenylidene is one of the most abundant organic molecules in interstellar clouds,[153,144] and propadienylidene has been suggested as a carrier of the diffuse interstellar bands (DIBs), which is still being debated and described in Chapter 5. Propargylene, also called propynylidene, has not yet been detected in space due to its small dipole moment. HCCCH has a ^3B electronic ground state with C_2 symmetry, according to matrix EPR and IR spectroscopy studies, as well as theoretical calculations.[154] The electronic absorption spectrum of HCCCH in an Ar matrix has been investigated, exhibiting broad absorption bands and vibrational structures.[133,154] The lowest broad band, spanning from 350 to 275 nm, can be assigned to a combination of the $\tilde{A}$ ^3B and $\tilde{B}$ ^3A states. However, several excited electronic states, including singlet and triplet states, have been computed to lie within this range.[155,156] Since no conclusive experimental assignments have been reported thus far, further characterization and assignment of the excited electronic states is necessary.

In this chapter, we report the photoelectron spectrum of $HCCCH^-$ anion. We utilize a neutral–entrainment anion source to produce $HCCCH^-$, allowing us to investigate the neutral electronic excited states following electron detachment. We measure the term energies and

vibrational levels for multiple excited electronic states of HCCCH. Finally, we compare the experimental results, collected in two laboratories, with calculated values.

6.2 Experimental Details

The VMI photoelectron spectrometer has been described in detail in Chapter 2. This experimental apparatus uses a pulsed anion beam, mass separation by a Wiley-McLaren time-of-flight mass spectrometer (TOF MS),[24] a tunable laser source, and a VMI detector.

For anion preparation, we employ the O^- + propyne reaction first observed by Dawson *et al.*[157] and form $HCCCH^-$ in a pulsed supersonic entrainment reactor.[46] Dawson and coworkers found that the O^- + propyne ($H_3CC{\equiv}CH$) reaction produces both H_2CCC^- and $HCCCH^-$ products whereas the reaction of O^- with propyne's isomer, allene ($H_2C{=}C{=}CH_2$), produces $C_3H_2^-$ in nearly pure H_2CCC^- isomeric form. The photoelectron spectra of the m/z = 38 anion arising from both reactions (O^- + propyne and O^- + allene) are taken under the same experimental conditions in the present experiment. The entrainment reactor consists of a central and two side pulsed General Valves operating at a repetition rate of 80 Hz with separate timings and pulse widths. The middle valve provides the main expansion using 1% propyne or 1% allene seeded in Ar at a stagnation pressure of 4.1 atm. One of the side valves entrains neat N_2O into the main expansion. Collisions of the gas expansion with a guided 1-keV electron beam yield slow secondary electrons that form the O^- reactant through dissociative electron attachment of N_2O. Subsequently, the O^- reacts with propyne or allene to form the m/z = 38 anion. If the N_2O entrainment valve is turned off, the m/z = 38 signal disappears.

The anions are perpendicularly extracted and mass-separated using a Wiley-McLaren TOF MS. Anions of m/z = 38 are photodetached by spatially and temporally overlapping them with the fourth harmonic generation (FHG, 266 nm or 4.660 eV) of an Nd:YAG laser or a tunable-light pulse (5.158, 4.704 or 2.352 eV) from the frequency-doubled or fundamental signal output of a 355-nm pumped optical parametric oscillator. Then, the kinetic energy distribution of the ejected electrons is acquired by the VMI photoelectron spectrometer. In this chapter, we report photoelectron spectra as a function of electron binding energy (eBE= ħω – eKE), which is independent of the laser wavelength used for photodetachment. The energy scale for the reported images is calibrated using the well-known photoelectron spectrum of I^-.[149-151] The spectra reported here cover an eKE range from 0 to 1.2 eV, with a declining energy resolution of 10 to 60 meV across this range.

6.3 Results

Figure 6.1 shows the photoelectron spectra of the product anions from O^- + allene and O^- + propyne with a photon energy of 2.352 eV. O^- can abstract a proton and a hydrogen atom from a compound at the same time (i.e., H_2^+ abstraction) and produce a new radical anion along with water. For the reaction of O^- with C_3H_4, the isomer distribution of the $C_3H_2^-$ product anions depends on the isomeric form of the C_3H_4 reactant.[157] The O^- + allene reaction results in the photoelectron spectrum of H_2CCC^-, plotted in black, which has been described in Chapter 5. In contrast, when O^- reacts with propyne, the red trace in Fig. 6.1 shows many new features in addition to those seen in the black trace. This comparison provides direct evidence that the reaction of O^- with propyne produces at least one additional isomer of $C_3H_2^-$. In a separate experiment,

Osborn and coworkers have taken the photoelectron spectra of the product anions from O^- + propyne reaction using the Negative Ion Photoelectron Spectroscopy (NIPES) instrument at JILA.[158] They confirmed that the O^- + propyne reaction produces both H_2CCC^- and $HCCCH^-$ products. Although the neutral–entrainment anion source in the VMI instrument is different from the flowing afterglow ion source in the NIPES instrument, the features from 1.4 to 2.1 eV binding energy between two instruments show the same isomer-specific chemistry. Therefore, for all photon energies in this chapter, the black spectra (O^- + allene) arise from photodetachment of H_2CCC^-, whereas features in the red spectra (O^- + propyne) that are not present in the black spectra can be assigned to transitions from the propargylene anion, $HCCCH^-$. For this Chapter, the focus will be on the assignment of those peaks attributed to detachment from the $HCCCH^-$ isomer.

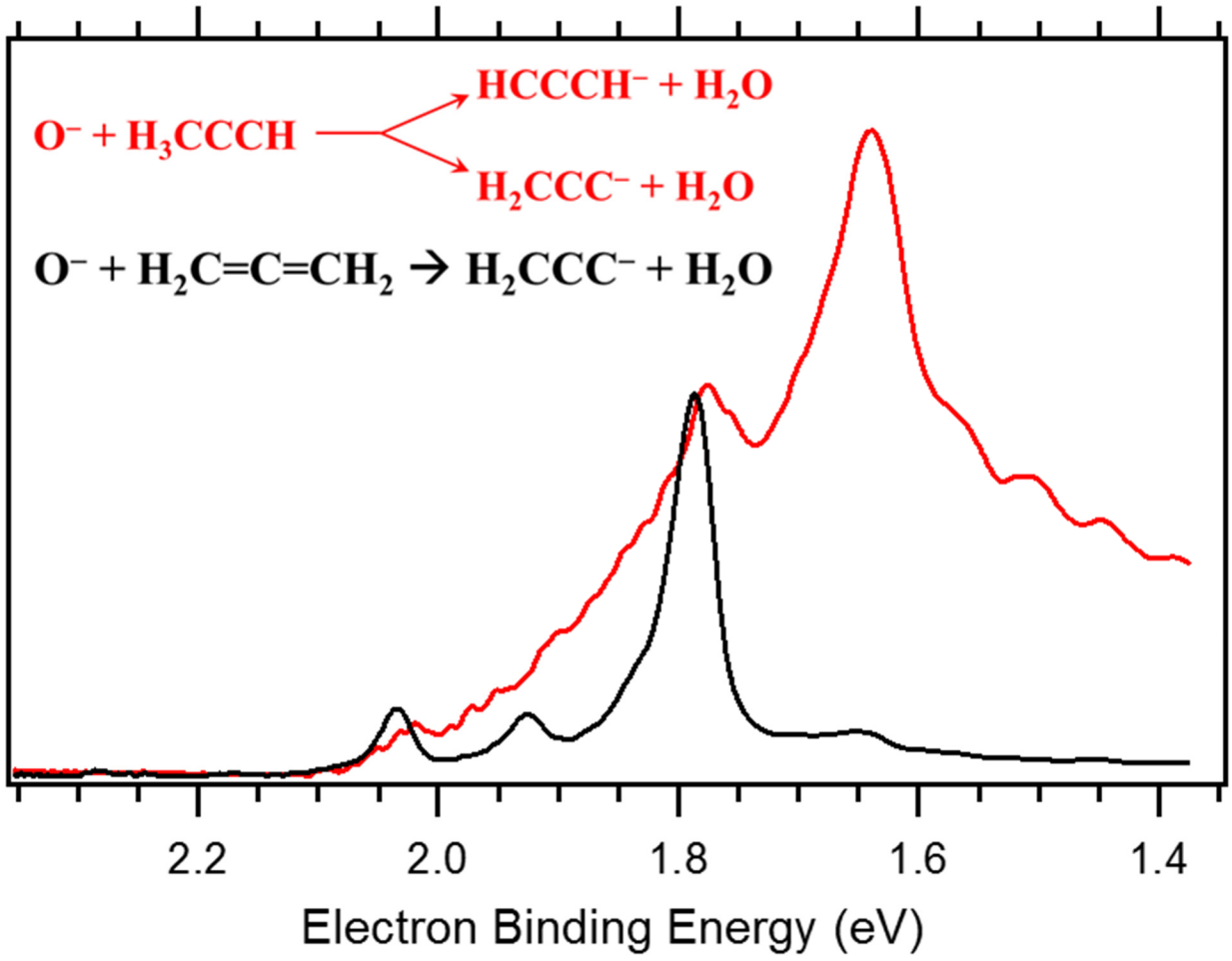

Figure 6.1 Photoelectron spectra of the product anions from O^- + allene (black), and O^- + propyne (red) acquired with the VMI photoelectron spectrometer. Spectra were taken with $\hbar\omega$ = 2.352 eV.

Using higher photon energy of 4.660 and 4.704 eV, we observe the photoelectron spectra shown in Fig. 6.2, which could not be acquired on the NIPES instrument. From this comparison, the features in the red spectrum that are not present in the black spectrum exhibit a well-resolved, short vibrational progression. We attribute the peaks at eBE = 4.454(5) and 4.590(5) eV in the red spectrum to an electronic excited state of HCCCH, assigned in the Discussion section. In order to access still higher electronic states of HCCCH, we use a greater photon energy of 5.158 eV. The photoelectron spectra, presented in Fig. 6.3, show two additional features at eBE = 4.738(5) and 4.869(5) eV.

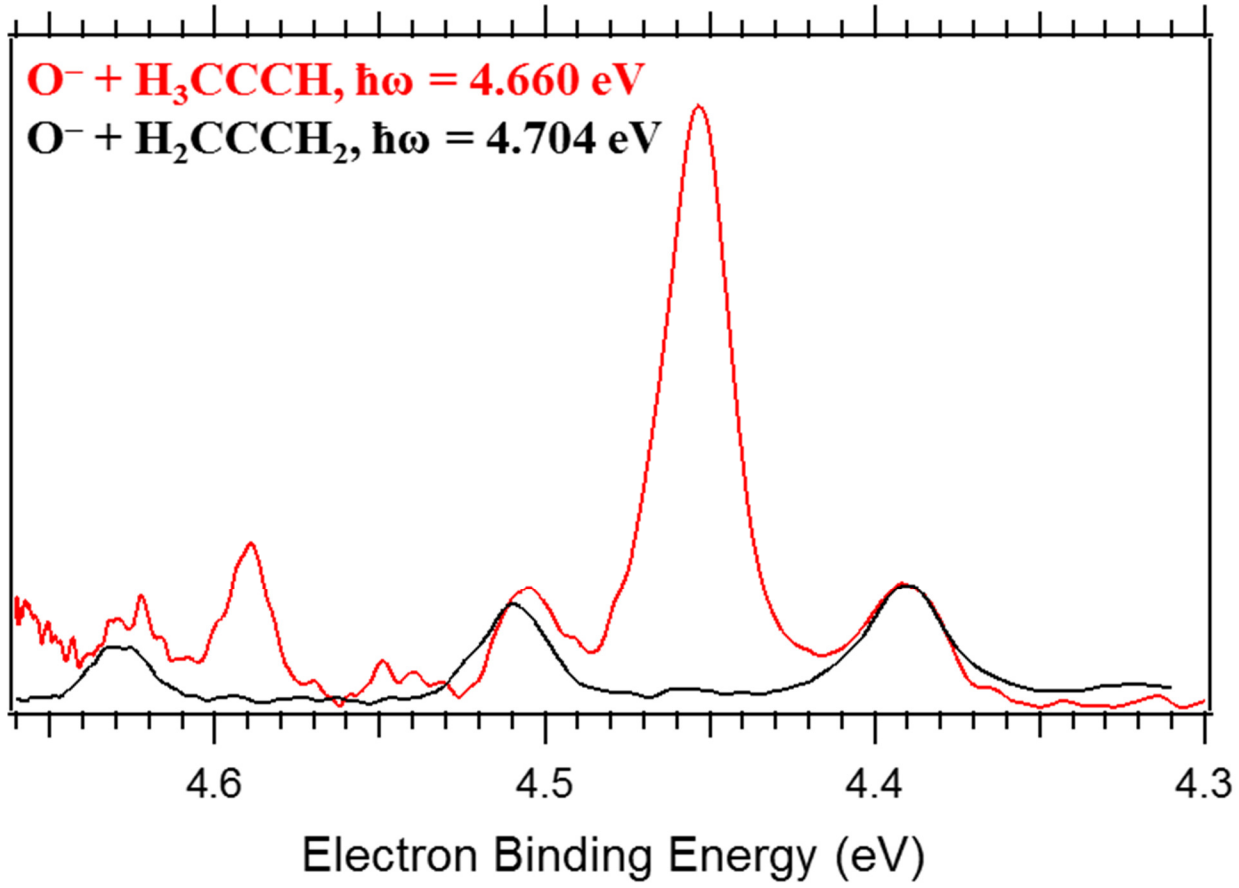

Figure 6.2 Photoelectron spectra of the product anions from O^- + allene (black) and O^- + propyne (red) reactions. Spectra in red were acquired with ħω = 4.660 eV, and in black with ħω = 4.704 eV.

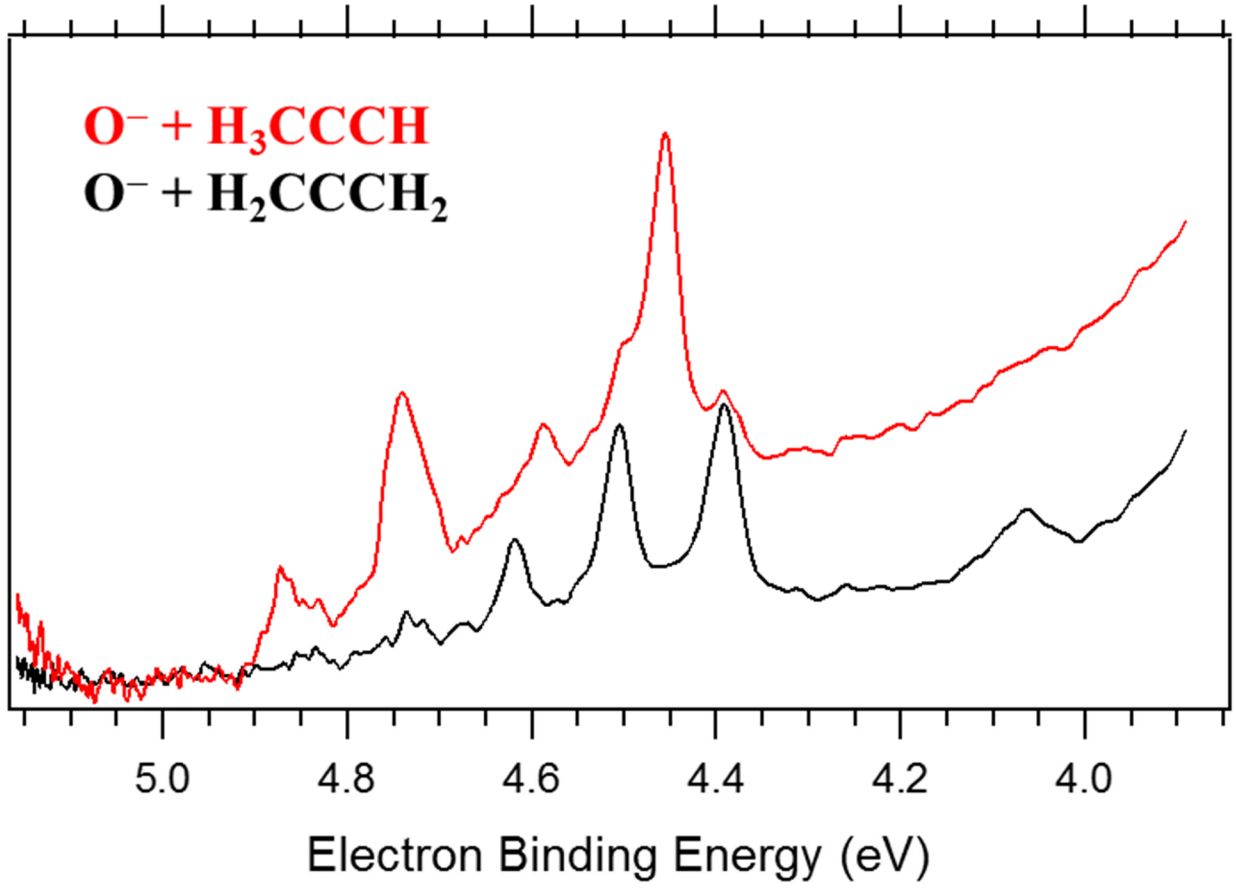

Figure 6.3 Photoelectron spectra of the product anions from O^- + allene (black) and O^- + propyne (red) reactions. Both spectra were taken with $\hbar\omega$ = 5.158 eV.

6.4 Discussion

This work is combined with NIPES at JILA to cover the eBE range of 0.9 to 5.1 eV. We compare these results with high-level electronic structure calculations to gain further insight into the electronic structure of HCCCH. Before going into detail about the spectra obtained in the VMI instrument, a brief overview of the findings from the NIPES experiment is presented.[158] Through comparison of the $HCCCH^-$ and $DCCCD^-$ photoelectron spectra, the EA of HCCCH is determined to be $1.156 \pm^{0.010}_{0.095}$ eV, with a singlet-triplet splitting between the $\tilde{X}\,^3B$ and the $\tilde{a}\,^1A$ states of ΔE_{ST} = $0.500 \pm^{0.10}_{0.01}$ eV. The experimental term energy of the higher excited state, $\tilde{b}\,^1B$, is $0.94 \pm^{0.22}_{0.20}$ eV. Transitions to both $\tilde{X}\,^3B$ and $\tilde{b}\,^1B$ states exhibit long vibrational progressions, a portion of which can be seen in Fig. 6.1, and are assigned to the ν_4 mode (in-plane symmetric CCH bend) of the $\tilde{X}\,^3B$ state, indicating a large geometry change from the anion to the neutral.

Regarding the electronic structure calculation, Osborn and coworkers employ CCSD(T) for the lowest electronic state of each symmetry and multi-reference configuration interaction (MRCI) level of theory for all electronic states in order to calculate the geometries and transition energies.[158] Note that there is a low-lying excited state, $\tilde{A}\,^2A$, in the anion, which could be populated in the anion beam. However, since there is no experimentally observed splitting arising from the two predicted anion states, we consider only one anion state in our interpretation of transitions to all neutral states. The experimental and calculated values are summarized in Table 6.1. The calculated large CCH bond angle change from anion (126°) to neutral ($\tilde{X}\,^3B$, 160°; $\tilde{b}\,^1B$, 180°) is consistent with the long vibrational progression of the CCH bend seen in the NIPES experiment. The other calculated geometries presented in Table 6.1 will be used below to aid in the assignment of higher excited electronic states seen in the VMI data.

The peak assignments in the VMI data are rather complicated. Background signals inherent in these experiments prohibit quantifying the angular distributions from the VMI apparatus, which contains crucial information for the assignment of electronic states. Based on the peak intensities, the 4.454 eV peak (Fig. 6.2-6.3) is likely the origin of an electronic state. Above the 4.454 eV peak, the peak at 4.590 eV is tentatively assigned as the CCC stretch mode (ν_2), indicating a ν_2 frequency of 0.136 eV (1,097 cm^{-1}). However, a third peak is located at 4.738 eV, lying 0.284 eV (2,291 cm^{-1}) above the 4.454 eV peak. This spacing cannot be due to a fundamental vibrational mode or, based on intensities, a combination band. Therefore, we assign the peak at 4.738 eV as the origin of an additional excited electronic state of HCCCH with a similar geometry to the anion. According to the MRCI results in Table 6.1, the $\tilde{c}\ ^1$A and $\tilde{A}\ ^3$B states both have large geometry changes compared to the anion, which would lead to extensive vibrational progressions or make them difficult to observe. Thus, this 4.738 eV feature is not due to the $\tilde{c}\ ^1$A or $\tilde{A}\ ^3$B states. In contrast, the $\tilde{d}\ ^1$A and $\tilde{B}\ ^3$A states have small geometry changes compared to the $\tilde{A}\ ^2$A and $\tilde{X}\ ^2$B anionic states, respectively, which is consistent with the trends seen in the photoelectron spectrum. Based on calculated energetics, the best match with the experimental origin peak at 4.454 eV is the $\tilde{d}\ ^1A_2$ state, and the peak at 4.738 eV is assigned as the $\tilde{B}\ ^3$A state. The feature at 4.869 eV lies 0.131 eV (1057 cm^{-1}) above the origin of the $\tilde{B}\ ^3$A state. We assign this peak as excitation of the ν_2 mode in the $\tilde{B}\ ^3$A state. Thus, the term energies of the $\tilde{d}\ ^1$A and $\tilde{B}\ ^3$A states are $3.298 \pm^{0.10}_{0.01}$ and $3.582 \pm^{0.10}_{0.01}$ eV, respectively. The term energy of the $\tilde{B}\ ^3$A state is also in a good agreement with the UV/Vis absorption spectrum of the triplet ground-state HCCCH, which exhibited a broad absorption from 350 to 275 nm and can be assigned to an absorption to a combination of the $\tilde{A}\ ^3$B and $\tilde{B}\ ^3$A states.[133,154]

Table 6.1. Comparison between experimental and calculated detachment energies and term energies.

				Adiabatic Detachment Energy (eV)			Term Energy (eV)
Species	State	∠CCC (°)	∠HCC (°)	CCSD(T)/CBS	MRCI/CBS	Experiment	Experiment
$HCCCH^-$	$\tilde{X}\,^2B$	179	126	0	0	0	
	$\tilde{A}\,^2A$	163	123	0.026	0.014		
HCCCH	$\tilde{X}\,^3B$	173	160	1.146	1.03	$1.156 \pm^{0.010}_{0.095}$	0
	$\tilde{a}\,^1A$	180	129		1.48	1.165 ± 0.005	$0.500 \pm^{0.10}_{0.01}$
	$\tilde{b}\,^1B$	180	180		1.82	2.100 ± 0.2	$0.940 \pm^{0.22}_{0.20}$
	$\tilde{c}\,^1A$	180	180		2.48		
	$\tilde{A}\,^3B$	108	131		4.26		
	$\tilde{d}\,^1A$	160	135		4.29	4.454 ± 0.005	$3.298 \pm^{0.10}_{0.01}$
	$\tilde{B}\,^3A$	180	128		4.36	4.738 ± 0.005	$3.582 \pm^{0.10}_{0.01}$

6.5 Conclusion

In this work, we recorded the photoelectron spectra of the $HCCCH^-$ anion using three different photon energies. The three lowest-lying electronic states ($\tilde{X}\ ^3B$, $\tilde{a}\ ^1A$, and $\tilde{b}\ ^1B$) were measured in the NIPES instrument to obtain the EA and singlet-triplet splitting of HCCCH. From the VMI experiments, origin transitions of the $\tilde{d}\ ^1A_2$ and $\tilde{B}\ ^3A_2$ states are assigned and characterized based on a small geometry change from the anion. The HCCCH $\tilde{c}\ ^1A$ and $\tilde{A}\ ^3B$ states were not observed.

Bibliography

1. B. Brehm, M. A. Gusinow, and J. L. Hall, "Electron Affinity of Helium *via* Laser Photodetachment of its Negative Ion," *Phys. Rev. Lett.* **19,** 737 (1967).

2. K. M. Ervin and W. C. Lineberger, Photoelectron spectroscopy of molecular anions in *Advances in Gas Phase Ion Chemistry*, Vol. 1, edited by N. G. Adams and L. M. Babcock (JAP Press, Greenwich), p. 121 [1992].

3. D. M. Neumark, "Slow Electron Velocity-Map Imaging of Negative Ions: Applications to Spectroscopy and Dynamics," *J. Phys. Chem. A* **112,** 13287 (2008).

4. A. Sanov and R. Mabbs, "Photoelectron imaging of negative ions," *Int. Rev. Phys. Chem.* **27,** 53 (2008).

5. B. J. Greenblatt, M. T. Zanni, and D. M. Neumark, "Photodissociation of $I_2^-(Ar)_n$Clusters Studied with Anion Femtosecond Photoelectron Spectroscopy," *Science* **276,** 1675 (1997).

6. M. T. Zanni, B. J. Greenblatt, A. V. Davis, and D. M. Neumark, "Photodissociation of gas phase I_3^- using femtosecond photoelectron spectroscopy," *J. Chem. Phys.* **111,** 2991 (1999).

7. N. J. Kim, D. H. Paik, and A. H. Zewail, "Femtosecond dynamics of solvated oxygen anions. II. Nature of dissociation and caging in finite-sized clusters," *J. Chem. Phys.* **118,** 6930 (2003).

8. R. Wester, A. E. Bragg, A. V. Davis, and D. M. Neumark, "Time-resolved study of the symmetric SN_2-reaction I^-+CH_3I," *J. Chem. Phys.* **119,** 10032 (2003).

9. R. Mabbs, K. Pichugin, and A. Sanov, "Time-resolved imaging of the reaction coordinate," *J. Chem. Phys.* **122,** 174305 (2005).

10. J. R. Verlet, A. Kammrath, G. B. Griffin, and D. M. Neumark, "Electron solvation in water clusters following charge transfer from iodide," *J. Chem. Phys.* **123,** 231102 (2005).

11. L. R. McCunn, G. H. Gardenier, T. L. Guasco, B. M. Elliott, J. C. Bopp, R. A. Relph, and M. A. Johnson, "Probing isomer interconversion in anionic water clusters using an Ar-mediated pump-probe approach: Combining vibrational predissociation and velocity-map photoelectron imaging spectroscopies," *J. Chem. Phys.* **128,** 234311 (2008).

12. L. Sheps, E. M. Miller, S. Horvath, M. A. Thompson, R. Parson, A. B. McCoy, and W. C. Lineberger, "Solvent-Mediated Electron Hopping: Long-Range Charge Transfer in $IBr^-(CO_2)$ Photodissociation," *Science* **328,** 220 (2010).

13. K. M. Ervin, "Experimental Techniques in Gas-Phase Ion Thermochemistry," *Chem. Rev.* **101,** 391 (2001).

14. W. C. Lineberger and W. T. Borden, "The Synergy Between Qualitative Theory, Quantitative Calculations and Direct Experiments in Understanding, Calculating, and Measuring the Energy Differences Between the Lowest Singlet and Triplet States of Organic Diradicals," *Phys. Chem. Chem. Phys.* **13,** 11792 (2011).

15. D. G. Leopold, K. K. Murray, A. E. S. Miller, and W. C. Lineberger, "Methylene: A study of the $\tilde{X}\,^3B_1$ and $\tilde{a}\,^1A_1$ states by photoelectron spectroscopy of CH_2^- and CD_2^-," *J. Chem. Phys.* **83,** 4849 (1985).

16. E. Surber, R. Mabbs, and A. Sanov, "Probing the Electronic Structure of Small Molecular Anions by Photoelectron Imaging," *J. Phys. Chem. A* **107,** 8215 (2003).

17. E. P. Wigner, "On the Behavior of Cross Sections Near Thresholds," *Phys. Rev.* **73,** 1002 (1948).

18. K. J. Reed, A. H. Zimmerman, H. C. Andersen, and J. I. Brauman, "Cross sections for photodetachment of electrons from negative ions near threshold," *J. Chem. Phys.* **64,** 1368 (1976).

19. J. Cooper and R. N. Zare, "Angular Distribution of Photoelectrons," *J. Chem. Phys.* **48,** 942 (1968).

20. R. L. Schwartz, G. E. Davico, T. M. Ramond, and W. C. Lineberger, "Singlet–Triplet Splittings in CX_2 (X = F, Cl, Br, I) Dihalocarbenes via Negative Ion Photoelectron Spectroscopy," *J. Phys. Chem. A* **103,** 8213 (1999).

21. G. J. Rathbone, T. J. Sanford, D. H. Andrews, and W. C. Lineberger, "Photoelectron imaging spectroscopy of $Cu^-(H_2O)_{1,2}$ anion complexes," *Chem. Phys. Lett.* **401,** 570 (2005).

22. T. J. Sanford, S.-Y. Han, M. A. Thompson, R. Parson, and W. C. Lineberger, "Photodissociation dynamics of $IBr^-(CO_2)_n$, n<15," *J. Chem. Phys.* **122,** 054307 (2005).

23. L. Sheps, E. M. Miller, and W. C. Lineberger, "Photoelectron spectroscopy of small $IBr^-(CO_2)_n$, (n=0-3) cluster anions," *J. Chem. Phys.* **131,** 064304 (2009).

24. W. C. Wiley and I. H. McLaren, "Time-of-Flight Mass Spectrometer with Improved Resolution," *Rev. Sci. Instrum.* **26,** 1150 (1955).

25. D. W. Chandler and P. L. Houston, "Two-Dimensional Imaging of State-Selected Photodissociation Products Detected by Multiphoton Ionization," *J. Chem. Phys.* **87,** 1445 (1987).

26. A. T. J. B. Eppink and D. H. Parker, "Velocity map imaging of ions and electrons using electrostatic lenses: Application in photoelectron and photofragment ion imaging of molecular oxygen," *Rev. Sci. Instrum.* **68,** 3477 (1997).

27. M. A. Johnson and W. C. Lineberger, Pulsed Methods for Cluster Ion Spectroscopy in *Techniques for the Study of Ion Molecule Reactions*, edited by J. M. Farrar and J. W. Saunders (Wiley, New York), p. 591 [1988].

28. D. L. Osborn, D. J. Leahy, D. R. Cyr, and D. M. Neumark, "Photodissociation spectroscopy and dynamics of the $(N_2O_2)_2$ anion," *J. Chem. Phys.* **104,** 5026 (1996).

29. D. W. Boo, Y. Ozaki, L. H. Andersen, and W. C. Lineberger, "Femtosecond Dynamics of Linear Ag_3," *J. Phys. Chem. A* **101,** 6688 (1997).

30. X. Li, A. Grubisic, S. T. Stokes, J. Cordes, G. F. Ganteför, K. H. Bowen, B. Kiran, M. Willis, P. Jena, R. Burgert, and H. Schnöckel, "Unexpected Stability of Al_4H_6: A Borane Analog?," *Science* **315,** 356 (2007).

31. E. Garand, T. I. Yacovitch, and D. M. Neumark, "Slow photoelectron velocity-map imaging spectroscopy of C_2N^-, C_4N^-, and C_6N^-," *J. Chem. Phys.* **130,** 064304 (2009).

32. O. Cheshnovsky, S. H. Yang, C. L. Pettiette, M. J. Craycraft, Y. Liu, and R. E. Smalley, "Ultraviolet photoelectron spectroscopy of semiconductor clusters: Silicon and germanium," *Chem. Phys. Lett.* **138,** 119 (1987).

33. D. W. Arnold, S. E. Bradforth, T. N. Kitsopoulos, and D. M. Neumark, "Vibrationally resolved spectra of C_2–C_{11} by anion photoelectron spectroscopy," *J. Chem. Phys.* **95,** 8753 (1991).

34. L.-S. Wang, H.-S. Cheng, and J. Fan, "Photoelectron spectroscopy of size-selected transition metal clusters: Fe_n^-, n=3–24," *J. Chem. Phys.* **102,** 9480 (1995).

35. W. Zheng, S. Xu, D. Radisic, S. Stokes, X. Li, and K. H. Bowen Jr., "On the interaction of electrons with betaine zwitterions," *J. Chem. Phys.* **122,** 101103 (2005).

36. X.-B. Wang and L.-S. Wang, "Development of a low-temperature photoelectron spectroscopy instrument using an electrospray ion source and a cryogenically controlled ion trap," *Rev. Sci. Instrum.* **79,** 073108 (2008).

37. T. R. Rizzo, J. A. Stearns, and O. V. Boyarkin, "Spectroscopic studies of cold, gas-phase biomolecular ions," *Int. Rev. Phys. Chem.* **28,** 481 (2009).

38. M. Z. Kamrath, R. A. Relph, T. L. Guasco, C. M. Leavitt, and M. A. Johnson, "Vibrational predissociation spectroscopy of the H_2-tagged mono- and dicarboxylate anions of dodecanedioic acid," *Int. J. Mass Spectrom. Ion Processes* **300,** 91 (2011).

39. K. R. Asmis and D. M. Neumark, "Vibrational Spectroscopy of Microhydrated Conjugate Base Anions," *Accounts Chem. Res.* **45,** 43 (2012).

40. J. J. Grabowski and S. J. Melly, "Formation of Carbene Radical-Anions - Gas-Phase Reaction of the Atomic Oxygen Anion with Organic Neutrals," *Int. J. Mass Spectrom. Ion Processes* **81,** 147 (1987).

41. S. T. Graul and R. T. Squires, "Advances in Flow Reactor techniques," *Mass Spectrosc. Rev.* **7,** 263 (1988).

42. J. Lee and J. J. Grabowski, "Reactions of the Atomic Oxygen Radical-Anion and the Synthesis of Organic Reactive Intermediates," *Chem. Rev.* **92,** 1611 (1992).

43. P. G. Wenthold, J. Hu, and R. R. Squires, "Regioselective Synthesis of Biradical Negative Ions in the Gas-Phase. Generation of Trimethylenemethane, meta-Benzyne, and para-Benzyne Anions," *J. Am. Chem. Soc.* **116,** 6961 (1994).

44. R. Campargue, "Aerodynamic Separation Effect on Gas and Isotope Mixtures Induced by Invasion of the Free Jet Shock Wave Structure," *J. Chem. Phys.* **52,** 1795 (1970).

45. R. Campargue, "Progress in overexpanded supersonic jets and skimmed molecular beams in free-jet zones of silence," *J. Phys. Chem.* **88,** 4466 (1984).

46. W. H. Robertson, J. A. Kelley, and M. A. Johnson, "A pulsed supersonic entrainment reactor for the rational preparation of cold ionic complexes," *Rev. Sci. Instrum.* **71,** 4431 (2000).

47. J. M. Weber, "A pulsed ion source for the preparation of metal containing cluster anions using supersonic entrainment of laser vaporized metal," *Rev. Sci. Instrum.* **76,** 043301 (2005).

48. L. A. Posey, M. J. Deluca, and M. A. Johnson, "Demonstration of a pulsed photoelectron spectrometer on mass-selected negative ions: O^-, O_2^-, and O_4^-," *Chem. Phys. Lett.* **131,** 170 (1986).

49. V. Dribinski, A. Ossadtchi, V. A. Mandelshtam, and H. Reisler, "Reconstruction of Abel-transformable images: The Gaussian basis-set expansion Abel transform method," *Rev. Sci. Instrum.* **73,** 2634 (2002).

50. W. C. Martin, R. Zalubas, and A. Musgrove, "Energy Levels of Sulfur, S I Through S XVI," *J. Phys. Chem. Ref. Data* **19,** 821 (1990).

51. C. Blondel, W. Chaibi, C. Delsart, C. Drag, F. Goldfarb, and S. Kröger, "The electron affinities of O, Si, and S revisited with the photodetachment microscope," *Eur. Phys. J. D* **33,** 335 (2005).

52. J. E. Wells and J. N. Yukich, "Photodetachment spectroscopy from the lowest threshold of S^-," *Phys. Rev. A* **80,** 055403 (2009).

53. E. E. Ferguson, F. C. Fehsenfeld, and A. L. Schmeltekopf, "Flowing Afterglow Measurements of Ion-Neutral Reactions," *Advances in Atomic and Molecular Physics* **5,** 1 (1969).

54. G. I. Mackay, G. D. Vlachos, D. K. Bohme, and H. I. Schiff, "Studies of reactions involving $C_2H_X^+$ ions with HCN using a modified selected ion flow tube," *Int. J. Mass Spectrom. Ion Processes* **36,** 259 (1980).

55. D. Smith and N. G. Adams, "An Ion-Ion Afterglow Plasma as a Source of Simple and Clustered Positive and Negative-Ions," *Journal of Physics D-Applied Physics* **13,** 1267 (1980).

56. C. H. Depuy and V. M. Bierbaum, "Gas-Phase Reactions of Organic-Anions as Studied by the Flowing Afterglow Technique," *Accounts Chem. Res.* **14,** 146 (1981).

57. D. G. Leopold, K. K. Murray, and W. C. Lineberger, "Laser photoelectron spectroscopy of vibrationally relaxed CH_2^-: A reinvestigation of the singlet–triplet splitting in methylene," *J. Chem. Phys.* **81,** 1048 (1984).

58. W. H. Robertson and M. A. Johnson, "Molecular Aspects of Halide Ion Hydration: the Cluster Approach," *Annu. Rev. Phys. Chem.* **54,** 173 (2003).

59. C. J. Johnson, B. B. Shen, B. L. J. Poad, and R. E. Continetti, "Photoelectron-photofragment coincidence spectroscopy in a cryogenically cooled linear electrostatic ion beam trap," *Rev. Sci. Instrum.* **82,** 105105 (2011).

60. C. Hock, J. B. Kim, M. L. Weichman, T. I. Yacovitch, and D. M. Neumark, "Slow photoelectron velocity-map imaging spectroscopy of cold negative ions," *J. Chem. Phys.* **137,** 244201 (2012).

61. K. R. Asmis, T. R. Taylor, C. Xu, and D. M. Neumark, "Anion photoelectron spectroscopy of I_2^- and $I_2^-Ar_n$ (n = 1–14, 16, 20) clusters," *J. Chem. Phys.* **109,** 4389 (1998).

62. C. L. Adams, H. Schneider, K. M. Ervin, and J. M. Weber, "Low-energy photoelectron imaging spectroscopy of nitromethane anions: Electron affinity, vibrational features, anisotropies, and the dipole-bound state," *J. Chem. Phys.* **130,** 074307 (2009).

63. C. L. Adams and J. M. Weber, "Photoelectron imaging spectroscopy of nitroethane anions," *J. Chem. Phys.* **134,** 244301 (2011).

64. E. M. Miller, L. Sheps, Y.-J. Lu, A. S. Case, A. B. McCoy, and W. C. Lineberger, "New view of the ICN A continuum using photoelectron spectroscopy of ICN^-," *J. Chem. Phys.* **136,** 044313 (2012).

65. S. T. Arnold, J. H. Hendricks, and K. H. Bowen, "Photoelectron spectroscopy of the solvated anion clusters $O^-(Ar)_n$=1–26,34: Energetics and structure," *J. Chem. Phys.* **102,** 39 (1995).

66. C. Desfrancois, H. Abdoul-Carime, and J. P. Schermann, "Electron attachment to isolated nucleic acid bases," *J. Chem. Phys.* **104,** 7792 (1996).

67. S. Xu, W. Zheng, D. Radisic, and Kit H. Bowen, Jr., "The stabilization of arginine's zwitterion by dipole-binding of an excess electron," *J. Chem. Phys.* **122,** 091103 (2005).

68. C. J. Johnson, M. E. Harding, B. L. J. Poad, J. F. Stanton, and R. E. Continetti, "Electron Affinities, Well Depths, and Vibrational Spectroscopy of cis- and trans-HOCO," *J. Am. Chem. Soc.* **133,** 19606 (2011).

69. S. J. Blanksby, T. M. Ramond, G. E. Davico, M. R. Nimlos, S. Kato, V. M. Bierbaum, W. C. Lineberger, G. B. Ellison, and M. Okumura, "Negative-Ion Photoelectron Spectroscopy, Gas-Phase Acidity, and Thermochemistry of the Peroxyl Radicals CH_3OO and CH_3CH_2OO," *J. Am. Chem. Soc.* **123,** 9585 (2001).

70. K. Luria, W. Christen, and U. Even, "Generation and Propagation of Intense Supersonic Beams," *J. Phys. Chem. A* **115,** 7362 (2011).

71. L. J. Puckett and W. C. Lineberger, "Negative-Ion Reactions in NO-H_2O Mixtures," *Phys. Rev. A* **1,** 1635 (1970).

72. G. B. Ellison, P. C. Engelking, and W. C. Lineberger, "An Experimental Determination of the Geometry and Electron Affinity of CH_3," *J. Am. Chem. Soc.* **100,** 2556 (1978).

73. O. Echt, K. Sattler, and E. Recknagel, "Magic Numbers for Sphere Packings: Experimental Verification in Free Xenon Clusters," *Phys. Rev. Lett.* **47,** 1121 (1981).

74. S. R. Desai, C. S. Feigerle, and J. C. Miller, "Magic numbers in $(NO)_m^+Ar_n$ heteroclusters produced by two-photon ionization in a supersonic expansion," *J. Chem. Phys.* **97,** 1793 (1992).

75. E. Garand, A. A. Buchachenko, T. I. Yacovitch, M. M. Szcześniak, G. Chałasiński, and D. M. Neumark, "Study of ArO^- and ArO via Slow Photoelectron Velocity-Map Imaging Spectroscopy and Ab Initio Calculations," *J. Phys. Chem. A* **113,** 4631 (2009).

76. X.-B. Wang, X.-P. Xing, and L.-S. Wang, "Observation of H_2 Aggregation onto a Doubly Charged Anion in a Temperature-Controlled Ion Trap," *J. Phys. Chem. A* **112,** 13271 (2008).

77. D. E. Manolopoulos, K. Stark, H.-J. Werner, D. W. Arnold, S. E. Bradforth, and D. M. Neumark, "The Transition State of the F + H_2 Reaction," *Science* **262,** 1852 (1993).

78. E. de Beer, E. H. Kim, D. M. Neumark, R. F. Gunion, and W. C. Lineberger, "Transition state spectroscopy of the OH + H_2 → H_2O + H reaction via photodetachment of H_3O^- and D_3O^-," *J. Phys. Chem.* **99,** 13627 (1995).

79. T. I. Yacovitch, E. Garand, J. B. Kim, C. Hock, T. Theis, and D. M. Neumark, "Vibrationally resolved transition state spectroscopy of the F + H_2 and F + CH_4 reactions," *Faraday Discuss.* **157,** 399 (2012).

80. M. Okumura, L. I. Yeh, and Y. T. Lee, "The vibrational predissociation spectroscopy of hydrogen cluster ions," *J. Chem. Phys.* **83,** 3705 (1985).

81. M. Okumura, L. I. Yeh, J. D. Myers, and Y. T. Lee, "Infrared spectra of the cluster ions $H_7O_3^+H_2$ and $H_9O_4^+H_2$," *J. Chem. Phys.* **85,** 2328 (1986).

82. M. Okumura, L. I. Yeh, J. D. Myers, and Y. T. Lee, "Infrared Spectra of the Solvated Hydronium Ion: Vibrational Predissociation Spectroscopy of Mass-Selected $H_3O^+(H_2O)_n(H_2)_m$," *J. Phys. Chem.* **94,** 3416 (1990).

83. D. L. Osborn, D. J. Leahy, E. H. Kim, E. de Beer, and D. M. Neumark, "Photoelectron spectroscopy of CH_3O^- and CD_3O^-," *Chem. Phys. Lett.* **292,** 651 (1998).

84. T. M. Ramond, G. E. Davico, R. L. Schwartz, and W. C. Lineberger, "Vibronic structure of alkoxy radicals via photoelectron spectroscopy," *J. Chem. Phys.* **112,** 1158 (2000).

85. M. J. Nee, A. Osterwalder, J. Zhou, and D. M. Neumark, "Slow electron velocity-map imaging photoelectron spectra of the methoxide anion," *J. Chem. Phys.* **125,** 014306 (2006).

86. S. Geltman, "Theory of Threshold Energy Dependence of Photodetachment of Diatomic Molecular Negative Ions," *Phys. Rev.* **112,** 176 (1958).

87. P. C. Engelking and D. R. Herrick, "Effects of rotational doubling on the anomalous photodetachment thresholds resulting from electron-dipole interaction," *Phys. Rev. A* **29,** 2425 (1984).

88. J. R. Smith, J. B. Kim, and W. C. Lineberger, "High-resolution threshold photodetachment spectroscopy of OH^-," *Phys. Rev. A* **55,** 2036 (1997).

89. Zhixin Tian and S. R. Kass, "Carbanions in the Gas Phase," *Chem. Rev.* **113,** 6986 (2013).

90. C. E. Cleeton and N. H. Williams, "Electromagnetic Waves of 1.1 cm Wave-Length and the Absorption Spectrum of Ammonia," *Phys. Rev.* **45,** 234 (1934).

91. L. H. Jones, "Measurement and analysis of the ν_2 bands of $^{14}ND_3$ and $^{15}ND_3$," *J. Mol. Spectrosc.* **74,** 409 (1979).

92. D.-J. Liu and T. Oka, "Experimental Determination of the Ground-State Inversion Splitting in H_3O^+," *Phys. Rev. Lett.* **54,** 1787 (1985).

93. T. J. Sears, P. R. Bunker, P. B. Davies, S. A. Johnson, and V. Spirko, "Diode laser absorption spectroscopy of D_3O^+: Determination of the equilibrium structure and potential function of the oxonium ion," *J. Chem. Phys.* **83,** 2676 (1985).

94. M. Araki, H. Ozeki, and S. Saito, "Experimental determination of the ground-state inversion splitting in D_3O^+ by microwave spectroscopy," *J. Chem. Phys.* **109,** 5707 (1998).

95. A. F. Gaines and F. M. Page, "The Stabilities of Negative Ions. I. The Methyl-, Diphenylmethyl, and Triphenylmethyl Negative Ions," *Int. J. Mass Spectrom. Ion Phys.* **1,** 315 (1968).

96. D. Feldman, R. Rackwitz, H. J.Kaiser, and E. Heincke, "Photodetachment bei einigen neagtiven molekulionen: P_2^-, As_2^-, CH_2^-, CH_3^-, S_3^-," *Z. Naturforsch. A* **32,** 600 (1977).

97. S. T. Graul and R. R. Squires, "Gas-phase reactions of the methyl anion," *J. Am. Chem. Soc.* **111,** 892 (1989).

98. S. T. Graul and R. R. Squires, "Generation of alkyl carbanions in the gas phase," *J. Am. Chem. Soc.* **112,** 2506 (1990).

99. S. E. Mitchell, P. M. Conklin, and J. W. Farley, "First observation of autodetachment lifetimes of methide, CH_3^-," *J. Chem. Phys.* **118,** 11017 (2003).

100. R. E. Kari and I. G. Csizmadia, "PotentialEnergy Surfaces of CH_3^+ and CH_3," *J. Chem. Phys.* **50,** 1443 (1969).

101. Frank Driessler, Reinhart Ahlrichs, Volker Staemmler, and W. Kutzelnigg, "Ab-initio Calculations on Small Hydrides Including Electron Correlation," *Theoret. chim. Acta (Berl.)* **30,** 315 (1973).

102. C. E. Dykstra, M. Hereld, R. R. Lucchese, H. F. Schaefer, and W. Meyer, "Molecular structure of the methyl anion CH_3^-. An investigation of the effects of electron correlation using the theory of selfconsistent electron pairs (SCEP)," *J. Chem. Phys.* **67,** 4071 (1977).

103. D. S. Marynick and D. A. Dixon, "Electron affinity of the methyl radical: Structures of CH_3 and CH_3^-," *Proc. Natl. Acad. Sci. U.S.A.* **74,** 410 (1977).

104. G.T. Surratt1 and W. A. Goddard III, "Theoretical studies of CH_3, CH_3^+ and CH_3^- using correlated wavefunctions," *Chem. Phys.* **23,** 39 (1977).

105. H. Kollmar, "The stability of alkyl anions. A molecular orbital theoretical study," *J. Am. Chem. Soc.* **100,** 2665 (1978).

106. T. J. Lee and H. F. Schaefer, "Systematic study of molecular anions within the self-consistent-field approximation: OH^-, CN^-, C_2H^-, NH_2^-, and CH_3^-," *J. Chem. Phys.* **83,** 1784 (1985).

107. J. V. Ortiz, "Many-body theory of the ionization energies of CH_3^-, SiH_3^-, and GeH_3^-," *J. Am. Chem. Soc.* **109,** 5072 (1987).

108. John A. Pople, Martin HeadGordon, Douglas J. Fox, Krishnan Raghavachari, and L. A. Curtiss, "Gaussian1 theory: A general procedure for prediction of molecular energies," *J. Chem. Phys.* **90,** 5622 (1989).

109. Larry A. Curtiss, Krishnan Raghavachari, Gary W. Trucks, and J. A. Pople, "Gaussian2 theory for molecular energies of first and secondrow compounds," *J. Chem. Phys.* **94,** 7221 (1991).

110. W. P. Kraemer, V. Špirko, P.-A. Malmqvist, and B. O. Roos, "Inversion-vibration energies of CH_3^- and adiabatic electron affinity of CH_3," *J. Mol. Spectrosc.* **147,** 526 (1991).

111. C. F. Rodriquez, S. Sirois, and A. C. Hopkinson, "Effect of multiple halide substituents on the acidity of methanes and methyl radicals. Electron affinities of chloro- and fluoromethyl radicals," *J. Org. Chem.* **57,** 4869 (1992).

112. Ulrike Salzner and P. v. R. Schleyer, "A successful ab initio study of the adiabatic electron affinity of the methyl radical," *Chem. Phys. Lett.* **199,** 267 (1992).

113. David A. Dixon, David Feller, and K. A. Peterson, "Accurate Calculations of the Electron Affinity and Ionization Potential of the Methyl Radical," *J. Phys. Chem. A* **101,** 9405 (1997).

114. Qian-Shu Li, Jun-Fang Zhao, Yaoming Xie, and H. F. S. III, "Electron affinities, molecular structures, and thermochemistry of the fluorine, chlorine and bromine substituted methyl radicals," *Mol. Phys.* **100,** 3615 (2002).

115. Panayiotis S. Petrou and A. V. Nicolaides, "Electron affinities of a homologous series of tertiary alkyl radicals and their C–H bond dissociation energies (BDEs)," *Tetrahedron* **65,** 1655 (2009).

116. C. Yamada, E. Hirota, and K. Kawaguchi, "Diode laser study of the ν_2 band of the methyl radical," *J. Chem. Phys.* **75,** 5256 (1981).

117. J. M. Frye, T. J. Sears, and D. Leitner, "Diode laser spectroscopy of the ν_2 band of CD_3," *J. Chem. Phys.* **88,** 5300 (1988).

118. Trevor J. Sears, Joan M. Frye, V. Spirko, and W. P. Kraemer, "Extended measurements of the ν_2 band of CD_3 and the determination of the vibrational potential function for methyl," *J. Chem. Phys.* **90,** 2125 (1989).

119. PGOPHER, a Program for Simulating Rotational Structure, C. M. Western, University of Bristol, http://pgopher.chm.bris.ac.uk.

120. I. N. Levine, *Quantum Chemistry*, 5th ed. (Prentice Hall, New Jersey, 2000)

121. M. S. Robinson, M. L. Polak, V. M. Bierbaum, C. H. DePuy, and W. C. Lineberger, "Experimental Studies of Allene, Methylacetylene, and the Propargyl Radical: Bond Dissociation Energies, Gas-Phase Acidities, and Ion-Molecule Chemistry," *J. Am. Chem. Soc.* **117,** 6766 (1995).

122. H. W. Hermann and S. R. Leone, "Photofragment infrared emission spectroscopy: Vibrational progression and potential parameters of the $CH_3(\nu_2)$ ‘‘umbrella’’ mode," *J. Chem. Phys.* **76,** 4759 (1982).

123. Charles H. DePuy, Scott Gronert, Stephan E. Barlow, Veronica M. Bierbaum, and R. Damrauer, "The gas-phase acidities of the alkanes," *J. Am. Chem. Soc.* **111,** 1968 (1989).

124. B. Ruscic, M. Litorja, and R. L. Asher, "Ionization Energy of Methylene Revisited: Improved Values for the Enthalpy of Formation of CH_2 and the Bond Dissociation Energy of CH_3 via Simultaneous Solution of the Local Thermochemical Network," *J. Phys. Chem. A* **103,** 8625 (1999).

125. Y. Song, X.-M. Qian, K.-C. Lau, and C. Y. Ng, "A pulsed field ionization study of the dissociative photoionization reaction $CD_4 + h\nu \rightarrow CH_3^+ + D + e^-$," *Chem. Phys. Lett.* **347,** 51 (2001).

126. J. Higuchi, "Note on the Absorption Spectra of the Methyl Radical," *J. Chem. Phys.* **23,** 2197 (1955).

127. J. Higuchi, "Electronic Structures of the Methyl Radical: Effect of 3s Atomic Orbital of Carbon," *J. Chem. Phys.* **28,** 527 (1958).

128. A. Padgett and M. Krauss, "Electronic Structure of CH_2 and CH_3," *J. Chem. Phys.* **32,** 189 (1960).

129. R. McDiarmid, "Calculation of the energies of the lower excited states of CH_3," *Theoret. chim. Acta (Berl.)* **20,** 282 (1971).

130. G. Olbrich, "MRD CI calculations of excited states of the SiH_3 radical, including potential curves for the inversion mode and the dissociation $SiH_3 \rightarrow SiH_2 + H$," *Chem. Phys.* **101,** 381 (1986).

131. Alexander M. Mebel and S.-H. Lin, "Excited electronic states of the methyl radical. Ab initio molecular orbital study of geometries, excitation energies and vibronic spectra," *Chem. Phys.* **215,** 329 (1997).

132. S. V. Levchenko and A. I. Krylov, "Electronic structure of halogen-substituted methyl radicals: Excited states of CH_2Cl and CH_2F," *J. Chem. Phys.* **115,** 7485 (2001).

133. R. A. Seburg, E. V. Patterson, J. F. Stanton, and R. J. McMahon, "Structures, Automerizations, and Isomerizations of C_3H_2 Isomers," *J. Am. Chem. Soc.* **119,** 5847 (1997).

134. G. Maier, H. P. Reisenauer, W. Schwab, P. Carsky, B. A. Hess Jr., and L. J. Schaad, "Vinylidene carbene: a new C_3H_2 species," *J. Am. Chem. Soc.* **109,** 5183 (1987).

135. J. M. Vrtilek, C. A. Gottlieb, E. W. Gottlieb, T. C. Killian, and P. Thaddeus, "Laboratory detection of propadienylidene, H_2CCC," *Astrophys. J.* **364,** L53 (1990).

136. J. Cernicharo, C. A. Gottlieb, M. Guélin, T. C. Killian, G. Paubert, P. Thaddeus, and J. M. Vrtilek, "Astronomical detection of H_2CCC," *Astrophys. J.* **368,** L39 (1991).

137. C. A. Gottlieb, T. C. Killian, P. Thaddeus, P. Botschwina, J. Flügge, and M. Oswald, "Structure of propadienylidene, H_2CCC," *J. Chem. Phys.* **98,** 4478 (1993).

138. J. Gauss and J. F. Stanton, "The equilibrium structure of propadienylidene," *J. Mol. Struct.* **485,** 43 (1999).

139. M. C. McCarthy and P. Thaddeus, "Carbon-13 Isotopic Species of H_2C_3, H_2C_4, and H_2C_5: High-Resolution Rotational Spectra," *J. Mol. Spectrosc.* **211,** 235 (2002).

140. J. F. Stanton, J. T. DePinto, R. A. Seburg, J. A. Hodges, and R. J. McMahon, "Electronic Spectrum of Propadienylidene (H_2CCC:)," *J. Am. Chem. Soc.* **119,** 429 (1997).

141. J. A. Hodges, R. J. McMahon, K. W. Sattelmeyer, and J. F. Stanton, "Electronic Spectrum of Propadienylidene (H_2C=C=C:) and its Relevance to the Diffuse Interstellar Bands," *Astrophys. J.* **544,** 838 (2000).

142. J. P. Maier, G. A.H. Walker, D. A. Bohlender, F. J. Mazzotti, J. F. R. Raghunandan, I. Garkusha, and A. Nagy, "Identification of H_2CCC as a Diffuse Interstellar Band Carrier," *Astrophys. J.* **726,** 41 (2011).

143. T. Oka and B. J. McCall, "Disclosing Identities in Diffuse Interstellar Bands," *Science* **331,** 293 (2011).

144. Harvey Liszt, Paule Sonnentrucker, Martin Cordiner, and M. Gerin, "The Abundance of C_3H_2 and Other Small Hydrocarbons in the Diffuse Interstellar Medium," *Astrophys. J.* **753,** L28 (2012).

145. M. Araki, S. Takano, H. Yamabe, K. Tsukiyama, and N. Kuze, "Radio Search for H_2CCC Toward HD 183143 as a Candidate for a Diffuse Interstellar Band Carrier," *Astrophys. J.* **753,** L11 (2012).

146. J. M. Oakes and G. B. Ellison, "Photoelectron spectroscopy of radical anions," *Tetrahedron* **42,** 6263 (1986).

147. K. Yokoyama, G. W. Leach, J. B. Kim, and W. C. Lineberger, "Autodetachment spectroscopy and dynamics of dipole bound states of negative ions: $^2A_1$–$^2B_1$ transitions of H_2CCC^-," *J. Chem. Phys.* **105,** 10696 (1996).

148. D. M. Neumark, K. R. Lykke, T. Anderson, and W. C. Lineberger, "Laser photodetachment measurement of the electron affinity of atomic oxygen," *Phys. Rev. A* **32,** 1890 (1985).

149. C. E. Moore, *Atomic Energy Levels (National Bureau of Standards, Washington, D.C., 1949)*, Vol. I.

150. C. E. Moore, *Atomic Energy Levels (National Bureau of Standards, Washington, D.C., 1949)*, Vol. III.

151. D. Hanstorp and M. Gustafsson, "Determination of the electron affinity of iodine," *J. Phys. B* **25,** 1773 (1992).

152. J. F. Stanton, E. Garand, J. Kim, T. I. Yacovitch, C. Hock, A. S. Case, E. M. Miller, Y.-J. Lu, K. M. Vogelhuber, S. W. Wren, T. Ichino, J. P. Maier, R. J. McMahon, D. L. Osborn, D.

M. Neumark, and W. C. Lineberger, "Ground and low-lying excited states of propadienylidene ($H_2C=C=C:$) obtained by negative ion photoelectron spectroscopy," *J. Chem. Phys.* **136,** 134312 (2012).

153. P. Thaddeus, C. A. Gottlieb, R. Mollaaghababa, and J. M. Vrtilek, "Free carbenes in the interstellar gas," *J. Chem. Soc., Faraday Trans.* **89,** 2125 (1993).

154. R. A. Seburg, E. V. Patterson, and R. J. McMahon, "Structure of Triplet Propynylidene (HCCCH) as Probed by IR, UV/vis, and EPR Spectroscopy of Isotopomers," *J. Am. Chem. Soc.* **131,** 9442 (2009).

155. A. M. Mebel, W. M. Jackson, A. H. H. Chang, and S. H. Lin, "Photodissociation Dynamics of Propyne and Allene: A View from ab Initio Calculations of the C_3H_n (n = 1−4) Species and the Isomerization Mechanism for C_3H_2," *J. Am. Chem. Soc.* **120,** 5751 (1998).

156. M. C. van Hemerta and E. F. van Dishoeck, "Photodissociation of small carbonaceous molecules of astrophysical interest," *Chem. Phys.* **343,** 292 (2008).

157. J. H. J. Dawson, T. A. M. Kaandorp., and N. M. M. Nibbering, "A gas phase study of the ions $[C_3H_2]^-$ and $[C_3H_3]^-$ generated from the reaction of O^- with propyne," *Org. Mass Spectrom.* **12,** 330 (1977).

158. D. L. Osborn, K. M. Vogelhuber, S. W. Wren, E. M. Miller, Y.-J. Lu, A. S. Case, L. Sheps, R. J. McMahon, J. F. Stanton, L. B. Harding, B. Ruscic, and W. C. Lineberger, "Electronic States of the Quasi-linear Molecule Propargylene (HCCCH) from Negative Ion Photoelectron Spectroscopy," *J. Am. Chem. Soc.* **136,** ASAP (2014).

Appendix A: Schematic Drawings of the Parts of the Discharge Source

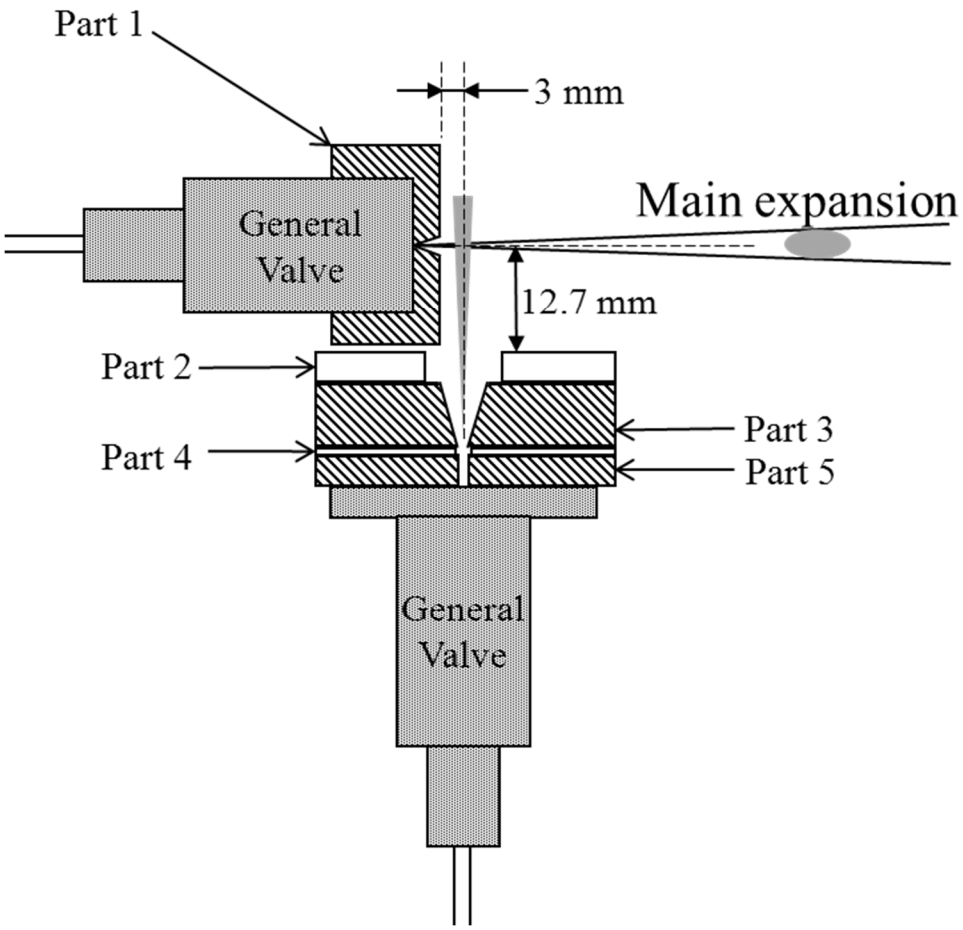

Figure A.1 Schematic arrangement of the pulsed plasma-entrainment anion source employing two solenoid valves. Part 1 is a custom-made conical nozzle coupling with a General Valve body, part 2 is a cylindrical MACOR plate, part 3 is an electrode (stainless steel or aluminum) pulsed to negative high voltage, part 4 is a thin MACOR insulator between two electrodes, and part 5 is a thin electrode (stainless steel) attached to a commercial General Valve faceplate held at earth ground. These components are expanded below.

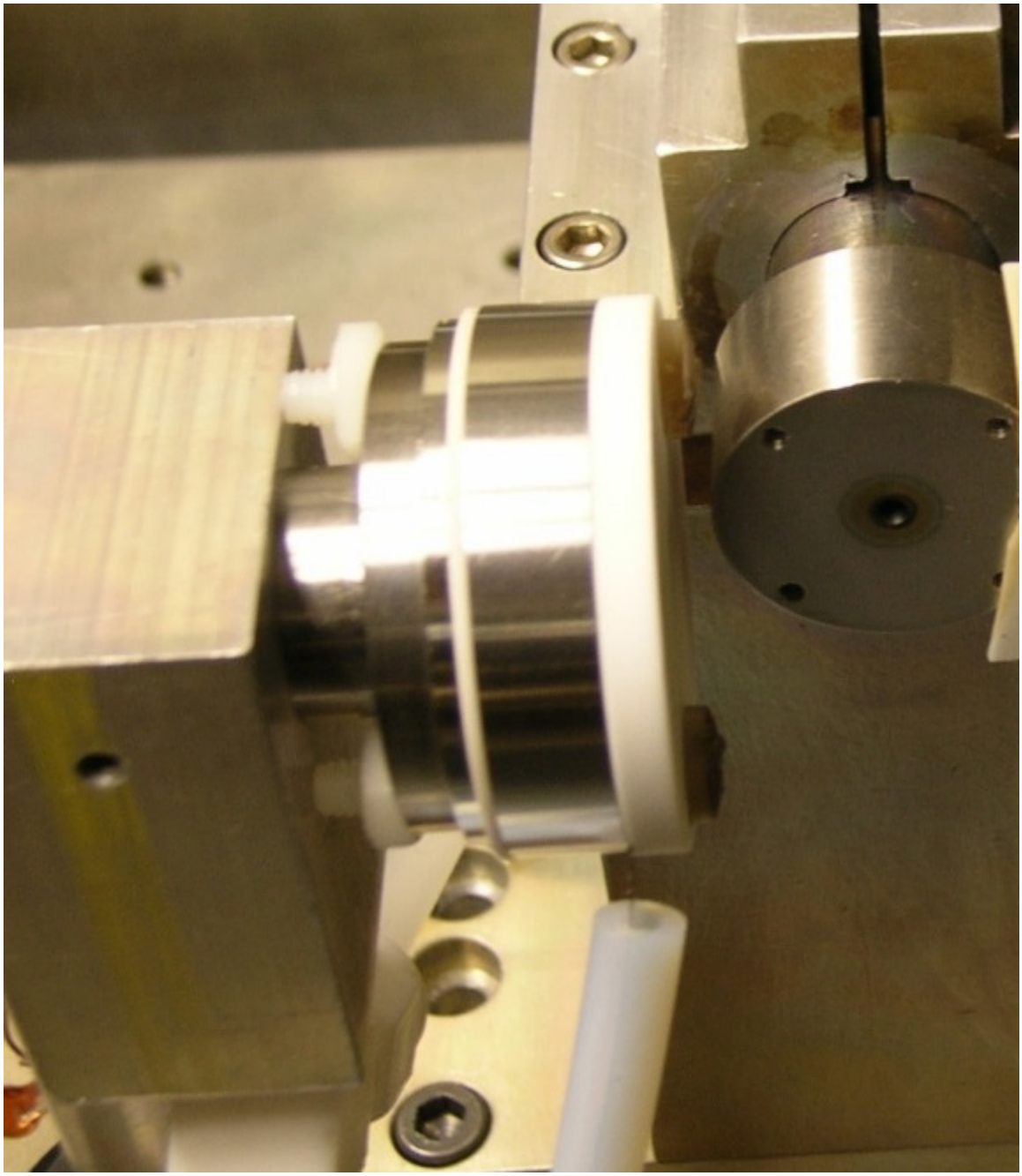

Figure A.2 Picture of the setup showing how both pulsed valves are mounted in the source chamber. This picture also displays how the stack of insulators and electrodes is held together. All components of the discharge device have four bolt holes and are fastened onto the faceplate of the side solenoid valve using two nylon screws.

Part 1: 40°-cone, 3.5-mm thick, 500-µm conical nozzle

In order to increase the forward intensity of the main expansion, we use a 40° conical nozzle with a 0.5-mm orifice (D_O) and an aspect ratio (L/D_O) of 7.[70] The nozzle seals in a similar fashion as a commercial faceplate and, thus, couples well with a General Valve body.

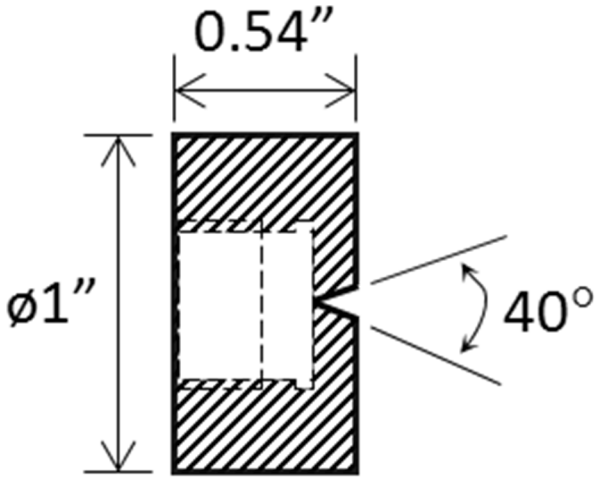

Part 2: The ended MACOR plate:

This MACOR plate separates the main pulsed valve and the electrode (part 3) that is pulsed to negative high voltage.

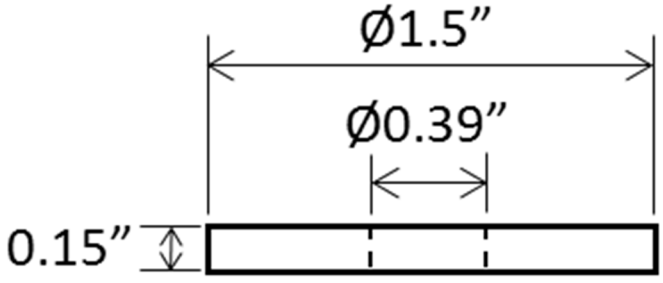

Part 3: The electrode (S.S. or aluminum) pulsed to negative high voltage:

A pulsed voltage between -800 and -2000 V is used to maximize the ion intensities and the stability of the discharge. Additionally, we use a 40° conical nozzle with a 1-mm orifice to collimate generated plasma. In order to have stable discharge, the edge of the orifice is required to be clean and smooth. We clean the surface using #400 sand papers and make the edge smooth using the electropolishing machine at JILA machine shop.

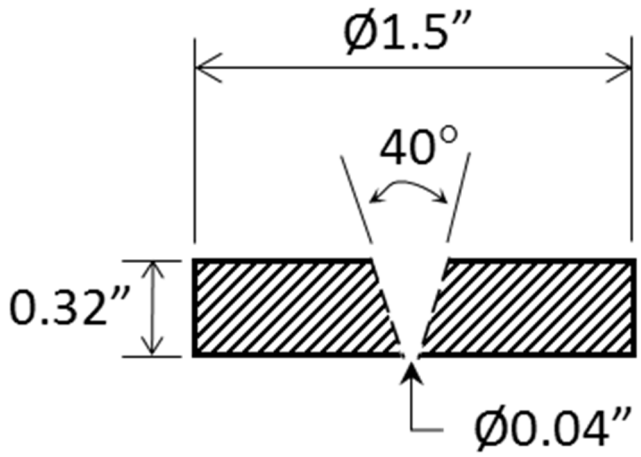

Part 4: The thin MACOR insulator between two electrodes:

The central hole of this MACOR insulator is very fast to get dirty since the discharge occurs at this region. We use sand “wires” or small driller to get rid of thin layers from the surface of the middle hole.

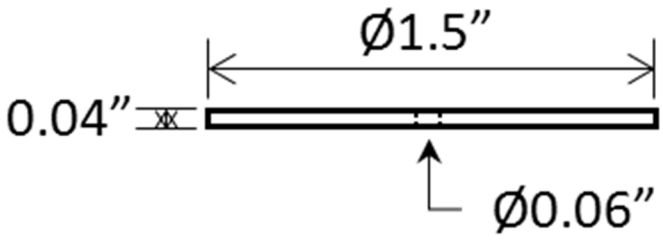

Part 5: The thin electrode (S.S.) held at earth ground:

We use this plate to avoid heating up or discharging to the faceplate of the solenoid valve. This plate is also fast to get dirty and damaged, so the surface of the electrode needs to be clean and smooth. We clean the surface using #400 sand papers and make the surface smooth using the electropolishing machine at JILA machine shop.

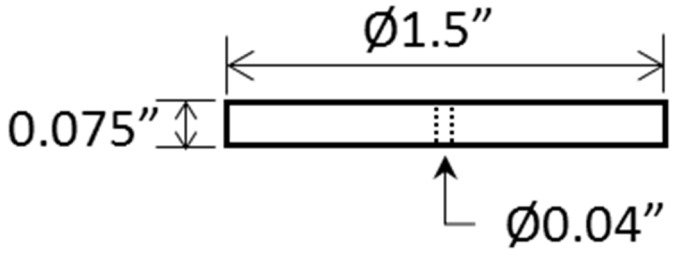

Appendix B: Expanded Sectional View of the Discharging Region

In this design, the gas density at the discharge region between two electrodes is high enough to produce plasma. The diameters of both central holes in two electrodes are 1 mm, while the diameter of the middle hole in the MACOR insulator is slightly larger, 1.5 mm.

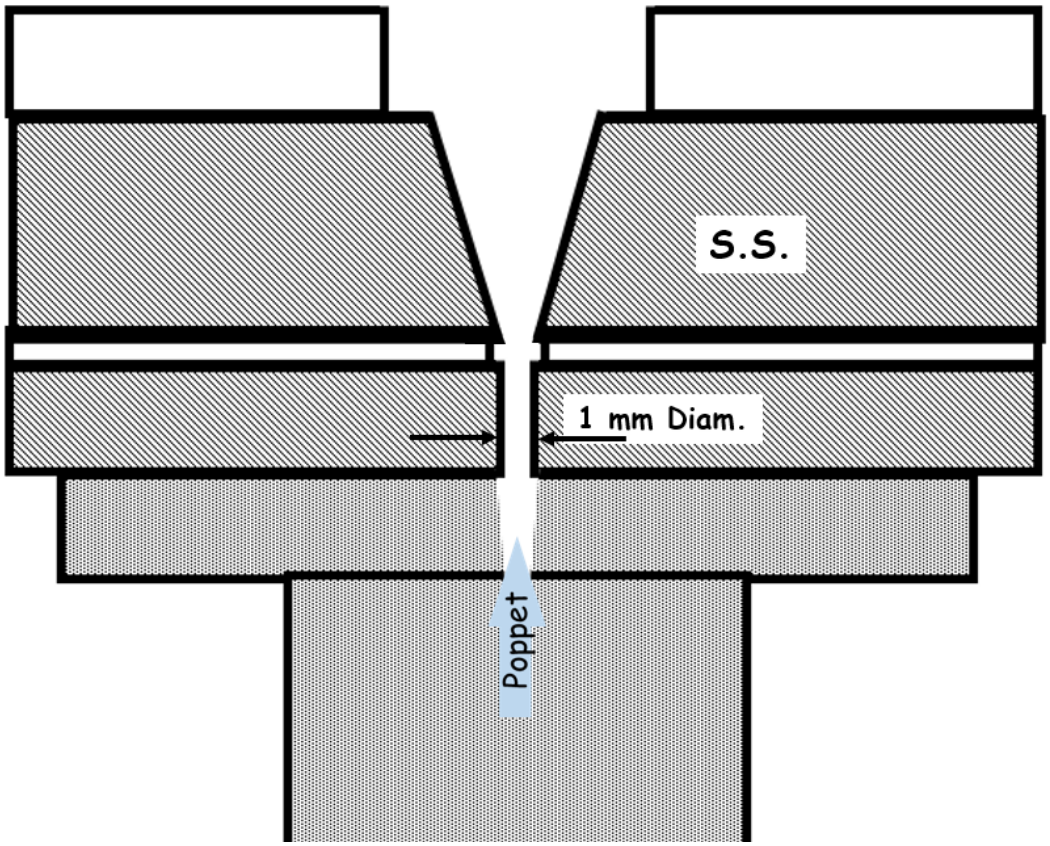

Appendix C: Source Conditions for $OH^-(Ar)_n$ Cluster Formation

Main expansion: 3.7-atm neat Ar

Side expansion: 4.7-atm 1% O_2 / 25% H_2 / Ar

(Although the backing pressures of both gas mixtures are similar, the side pulsed valve opens shortly, resulting in that the ion-gauge pressure reading for the side valve is roughly one order of magnitude less than that for the main valve.)

Pulsed discharge voltage: -2000 V

(The electrode is in series with two 10 kΩ resistors for increasing discharge stability.)

Pulsed discharge duration: 40 ~ 140 μs

(Once ions are found with a long pulsed discharge duration (e.g., 140 μs), decreasing the duration with small steps (10 μs) and optimizing the discharge timing until reaching a duration of 40 μs are helpful to achieve cold anion beam.)

Discharge current: 75 mA

(The voltage drop across two 10 kΩ resistors is -1.5 kV, corresponding to a discharge current of 75 mA.)

Temporal FWHM of the ion packet: 20 μs

(We vary the timing of the extraction plate that directs anions down the TOF MS to measure the time spread of the ion packet in the main expansion.)